

General response

We present a thoroughly revised manuscript, addressing the issues raised by the two Reviewers and the Executive Editor. We made the following changes:

- Over the recent months, we have further developed the model, including several bug fixes. For this reason, we redid all simulations, with improved settings and based on the comments below. Particularly the warming example simulation looks different now as a melt pond forms on top of the sea ice. In the first submission, an improper treatment of the upper boundary by the model could lead to the loss of meltwater at the top of the model domain. This has been corrected.
- We revised all plots and added more explanation where appropriate.
- We now provide an outlook section where we address how discrepancies between our simulations and the existing literature are briefly addressed.
- We removed the discussion of the Bucket scheme with fixed, prescribed salinity profiles. We encountered that the implementation was flawed, as the bucket scheme may transport part of the brine downward when it exceeds the size of the "bucket". However, the thermodynamics routine would melt additional sea ice to maintain thermal equilibrium, which in turn again would be transported downward by the water transport scheme. This is undesirable and we were not able to come up with a solution within the time frame of the review process.

Please find a detailed response below, followed by the revised manuscript and a track-changed version of the revised manuscript. Note that page and line numbers refer to the revised manuscript without track changes.

Response to Reviewers

Reviewer #1

In the manuscript: "Version 1 of a sea ice module for the physics based, detailed, multi-layer SNOWPACK model", an extension of the physical based SNOWPACK model to sea ice is presented. Parts of the model equations are adapted to account for salinity. In addition, other relevant processes like sea ice growth and melt, flooding and brine dynamics are included. The authors discuss the performance of the model comparing it to snow buoy and IMB measurements over Antarctic sea ice. Overall, this manuscript is well written and has a clear structure. Modeling the evolution of snow on sea ice is a challenging task and the here presented model extensions provide important progress for the snow on sea ice modeling community. I believe that this model will be widely used in future research, especially if it will be coupled to SMRT like the authors state in their conclusions. However, the presentation and the discussion of the results are partly too short and important details are missing. Therefore I recommend the manuscript to be published after major revisions. I have three general comments that I would like the authors to address.

We thank the reviewer for the careful review and constructive comments. Please find our response to the issues raised below.

General comments (GC):

- GC1: In the description of the experiments, important details about the model initialization are missing. In SNOWPACK, the snow is described by grain parameters like dendricity, sphericity and bond radius. These parameters are hard to obtain from snowpit or snow buoy measurements and I wonder what the authors assumed in the model initialization (so far, it is not mentioned in the manuscript). A discussion about these parameters and their influence on the results would be very helpful for further SNOWPACK users. In addition, the authors should provide the full initialization profiles and SNOWPACK settings (I guess this can be provided in the appendix).

So far, we used a simple procedure for the initialization of the snow layers, as the buoys were installed with low snow depths, such that the majority of the snow accumulates in the simulations after initialization.

We mention this in the revised manuscript P12,L29-31. Otherwise, it is typically recommended to run SNOWPACK for some setup and then select layers that closest match the observed layering in terms of grain size, grain shape and density. Note that the Online supplement contains the input files for the SNOWPACK model as used in this study.

- GC2: In general, the motivation and discussion of the different experiments (section 4.1 to 4.5) are too short and need to be extended. Some features, which are visible in the figures are not or only poorly discussed. I encourage the authors to carefully read my specific comments for the single chapters.
Please find our response to the points raised below. We improved the introduction and discussion of the results throughout the manuscript.
- GC3: It seems like the authors used the same color-scale range for all figures. In some figures, it is impossible to distinguish between different values since the color-scale goes far beyond the actual values in the figure. I recommend to use individual, representative color-scales for each figure.
We revised all the figures.

Specific comments:

- Section 3.1: Please improve figure 1.
We improved the readability of the figure.
- Section 4.1: From figure 2, it looks like it takes less than two hours until the 1.58 m thick sea ice is saturated. Is this realistic? It seems very fast to me.
It indeed seems to be an overestimation. We used the arithmetic mean for averaging the hydraulic conductivity between nodes, even though geometric mean is recommended (see (Haverkamp and Vauclin, 1979; Celia et al., 1990)). We therefore repeated the simulations shown in the paper using the geometric mean. We then find a longer time period before saturation is reached (around 16 hours). The saturated hydraulic conductivity for a porosity of 0.06 is 0.000035474 m/s. This corresponds to about 13 cm/hour. We provide now additional explanation in the manuscript (P15,L11-13).
- The caption for figure 2 (a) is confusing. I guess you mean "dry sea ice" instead of "dry snow"? In figure 2 (a) to 2 (d) the color-scale range need to be improved.
We rephrased the caption and improved the figure (Fig. 4 in the revised manuscript).
- Section 4.2: Please increase the y-axis in figure 3 (b) Please mention what the blue line in figure 3 (c) is (I guess the ice/ocean interface?).
We improved the figure and figure caption (Fig. 5 in the revised manuscript).
- In figure 3 (d), a difference of 6-10C is found close to the snow/ice interface. Do you expect the differences to be even higher at the top of the snow? As I understood, you use ERA5 incoming longwave radiation as a forcing data. So in principle, the differences shown in figure 3 (d) could also be caused by errors in the forcing data. It might be helpful to add a timeseries of the ERA forcing data to figure 3.
We added two figures with the forcing data for the two Snow Buoys (see Figs. 2 and 3 in the revised manuscript). We discuss now that temperature errors can also be a result of errors in the forcing data (P18,L1-2).
- I'm surprised that even at the ice/ocean interface, the difference can be up to 2C. To my understanding, the temperature should always be around the freezing temperature, or not?
The reason is that the simulate ice thickness is slightly underestimated, such that the lower boundary in the simulation is not exactly the lower boundary in the measurements. We explain this now in P16,L5-6.
- The caption for figure 4 is wrong (there is no temperature plot). Please adapt the color-scale for figure 4 (b).
We improved the figure and figure caption (now Fig. 7 in the revised manuscript).
- Section 4.3: It is not clear to me, what the authors want to demonstrate in this section. I therefore encourage the authors to write a short motivation at the start of the experiments (This also applies for the subsequent

sections). In Figure 5 (a) to 5 (c), vertical stripes are visible at the end of the simulation, which look like numerical instabilities. Are these related to the bucket scheme or to a too big timestep?

We actually decided to remove the description and simulation of the bucket scheme with fixed, prescribed salinity profiles. We encountered that the implementation was flawed, as the bucket scheme may transport part of the brine downward when it exceeds the size of the "bucket". However, the thermodynamics routine would melt additional sea ice to maintain thermal equilibrium, which in turn again would be transported downward by the water transport scheme. This is undesirable and we were not able to come up with a solution within the time frame of the review process.

- Section 4.4 In figure 6 (b) and (d), horizontal stripes are visible in the ice in the middle and at the end of the simulation, which look like numerical instabilities. To my understanding, these patterns should not appear since you are using the Crank-Nicolson scheme and the CFL criteria. Do you have an explanation for this phenomena? Please also discuss if these instabilities could have influenced the results of the simulations. *Crank-Nicolson is not necessarily immune to spurious oscillations when sharp gradients, discontinuities are present (Østerby, 2003). The CFL criterion is not necessary for the Crank-Nicolson scheme, but helps reduce some of the oscillations. The diffusion term helps to dampen the oscillations. There are some other numerical schemes which may exhibit smaller oscillatory behaviour (upwind schemes, Runge-Kutta method), and those could be considered in future revisions of the SNOWPACK model (see P28,L29-31).*
- In figure 6 (d), high brine salinity is simulated at the top of the snowpack. This must be wrong as I can't find any explanation how this could have happened? (especially since the snow was dry according to figure 6 (b)).

The brine salinity appearing in the near surface layer resulted from numerical rounding errors when calculating bulk salinity, which, given the low temperatures, resulted in very high brine salinities. This rounding error has been resolved now by revising the model source code.

- Figure 7 (a), (c) and (d) are not discussed in the text.
We added a discussion of the simulated snow microstructure, see P20,L28-34.
- Section 4.5. Please extend the discussion of the experiments.
Please see the revised section (Section 4.4 in the revised manuscript).
- The color-scale for figure 8 (a) needs to be adjusted.
We think that the colour bar for 8(a) (Fig. 10(a) in the revised manuscript) spans the temperature range in the simulations, so we are uncertain what the reviewer exactly means here.
- Section 4.6. Please extend the discussion and describe in more detail what is seen in figure 11.
We amended the discussion of Fig. 11 (Fig. 13(a) in Section 4.5 in the revised manuscript).

Minor comments and typos: (P refers to the page and L to the line)

- P1L3: cut "strongly"
Corrected.
- P1L18: "high salinity water" → "saline water"
Corrected.
- P2L4: Snow limits also the summer sea ice melt
Amended the text.
- P2L8-9: Please consider to rewrite this abstract since it is hard to understand
Rephrased.
- P2L10: "snow melt" → "melted snow"
Changed to: "Snow meltwater"
- P2L12: "Uncertainty in knowledge" reads strange, please rephrase
Changed to: "limited knowledge"

- P2L13: "Assessing snow amounts on sea ice is not straight-forward from atmospheric forcing alone" → "Assessing snow amounts on sea ice from atmospheric forcing alone is not straight-forward"
Rephrased.
- P2L22-23: I think all of these effects can also be observed during winter season.
It was indeed poorly formulated. We rephrased the sentence.
- P2L23-25: Please specify "shallow snow". According to figure 1 the snow depth can be up to 1 m which I would not consider as shallow.
It was indeed poorly formulated, and we took "shallow" with reference to alpine snowpacks. We rephrased the sentence.
- P2L26: "...impact on snow microstructure..." → "impact on the snow microstructure"
Corrected.
- P3L2: You could cite a paper dealing with this problem. E.g. Markus et al (2006)
Citation added.
- P3L17: Please explain the grain parameters.
Brief explanations and appropriate citation added (P3,L27-32 in the revised manuscript).
- P4L15-20: This paragraph is difficult to read. I recommend to rewrite it
We rephrased this paragraph.
- P4L26: "in the ocean from below" → "in the sea ice from the ocean below"
Rephrased.
- P6L13-14: "A critical assumption is.... That it assumes..." please rewrite.
Rephrased.
- P7L13: What does MPFD mean in equation 14?
We closely follow the notation in Celia et al. (1990), where it is not specified either, but presumably it stands for the right hand side of the Modified-Picard Finite Differences approximation.
- P7L22: please explain all coefficients in equation 15.
Missing coefficients added, including an equation to show the calculation of the fluxes q (see Eq. 15 and 16 in the revised manuscript).
- P8L18: "w" → "we"
Corrected.
- P8L18: please mention what CFL stands for
Amended and citation added.
- P8L25: "and a Dirichlet boundary condition by..." → "and a Dirichlet boundary condition at the bottom by..."
Corrected.
- P9L3: Equation 18 needs to be explained in more detailed
We provide now an additional step in the derivation (see Eq. 20 in the revised manuscript).
- P9L20: cut out "for snow"
Corrected.
- P10F1: "two sea ice buoys" → "two snow buoys". Please improve the notation of the dates in this figure.
Corrected.
- P10L1: In general, the buoys to not measure the snow depth but the hight of the snow above the initial snow/ice interface. In case of the formation of superimposed, this can make a significant difference
Good point that this was poorly formulated. We rephrased this part.

- P11L17: "after which" → "and"
Corrected.
- P11L18: "up to" → "until"
Corrected.
- P11L25: to me, a volumetric ice content of 0.9 seems rather low.
Indeed, a volumetric ice content of 0.9 is rather low, so we redid the simulations with a volumetric ice content of 0.95, unless stated otherwise.
- P12L7-8: "ERA5...to provide" → "ERA5...data to provide"
Corrected.
- P14L6-8: This reads strange, please rewrite
Rephrased.
- P14L7: Please specify "spring" (which months?)
Specified the months.
- P15L11: Please specify "slightly"
This was indeed poorly formulated. Just before our initial submission, we discovered that we interpreted the precipitation rates from the ERA5 data wrongly. After correcting, we didn't adapt the figure scaling and manuscript in accordance with the new simulation result. We apologize for that.
- P16L6: "depending" → "depending on"
Corrected.
- P17F5: I don't see grey colored snow in figure 5 (b)
Corrected, it was due to copying figure captions without realizing the sentence was not valid for this figure.
- P17L9: "For warming" → "For the warming experiment"
Rephrased to: "To force warming conditions, ..."
- P20: Figure 8 is shown before mentioning it in the text
Corrected.
- P22L1: Please rewrite the first sentence
Rephrased.
- P22L25: "simulate sea ice" → "simulated snow on sea ice"
Rephrased it differently. We think that we should stress here that SNOWPACK does not only simulate snow on sea ice, but the snow – sea ice system as a whole.
- P24: I don't see grey snow in figure 11 (b).
Corrected, it was due to copying figure captions without realizing the sentence was not valid for this figure.
- P24F11: "melting conditions is enforced" → "melting conditions are enforced"
Corrected.
- P25L3-4: please rewrite
Rephrased.
- P25L7: "limited forcing data" → "limited measurement data"
Corrected.
- P25L7-9: please mention the other limited measurement data
This paragraph was poorly formulated and has been revised.

Reviewer #2

The analysis is a model demonstration of applying SNOWPACK, a sophisticated snowmodel, in the Antarctic sea-ice environment. The topic presented here is of great interest to the cryosphere community, and is an excellent example of transferring knowledge from the terrestrial snow environment to the sea-ice environment. The analysis is well-presented, the manuscript being clearly-written and well-organized. There are several assumptions made for the model that need further explanation, especially with regard to how these assumptions compare to the true sea-ice environment and the implications of their differences. Please find comments below that I hope the authors will find useful.

We thank the reviewer for the insightful and constructive comments. Please find below our response to the issues raised.

- P1, L4. It's the loss of brine during melt that lowers sea-ice salinity, not so much freshwater percolation. Sea ice salinity decreases during the melt season with the expansion and interconnection of brine channels, leading to melt pond (and melt water) drainage through the ice.
We rephrased this sentence to include melt ponds, nevertheless, we found several mentions in literature of flushing of salt out of the sea ice due to freshwater percolation (Notz and Worster, 2009). We now mention melt ponds in the introduction (see P2,L32-35 in the revised manuscript).
- P1, L7. Delete "and" before "to describe water..."
Sentence rephrased in a different way.
- P2, L5-6. And the need to better represent the heterogeneity of these properties?
Good point, rephrased to: "indicating the need to explicitly consider those properties and their spatial and vertical variability."
- P2, L8. "the snow cover" do you mean the weight of the snow cover?
Sentence rephrased "... the snow cover, due to its weight, pushes ...". We think that it is also not correct to say that "the weight of the snow pushes...", as the "weight" cannot act on something.
- P2, L9. "over solely thermal growth" is confusing.
Rephrased.
- P2, L11-12. This sentence is redundant with itself. Do you mean that the scales are poorly known because of their limited observations?
We meant that the spatial and temporal variability of processes such as flooding and superimposed ice formation are poorly known, because of limited knowledge of snow cover distribution and properties. Rephrased, see P2,L14-15 in the revised manuscript.
- P2, L13-15. Sublimation also plays a role.
Good point! Added.
- P2, L22-23. Where is this often observed?
We found the word "often" too vague and rephrased the sentence, including appropriate references (see P2,L25-28 in the revised manuscript).
- P2, L23. Shallow relative to what?
Similar to our response to a similar comment by Reviewer #1: It was indeed poorly formulated, and we took "shallow" with reference to alpine snowpacks. We rephrased the sentence.
- P3, L1-2. This sentence needs to be a little more specific. There are remote sensing methods of snow that have no reliance on brightness temperatures (e.g. dual laser and radar altimetry).
Good point! Added, with the note that snow properties (depth and density) are still a source of uncertainty in laser or radar altimetry (see P3,L4-7 in the revised manuscript).
- P3, L13. A sentence could be added here to really set the stage. Something along the lines of: "In this analysis, we apply SNOWPACK to the Antarctic sea-ice environment and demonstrate its ability to successfully reproduce snow-on-sea ice conditions..." etc.
Thank you for the suggestion, we inserted a similar sentence (P3,L22-23 in the revised manuscript).

- P3, L22. Typo. "layer's"
Corrected.
- P4, L15. Why does the brine freeze instantly? Wouldn't brine salinity increase with decreasing temperature until it reached the eutectic point for salt? Lines 18-19 and 22 and simulation results make me think this process is being accounted for, but this should be clarified in the text here.
We indeed wanted to express here that with decreasing temperature the brine volume decreases such that the eutectic point for the brine corresponds to the temperature of the surrounding ice or snow. We rephrased the manuscript (see P4,L29-31 in the revised manuscript).
- P5, L11. For readers unfamiliar with the bucket scheme, a single sentence concisely describing its purpose would be appropriate here.
We actually decided to remove the description and simulation of the bucket scheme with fixed, prescribed salinity profiles. We encountered that the implementation was flawed, as the bucket scheme may transport part of the brine downward when it exceeds the size of the "bucket". However, the thermodynamics routine would melt additional sea ice to maintain thermal equilibrium, which in turn again would be transported downward by the water transport scheme. This is undesirable and we were not able to come up with a solution within the time frame of the review process.
- P9, L21-22. Brine channels become closed off during sea ice growth and thus much of the sea ice below sea level is unsaturated. How might this difference between the model and real-life play into the results?
We are not certain if the reviewer means the same with the term saturation. We consider saturated ice as ice where the pore space is completely depleted and the sea ice only consists of freshwater ice and brine. The hydraulic conductivity in our model regulates the flow of brine. So in our model approach, a zero hydraulic conductivity would stop any brine migration through the model domain. This implies, however, that the pressure head and degree of saturation would remain constant in time. However, the initial profile used to set-up the model would also affect the initial and temporal evolution of the brine. We think that the influence of the calculated flooding is relatively small. Pore space in snow is so much larger than in the underlying ice, that very soon ocean water will reach the snowpack. Ultimately, the model we propose is particularly aimed at simulating the snow covering sea ice. Nevertheless, the framework we propose for liquid water flow coupled to the transport equation for salinity may have potential for future development.
- Figure 1. The dates are not clear at the beginning of the buoy trajectories.
We improved the figure.
- P11, L6. Do you mean here that comparisons between the model simulations and IMB data were made with regard to the sea ice properties only?
Yes, due to the way the IMB was installed, we only have the temperature profile in the ice part, and can thus only assess ice temperature and ice thickness. We rephrased the manuscript (see P11,L1-4 in the revised manuscript).
- P11, L16-17. Please check the dates here. One of them is incorrect.
We are not sure what the reviewer meant here, but we rephrased the sentence (see P12,L6-9 in the revised manuscript).
- P11, L23. Typo "was" to "were"
Corrected.
- P12, L1-2. Unless the sea ice is melting and drained, it would retain brine content above sea level.
We mention now that it is a simplification of reality to assign zero brine volume to sea ice above sea level (see P12,L24-27 in the revised manuscript).
- P12, L2-3. Where do these initial values come from, and how sensitive are the results to them?
We provide some additional explanation now in the manuscript. Note that the initial snow covers in our simulations are very small (10 cm or less). The majority of the snowpack builds up during the model simulations. See P12,L29-31 in the revised manuscript).

- P12, L11. "measured snow depth" Measured snow depth from the snow buoys is fraught with uncertainties due to blowing and drifting snow, both during and outside of snowfall events. How representative is it to take these measured snow depth increases as snowfall events for the model?

We are not certain where the reviewer aims at. Is it about snow drift disturbing the snow height measurements? First of all, each individual sensor checks for signal consistency and by having four snow height sensors on a buoy, the consistency between the sensors can also be verified. If it is about snow drift removing snow, we would argue that this is precisely why the snow buoy system is advantageous, as it allows for an assessment of the actual amount of snow on sea ice.

- P12, L12. Typo. Change "is below" to "is less than the"
Corrected.
- P12, L21. Not all sea ice below sea level is saturated, and not all sea ice above sea level is salt-free. The model assumptions don't show geophysically-realistic vertical profiles of bulk salinity (please see the following for examples: <https://apps.dtic.mil/dtic/tr/fulltext/u2/a312027.pdf>). It would be worthwhile to discuss the discrepancies with observations, and possible pathways for future improvement of their representation. It would also be worthwhile to discuss the limited representation of brine salinity – it also does not reflect a geophysically-realistic profile in this first example.

The document, which is pointed to here, shows mainly information about the relationship between floe thickness and average bulk salinity. Only one figure shows vertically resolved bulk salinity profiles. The field data shows that typically, bulk salinity decreases with floe thickness, which is often explained due to gravity drainage of dense brine. This is something very challenging to reproduce. We provide now a discussion of our results with possible future model improvements in a new Outlook section (see P28,L24-25 in the revised manuscript).

- Figure 2 caption "dry sea ice" Technically, this is dry, porous freshwater ice.
Thanks for the suggestion. Corrected.
- P13, L5-6. sea level doesn't stay below the snow-ice interface for the simulation in panel b, does it?
Indeed, this was poorly formulated. We misinterpreted ERA5 precipitation rates, and after updating the data set, we forgot to adjust the manuscript accordingly. We rephrased the sentence (see P15,L25-28 in the revised manuscript).
- Figure 3. It would be informative to show the temperature difference between panels b and c.
We created a separate plot for the difference plots, so we can show the difference between a and c, as well as b and c. Please find the new figure 6 in the revised manuscript.
- Why are there intermittent decreases in snow depth in panel a compared to what appears to be a steady increase in snow depth in panel b? In panel a, is the model being re-adjusted to the measured snow depth at each timestep or is it melting?
As we explain now in P14,L14-15 in the revised manuscript, there is no correction in the model when simulated snow depth is above measured snow depth. Decreases in modelled snow depth are due to sublimation and snow melt. The precipitation from ERA5 seems to result in a thicker snowpack on sea ice than found in the snow height driven simulations. We now show cumulative time series of ERA5 precipitation in newly added figures (see Figs. 2 and 3 in the revised manuscript), which show that there is a constant increase in precipitation. This could mask snow depth decreases when there is melt.
- It would be helpful to increase the y-axis in all of the panels so that readers can see the full range in snow depth. Alternatively, zoomed in panels could be helpful.
We improved the figure.
- P14, L12. What is meant by an overestimated surface energy balance? If the energy budget is in balance, how can it be overestimated?
It was indeed poorly phrased, but we meant that the incoming energy could be overestimated, or the outgoing energy be underestimated. We rephrased the sentence.

- P13, L12-13. Do you mean here that snow density was too small, and thus, its insulating capacity was too high, keeping the sea ice "warmer" relative to the observed temperatures?
We assume this refers to P14. It's indeed what was meant here. We rephrased this sentence to be more clear.
- P15, L7-8. Isn't good agreement expected with this approach?
Written as it was, it was indeed a trivial statement. We rephrased the paragraph.
- P15, L11. How much is slightly overestimated? It's cut off in the figure.
We misinterpreted ERA5 precipitation rates, and after updating the data set, we forgot to recheck the figures and text in the manuscript. We updated the figure and rephrased the text.
- P15, L17-18. It would be helpful to state when (which date) flooding occurs since it's not apparent in the figure.
Actually, there is no flooding occurring. We meant to say here that the added weight of snow is increasing the bottom pressure, leading to an influx of saline water. The freeboard remains positive, i.e., the sea level stays below the snow–ice interface. We rephrased the sentence (see P18,L31-32 in the revised manuscript).
- P15, L28-29. Can difference plots be shown? How well do they compare?
We removed the simulation using the bucket scheme and fixed salinity profiles, as we found there were some discrepancies in this model approach, which could not be easily resolved.
- Figure 4a. The boundary between the snow and sea ice looks unusual. Is LWC actually zero in the uppermost layers of the ice surface or is there a gap between the snow and ice in this figure?
There is no gap in the snow and ice in the figure. There is low liquid water content just above the sea level due to capillary suction. We now explicitly mention this: see P18,L26-27 in the revised manuscript.
- Figure 4b. Why does the bulk salinity remain constant both vertically and horizontally in panel b? Why might this differ so much from observations? (please see the following for profile examples: <https://apps.dtic.mil/dtic/tr/fulltext/u2/a312027.pdf>).
When we initialize the simulations with a constant brine salinity profile, the only way the simulations would show a temporally varying bulk salinity is when there is vertical flow of brine. In the simulations this typically happens upon new snow accumulations adding weight. In reality there is also gravity drainage of dense brine, which is not reproduced by our model. We discuss this now in an outlook section at the end of the manuscript (see P28 in the revised manuscript).
- Figure 5 caption, dry snow is colored grey. This description is incorrect here?
Corrected, it was due to copying figure captions without realizing the sentence was not valid for this figure.
- Figure 6. This is a nice simulation experiment. For figure 6d, what mechanism is causing the brine salinity to increase in the uppermost part of the snow pack during March 2015?
The brine salinity appearing in the near surface layer resulted from numerical rounding errors when calculating bulk salinity, which, given the low temperatures, resulted in very high brine salinities. This rounding error has been resolved now by revising the model source code.
- Also, what is happening with brine salinity in the lower most ice layers from Sept - Dec 2015?
Issue resolved.
- Figure 8d. How can there be brine in the topmost layers of the snow pack?
Similar to the previous issue: The brine salinity appearing in the near surface layer resulted from numerical rounding errors when calculating bulk salinity, which, given the low temperatures, resulted in very high brine salinities. This rounding error has been resolved now by revising the model source code.
- P25, L9-10. While I agree with this statement, to bolster it, more simulations forced by ERA5 snowfall events rather than the selected events by the IMB data should be conducted and, at the very least, shown in supplementary material. Many current approaches for snow depth simulations are simplified and exclude loss terms. It would be informative to see if this approach is more effective in simulating snow depth due to

its sophistication.

We rephrased this paragraph. We plan on extending the analysis for the other snow buoys, but we feel that it would tend to be out of the scope for a model description paper.

David Ham, Executive Editor

Thank you for your efforts to make your code and dat available. There are still some aspects which do not conform to GMD policy and which need to be changed in the revised manuscript.

Thank you for the comments. Please find our responses below.

Links to SVN repositories

Links to SVN repositories are not permanent archives of the code. Should the project, for example, change revision control system then these links will go dead and the version numbers will no longer identify the code. Please persistently and publicly archive the exact version of the code used, and cite the resulting DOI accordingly. Most authors choose to use Zenodo (<https://zenodo.org>) for this, though any archive compliant with GMD policy will do.

We understand the need for a unique identification of the source code. However, we decided against uploading the source code to Zenodo and acquiring a unique DOI, because we always encourage users to use the latest version of the model. We therefore decided to include the source code in the Online Supplement, together with the run files and scripts.

No run or analysis scripts

It is at least not clear where the code is that ran the model (model input and configuration files, for examples), nor the code that was used to analyse the results and produce the figures and numerical results in the manuscript. These also form part of the code supporting the manuscript and should be published.

Please note that we included all the model input and configuration files in the Online Supplement to the manuscript. The README.txt file contained for each figure in the manuscript the appropriate command to execute SNOWPACK. We now added the postprocessing and plotting scripts as well.

Data citations are underspecified

The data from Meereisportal is insufficiently clearly specified (which dataset, which version, which dates etc.) The site itself contains information on how it should be cited, please follow it (http://data.meereisportal.de/gallery/index_new.php?lang=en_US&survey=&active-tab1=citation&active-tab2=). In particular, URLs can change, so just citing URLs is difficult. Further, it does not seem to be the case that all the data used has been cited. For example, there is mention elsewhere in the manuscript of the use of ERA5 data. Please ensure that all the data and code used in the production of the manuscript is precisely identified and cited from the code and data availability section. For further details see the GMD code and data availability policy: https://www.geoscientific-model-development.net/about/code_and_data_policy.html

We now refer the Snow Buoys with the specific DOIs. Thermistor Buoy 2016T41 does not have a unique identifier or version number.

References

Celia, M. A., Bouloutas, E. T., and Zarba, R. L.: A general mass-conservative numerical solution for the unsaturated flow equation, *Water Resour. Res.*, 26, 1483–1496, <https://doi.org/10.1029/WR026i007p01483>, 1990.

Haverkamp, R. and Vauclin, M.: A note on estimating finite difference interblock hydraulic conductivity values for transient unsaturated flow problems, *Water Resour. Res.*, 15, 181–187, <https://doi.org/10.1029/WR015i001p00181>, 1979.

Notz, D. and Worster, M. G.: Desalination processes of sea ice revisited, *J. Geophys. Res.*, 114, <https://doi.org/10.1029/2008JC004885>, URL <https://agupubs.onlinelibrary.wiley.com/doi/abs/10.1029/2008JC004885>, 2009.

Østerby, O.: Five Ways of Reducing the Crank–Nicolson Oscillations, *BIT Numerical Mathematics*, 43, 811–822, <https://doi.org/10.1023/B:BITN.0000009942.00540.94>, URL <https://doi.org/10.1023/B:BITN.0000009942.00540.94>, 2003.

Version 1 of a sea ice module for the physics based, detailed, multi-layer SNOWPACK model

Nander Wever^{1,2,3}, Leonard Rossmann⁴, Nina Maaß⁵, Katherine C. Leonard^{1,2,6}, Lars Kaleschke⁴, Marcel Nicolaus⁴, and Michael Lehning^{2,3}

¹Department of Atmospheric and Oceanic Sciences, University of Colorado Boulder, Boulder, CO, USA.

²CRYOS, School of Architecture, Civil and Environmental Engineering, EPFL, Lausanne, Switzerland.

³WSL Institute for Snow and Avalanche Research SLF, Davos, Switzerland.

⁴Alfred Wegener Institute, Helmholtz Centre for Polar and Marine Research, Bremerhaven, Germany.

⁵University of Hamburg, Institute of Oceanography, CEN, Germany.

⁶Cooperative Institute for Research in Environmental Science (CIRES), University of Colorado Boulder, Boulder, CO, USA.

Correspondence: NANDER WEVER (nander.wever@colorado.edu)

Abstract. Sea ice is an important component of the global climate system. The presence of a snowpack covering sea ice can strongly modify the thermodynamic behaviour of the sea ice, due to the low thermal conductivity and high albedo of snow. The snowpack can be stratified and change properties (density, water content, grain size and shape) throughout the seasons. Melting snow provides fresh water which can form melt ponds, or cause flushing of salt out of the underlying sea ice, while

5 flooding of the snow layer by saline ocean water can strongly impact both the ice mass balance and the freezing point of the snow. To capture the complex dynamics from the snowpack, we introduce modifications to the physics-based, multi-layer SNOWPACK model to simulate the snow-sea ice system. Adaptations to the model thermodynamics and a description of water and salt transport through the snow – sea ice system by coupling the transport equation to the Richards equation were added.

These modifications allow the snow microstructure descriptions developed in the SNOWPACK model to be applied to sea ice 10 conditions as well. Here, we drive the model with data from Snow and Ice Mass-balance Buoys installed in the Weddell Sea in Antarctica. The model is able to simulate the temporal evolution of snow density, grain size and shape, and snow wetness. The model simulations show abundant depth hoar layers and melt layers, as well as superimposed ice formation due to flooding and percolation. Gravity drainage of dense brine is underestimated as convective processes are so far neglected. Furthermore, with increasing model complexity, detailed forcing data for the simulations is required, which is difficult to acquire due to limited

15 observations in polar regions.

1 Introduction

Sea ice is an important component of the global climate system (e.g., Goosse and Fichefet, 1999; Ferrari et al., 2014). During the freezing process of ocean water, salt is expelled from the ice and dense, saline water is formed. The negative buoyancy of the resulting dense water is an important mechanism driving global ocean circulation (e.g., Gordon, 1988). Sea ice also forms 20 the interface between the ocean and the atmosphere for extended periods of time, altering the surface energy balance (e.g., Ledley, 1991; Brandt et al., 2005; Perovich et al., 2011).

Antarctic sea ice is largely snow covered (Allison et al., 1993), which has major implications for the energy and mass balance of sea ice (Eicken et al., 1995; Massom et al., 2001). The layer of snow strongly modifies the energy balance both via its high albedo (Grenfell and Perovich, 1984; Brandt et al., 2005; Perovich et al., 2011), and through the thermal conductivity of snow, which insulates the sea ice and limits ice growth (Maykut and Untersteiner, 1971; Sturm et al., 2002b). In summer, however, 5 the high albedo of the snow cover may limit ice melt (e.g., Curry et al., 1995). The thermal conductivity of snow also varies widely based on the snow microstructural properties, indicating the need to explicitly consider those properties and their spatial and vertical variability (Calonne et al., 2011; Sturm et al., 2002b).

Although the effect of snow on the energy balance reduces sea ice growth, it can also provide a positive contribution to the mass balance of the sea ice. Particularly on Antarctic sea ice, it is regularly observed that the snow cover, due to its weight, 10 pushes the sea ice below sea level. Flooding then may occur via cracks or through the brine channels. Refreezing of the flooded layer is an important mechanism increasing the ice mass in addition to basal thermodynamic growth in the Southern Ocean (Eicken et al., 1994; Jeffries et al., 1997). Snow meltwater or rain percolating and accumulating on top of the ice can also (re)freeze and cause the formation of superimposed ice (Haas et al., 2001; Nicolaus et al., 2003; Obleitner and Lehning, 2004).

The spatial and temporal variability of these processes is poorly known due to limited knowledge of snow cover distribution 15 and properties.

Assessing snow amounts on sea ice from atmospheric forcing alone is not straight-forward, as the local precipitation is redistributed by wind, and an unknown fraction of precipitation never accumulates over level ice as it is either blown into leads or accumulates in the lee of surface topography (Déry and Tremblay, 2004; Leonard and MakSYM, 2011; Trujillo et al., 2016; Liston et al., 2018; Petty et al., 2018), or is lost due to drifting snow sublimation (e.g., Wever et al., 2009). These processes 20 result in snow depth patterns and accumulation patterns that are typically spatially highly variable (Trujillo et al., 2016; Haas et al., 2017). Also, the wind redistribution and smoothing effect of the snow cover modifies the aerodynamic roughness of the sea ice surface, influencing the momentum flux between atmosphere and sea ice (Andreas, 2002; Weiss et al., 2011) and consequently the large-scale movement of sea ice (Tremblay and Mysak, 1997).

Snow stratigraphy over sea ice can also be highly variable in space and time, and exhibit complex microstructural layering 25 (Massom et al., 1998, 2001; Nicolaus et al., 2009). Strong temperature gradients over shallow snow covers can lead to facetting and grain growth, resulting in layers with faceted depth hoar crystals (Toyota et al., 2007; Lewis et al., 2011). Inhomogeneities caused by wind slabs, ice layers and melt-freeze crusts have been reported for both Arctic and Antarctic sea ice (e.g., Massom et al., 1997; Sturm et al., 2002a; Gallet et al., 2017; Merkouriadi et al., 2017; Arndt and Paul, 2018). As snow on sea ice is typically up to a few decimeter for extended periods of time, and accumulation events are small, it is a challenge for numerical 30 models to capture the vertical variability in the snow cover accurately.

Water transport processes in the snowpack can have a strong impact on the snow microstructure and the salinity distribution in the snow – sea ice system. Surface melt can create downward water percolation, which can refreeze lower down in the snowpack as ice layers or form superimposed ice (Nicolaus et al., 2009), or (particularly in the Arctic) form melt ponds. Upon warming of the underlying sea ice, increased hydraulic conductivity from expanding brine channels may cause freshwater to 35 flush salt out of the underlying ice (e.g., Notz and Worster, 2009). Upward motion of liquid water has also been observed

due to capillary forces (Massom et al., 1998, 2001). Capillary wicking can move salt upward, creating a salty slush layer and frost flowers at the ice surface (Rankin et al., 2002; Domine et al., 2004), which may get buried beneath snow after snow fall, impacting the salinity and water content of the lowest snow layers.

The snow cover is also important for deriving sea ice thickness and snow depth from satellite remote sensing. For example, 5 the microwave signature (e.g., Markus and Cavalieri, 1998; Drinkwater and Crocker, 1988; Powell et al., 2006) and the radar penetration (e.g., Willatt et al., 2010; Ricker et al., 2014) of snow-covered sea ice depend on the properties and layering of the snow.

A wide range of sea ice models have been developed (e.g., Bitz and Lipscomb, 1999; Maksym and Jeffries, 2000; Ukita and Martinson, 2001; Huwald et al., 2005; Griewank and Notz, 2013; Turner and Hunke, 2014). Due to the important role of snow 10 on sea ice, many sea ice models include a description of the snow cover in their models (Lecomte et al., 2011; Notz, 2012). The most important factors considered by sea ice models is the albedo and the insulating effect of the snow. Several studies used the snow thermodynamics model SNTHERM, either using the internal sea ice module or coupled to a sea ice model (Jordan et al., 1999; Nicolaus et al., 2006; Chung et al., 2010; Fuller et al., 2015) to improve the thermodynamical upper boundary condition for sea ice, and assessing the snow microstructure on sea ice.

15 Rather than improving the representation of snow in an existing sea ice model, this paper presents a new sea ice module developed for the physics-based, detailed, multi-layer snow cover model SNOWPACK. Our motivation is that the SNOWPACK model has a long development history with a focus on accurately representing physical processes in the snow cover. This includes a detailed representation of snow microstructure as well as liquid water flow processes (Bartelt and Lehning, 2002; Lehning et al., 2002a, b; Wever et al., 2015, 2016). The model has previously been successfully applied in Polar regions. For 20 example, for the Greenland Ice Sheet (Steger et al., 2017), it was found to provide accurate simulations of water flow and refreezing processes. An application to the Antarctic Plateau (Groot Zwaftink et al., 2013) showed good agreement for new snow density and temperature profiles in a drifting snow dominated environment. Here, we apply the new SNOWPACK module to the Antarctic sea ice environment and demonstrate its ability to successfully simulate snow on sea ice conditions.

2 Methods

25 The SNOWPACK model has seen a long development history regarding snow processes. The model calculates the snow energy balance, the resulting temperature distribution, snow settling (densification), liquid water flow and the evolution of snow microstructure. The snow microstructure is described by four parameters: grain size, bond radius, sphericity and dendricity. Grain size is considered the average grain size (Baunach et al., 2001) and bond radius is defined to be the minimum constriction in the connection between to grains (see Fig. 2 in Lehning et al. (2002a)). As defined in Brun et al. (1992), dendricity describes 30 how much of the original crystal shapes are still remaining in a snow layer, where 1 corresponds to perfect dendritic snow, and 0 to perfect rounds or faceted snow. Sphericity describes the ratio of rounded versus angular shapes, where 1 denotes perfectly round shapes, and 0 describes perfectly faceted shapes. Governing state equations describe the time evolution of

these parameters given snow temperature, density, liquid water content (LWC), etc. The full model description is presented in Bartelt and Lehning (2002) and Lehning et al. (2002a, b).

The basic model structure of SNOWPACK is congruent with the mushy-layer theory for sea ice (Hunke et al., 2011; Turner and Hunke, 2014). The model is 1-dimensional, with an arbitrary number of vertical layers of arbitrary depth. Typical layer 5 depth, however, is 1-2 cm. Each layer's total volume is subdivided into a part consisting of respectively ice, water and air. Henceforth these layers are called "snow" layers. Note that SNOWPACK also considers soil as a category, which is hereafter ignored in the context of sea ice.

The sea ice extension of the model provides modifications to the model code to include the effect of salinity on thermal properties and liquid water flow. Furthermore, ice growth and melt at the bottom of the domain is assessed. Flooding is 10 considered to occur only in one-dimension, and lateral advection of liquid water is ignored (Maksym and Jeffries, 2000).

Below, we detail the modifications of the SNOWPACK model to make it suitable for sea ice simulations. The modifications are implemented in the main version of SNOWPACK, and sea ice specific settings are only needed in the configuration files for the model. The code base of the SNOWPACK model is the same and future developments in other parts of the code will also be directly available for the sea ice version.

15 2.1 Heat Equation and Thermodynamics

SNOWPACK solves the heat equation using finite elements, as described in Bartelt and Lehning (2002), allowing to have a simulated snow surface temperature as well as a temperature at the bottom of the snow column. Each snow layer, called element, has two nodes with the adjacent elements. Several modifications were necessary to take into account the effect of salinity on thermodynamical properties.

20 First, it is assumed that all salt is concentrated in the liquid water in the brine pockets and that the volumetric ice content is free of salt, such that one can write:

$$S_b = \frac{S}{\theta}. \quad (1)$$

Here, S is the bulk salinity (g kg^{-1}), S_b is the brine salinity (g kg^{-1}) and θ is the volumetric LWC ($\text{m}^3 \text{ m}^{-3}$).

The melting point T_m (K) of each snow element can then be expressed as a function of brine salinity by the commonly used 25 relationship (Assur, 1960):

$$T_m = -\mu S_b + T_0, \quad (2)$$

where μ is a constant ($0.054 \text{ K} (\text{g kg}^{-1})^{-1}$) and T_0 is the melting point of fresh water (273.15 K). Eq. 2 is valid between 0°C and -6°C (Vancoppenolle et al., 2019).

To solve the heat equation, we assume equilibrium between the element temperature T_e (K) and the brine melting point 30 T_m . When the ice is heating (cooling), brine volume is assumed to increase (decrease) instantaneously by phase changes in the surrounding ice, in order to maintain $T_e = T_m$. This is achieved by feeding back the energy associated with the phase change as a source/sink term in the heat equation (see Eq. 3 in Bartelt and Lehning (2002)). Note that the latent heat released when water

freezes increases the temperature locally, and vice versa. These effects on local temperature would reduce the energy released during freezing or energy available for melt. Additionally, the refreezing or melting of ice impacts brine salinity and thereby the melting temperature. These competing processes slow down the convergence in the solver for the heat equation, which can be mitigated by providing an improved estimate of the melting temperature which satisfies: (i) the condition provided by Eq. 5 1 for the new LWC, (ii) Eq. 2 for the new melting temperature given the new brine salinity, and (iii) the change in ice content for the given deviation of the new element temperature from the melting point, by algebraically solving these three conditions with the three unknowns.

The bottom node of the domain represents the interface between sea ice and ocean and its temperature is prescribed as a Dirichlet boundary condition using the freezing temperature of the ocean water, which is determined by the prescribed ocean 10 salinity (set to 35 g kg^{-1} in this study). Typically heat is advected into the sea ice from the ocean below, referred to as the ocean heat flux. We determine the net energy loss or gain at the bottom node, given the prescribed ocean heat flux and the internal heat flux in the lowest sea ice element. This net energy is translated into bottom ice growth or melt.

An uncertainty for ice growth is the ice porosity of the newly formed ice. We apply a similar approach to the one presented in Griewank and Notz (2013), where an ice content threshold is defined. When the lowest element has an ice content below 15 this value, the net energy is used to create a new ice element with a brine salinity equal to ocean salinity (Vancoppenolle et al., 2010). Otherwise, the bottom element grows in length. We set a threshold of $0.99 \text{ m}^3 \text{ m}^{-3}$, which we also prescribe as the maximum allowed ice content of a single layer. Mass loss is applied by reducing the element length.

2.2 Brine Dynamics

The SNOWPACK model is equipped with a solver for the full Richards equation for transport in porous media (Wever et al., 20 2014). Here, we modified the solver for the Richards equation to account for density variations and couple the Richards equation to a transport equation for salinity. This provides an explicit treatment of brine dynamics. First, the Richards equation solves the liquid water flow in the snow – sea ice system, keeping the salinity constant with time. After each integration of the Richards equation, the advection-diffusion equation is solved for the same time step under the assumption of constant liquid water fluxes. The time step is limited to a maximum of 15 minutes, although stability criteria for both the Richards equation 25 as well as the advection-diffusion equation for salinity may impose additional, stricter, time constraints. Below, we detail how this scheme for liquid water transport was modified for sea ice.

2.2.1 Richards Equation for Water Flow

The mixed form of the Richards equation reads:

$$\frac{\partial \theta}{\partial t} - \frac{\partial}{\partial z} \left[\frac{\kappa}{\eta} \frac{\partial p}{\partial z} \right] - s = 0, \quad (3)$$

30 where t is time (s), z is the vertical coordinate (m), κ is the permeability (m^2), η is the viscosity (m s^{-2}) and s is a source/sink term ($\text{m}^3 \text{ m}^{-3} \text{ s}^{-1}$). The pressure p can be considered the sum of water potential and gravity potential:

$$p = \rho gh + \rho g z \cos(\gamma) \quad (4)$$

where h is the pressure head (m), g is the gravitational acceleration (m s^{-1}), ρ the density of the flowing liquid (kg m^{-3}) and γ is the slope angle. Because SNOWPACK can be used in sloped terrain, we keep this term for completeness of the model description, although γ is obviously 0 for sea ice.

The density of liquid water (ρ) is adjusted for salinity according to:

$$5 \quad \rho = \rho_w + \beta S_b, \quad (5)$$

where ρ_w is the density of fresh liquid water (1000 kg m^{-3}), β is a salinity coefficient, approximated as $0.824 \text{ kg}^2 \text{ g}^{-1} \text{ m}^{-3}$ (Massel, 2015, Appendix A).

The permeability κ is replaced by the hydraulic conductivity K , which relates to κ via:

$$K = \kappa \frac{\rho g}{\mu}, \quad (6)$$

10 where μ is the dynamic viscosity of water ($0.001792 \text{ kg (m s)}^{-1}$).

A critical assumption in the typical application of the Richards equation is that both g and ρ are constant in time and z , and consequently can be eliminated from the equation. Due to salinity variations in sea ice, variations of density of the flowing liquid can occur and are actually considered the driving mechanism in the temporal and spatial evolution of the salinity of sea ice.

15 Therefore, we rewrite the Richards equation for sea ice by considering ρ as a function of z and only eliminating g , arriving at:

$$\frac{\partial \theta}{\partial t} - \frac{\partial}{\partial z} \left[\frac{K}{\rho} \frac{\partial}{\partial z} (\rho h + \rho z \cos(\gamma)) \right] - s = 0, \quad (7)$$

As outlined in Wever et al. (2014), the Richards equation is implemented in SNOWPACK by the discretization proposed by Celia et al. (1990). The backward Euler approximation in time coupled with a simple Picard iteration, as shown in Eq. 14 of 20 Celia et al. (1990), becomes, for Eq. 7:

$$\frac{\theta^{n+1,m+1} - \theta^n}{\Delta t} - \frac{\partial}{\partial z} \left(\frac{K^{n+1,m}}{\rho} \frac{\partial \rho h^{n+1,m+1}}{\partial z} \right) - \cos(\gamma) \frac{\partial K^{n+1,m}}{\partial z} - \cos(\gamma) \frac{\partial}{\partial z} \left(\frac{K^{n+1,m} z}{\rho} \frac{\partial \rho}{\partial z} \right) - s = 0, \quad (8)$$

where n and m denote the time and iteration level, respectively. Here, we have used to chain rule to write:

$$\frac{\partial}{\partial z} \left[\frac{K}{\rho} \frac{\partial}{\partial z} (\rho z) \right] = \frac{\partial}{\partial z} \left[K \frac{\partial z}{\partial z} \right] + \frac{\partial}{\partial z} \left[\frac{K}{\rho} z \frac{\partial \rho}{\partial z} \right] = \frac{\partial K}{\partial z} + \frac{\partial}{\partial z} \left[\frac{K}{\rho} z \frac{\partial \rho}{\partial z} \right] \quad (9)$$

The last term on the right hand side expresses the liquid water flow driven by density differences.

25 After applying a Taylor expansion to Eq. 15 of Celia et al. (1990), and defining $\delta^m \equiv \rho h^{n+1,m+1} - \rho h^{n+1,m}$, we arrive at:

$$\left(\frac{1}{\Delta t} \frac{C^{n+1,m}}{\rho} \right) \delta^m + \frac{\theta^{n+1,m} - \theta^n}{\Delta t} - \frac{\partial}{\partial z} \left(\frac{K^{n+1,m}}{\rho} \frac{\partial \rho h^{n+1,m+1}}{\partial z} \right) - \cos(\gamma) \frac{\partial K^{n+1,m}}{\partial z} - \cos(\gamma) \frac{\partial}{\partial z} \left(\frac{K^{n+1,m} z}{\rho} \frac{\partial \rho}{\partial z} \right) - s = 0.$$

Finally, Eq. 16 in Celia et al. (1990) becomes:

$$5 \quad \left(\frac{1}{\Delta t} \frac{C^{n+1,m}}{\rho} \right) \delta^m - \frac{\partial}{\partial z} \left(\frac{K^{n+1,m}}{\rho} \frac{\partial \delta^m}{\partial z} \right) \\ = \frac{\partial}{\partial z} \left(\frac{K^{n+1,m}}{\rho} \frac{\partial \rho h^{n+1,m+1}}{\partial z} \right) + \cos(\gamma) \frac{\partial K^{n+1,m}}{\partial z} + \cos(\gamma) \frac{\partial}{\partial z} \left(\frac{K^{n+1,m}}{\rho} \frac{\partial \rho}{\partial z} \right) - \frac{\theta^{n+1,m} - \theta^n}{\Delta t} + s \quad (11)$$

After applying the standard finite difference approximation in space, Eq. 16 in Celia et al. (1990) translates into (i denoting the spatial coordinate):

$$10 \quad \frac{C_i^{n+1,m}}{\rho_i} \frac{\delta_i^m}{\Delta t} - \frac{1}{(\Delta z)^2} \left[\frac{K_{i+1/2}^{n+1,m}}{\rho_{i+1/2}} (\delta_{i+1}^m - \delta_i^m) - \frac{K_{i-1/2}^{n+1,m}}{\rho_{i-1/2}} (\delta_i^m - \delta_{i-1}^m) \right] \\ = \frac{1}{(\Delta z)^2} \left[\frac{K_{i+1/2}^{n+1,m}}{\rho_{i+1/2}} (\rho_{i+1} h_{i+1}^{n+1,m} - \rho_i h_i^{n+1,m}) - \frac{K_{i-1/2}^{n+1,m}}{\rho_{i-1/2}} (\rho_i h_i^{n+1,m} - \rho_{i-1} h_{i-1}^{n+1,m}) \right] \\ + \cos(\gamma) \frac{K_{i+1/2}^{n+1,m} - K_{i-1/2}^{n+1,m}}{\Delta z} + \cos(\gamma) \frac{\frac{K_{i+1/2}^{n+1,m}}{\rho_{i+1/2}} z_{i+1/2} \frac{\rho_{i+1} - \rho_i}{\Delta z} - \frac{K_{i-1/2}^{n+1,m}}{\rho_{i-1/2}} z_{i-1/2} \frac{\rho_i - \rho_{i-1}}{\Delta z}}{\Delta z} - \frac{\theta_i^{n+1,m} - \theta_i^n}{\Delta t} + s_i \\ \equiv (R_i^{n+1,m})_{\text{MPFD}}, \quad (12)$$

where the notation R_{MPFD} is kept for consistency with Celia et al. (1990). The system of equations described by Equation 12 forms a tri-diagonal matrix. As in Wever et al. (2014), the function `DGTSV` from the `LAPACK` library (Anderson et al., 1999) is called to compute the solution. When `LAPACK` is not available, or not selected on compile time, the Thomas algorithm is used as the implemented default alternative, which does not depend on external libraries. However the Thomas algorithm is not the preferred option as in contrast to `DGTSV`, it lacks partial pivoting and may suffer from numerical instabilities.

2.2.2 Transport Equation for Salinity

The governing equation in 1-dimension for concentration describes the change in salinity as a combination of a diffusion and 20 advection process:

$$\frac{\partial}{\partial t} (\theta S_b) - \frac{\partial}{\partial z} \left(D \theta \frac{\partial S_b}{\partial z} \right) - \frac{\partial}{\partial z} (q S_b) - s_{sb} = 0 \quad (13)$$

Where D is the diffusion coefficient ($\text{m}^2 \text{s}^{-1}$), considered here, as a first approximation, independent of temperature. In this study, D is set as $10^{-10} \text{ m}^2 \text{s}^{-1}$ (Poisson and Papa, 1983). q denotes the liquid water flux (m s^{-1}) and s_{sb} is a source/sink term for salinity (assumed here to be $0 \text{ g kg}^{-1} \text{s}^{-1}$).

An implicit numerical scheme for Equation 13 becomes in discretized form (n and i again denoting time and spatial level, respectively):

$$\begin{aligned}
& \frac{\left(\theta_i^{n+1} S_{b,i}^{n+1} - \theta_i^n S_{b,i}^n\right)}{\Delta t} \\
5 & - f \left[\left(\frac{2D_{i+1}^n \theta_{i+1}^{n+1} S_{b,i+1}^{n+1}}{\Delta z_{\text{up}} (\Delta z_{\text{up}} + \Delta z_{\text{down}})} - \frac{2D_i^n \theta_i^{n+1} S_{b,i}^{n+1}}{(\Delta z_{\text{up}} \Delta z_{\text{down}})} + \frac{2D_{i-1}^n \theta_{i-1}^{n+1} S_{b,i-1}^{n+1}}{\Delta z_{\text{down}} (\Delta z_{\text{up}} + \Delta z_{\text{down}})} \right) \right] \\
& - (1-f) \left[\left(\frac{2D_{i+1}^n \theta_{i+1}^n S_{b,i+1}^n}{\Delta z_{\text{up}} (\Delta z_{\text{up}} + \Delta z_{\text{down}})} - \frac{2D_i^n \theta_i^n S_{b,i}^n}{(\Delta z_{\text{up}} \Delta z_{\text{down}})} + \frac{2D_{i-1}^n \theta_{i-1}^n S_{b,i-1}^n}{\Delta z_{\text{down}} (\Delta z_{\text{up}} + \Delta z_{\text{down}})} \right) \right] \\
& - f \left[\left(\frac{q_{i+1}^n S_{b,i+1}^{n+1} - q_{i-1}^n S_{b,i-1}^{n+1}}{(\Delta z_{\text{up}} + \Delta z_{\text{down}})} \right) \right] - (1-f) \left[\left(\frac{q_{i+1}^n S_{b,i+1}^n - q_{i-1}^n S_{b,i-1}^n}{(\Delta z_{\text{up}} + \Delta z_{\text{down}})} \right) \right] - s_{\text{sb}} = 0 \quad (14)
\end{aligned}$$

Here, taking $f = 1$ results in a fully implicit scheme, whereas taking $f = 0.5$ corresponds to the Crank-Nicolson scheme (Crank and Nicolson, 1996). The equation is solved after every time step for liquid water flow. Then, for LWC θ , both θ^n , as 10 well as θ^{n+1} are known from solving Eq. 12. Furthermore, it is assumed that the water flux q is constant with time and can be referenced with the time level n . The liquid water flux is directly obtained from the Darcy-Buckingham law (Buckingham, 1907), which forms the basis of Richards equation:

$$q_{i+1}^n = \frac{K_{i+1/2}}{\rho_{i+1/2}} \left(\frac{\rho_{i+1} h_{i+1} - \rho_i h_i}{(\Delta z_{\text{up}})^2} \right) + \cos(\gamma) K_{i+1/2} + \cos(\gamma) \frac{K_{i+1/2}}{\rho_{i+1/2}} z_{i+1/2} \left(\frac{\rho_{i+1} - \rho_i}{\Delta z_{\text{up}}} \right), \quad (15)$$

and

$$15 \quad q_{i-1}^n = \frac{K_{i-1/2}}{\rho_{i-1/2}} \left(\frac{\rho_i h_i - \rho_{i-1} h_{i-1}}{(\Delta z_{\text{down}})^2} \right) + \cos(\gamma) K_{i-1/2} + \cos(\gamma) \frac{K_{i-1/2}}{\rho_{i-1/2}} z_{i-1/2} \left(\frac{\rho_i - \rho_{i-1}}{\Delta z_{\text{down}}} \right). \quad (16)$$

The domain in SNOWPACK is typically nonuniform and the spatial discretizations in Eq. 14 for a nonuniform grid are based on Veldman and Rinzema (1992). The system of equations described by Equation 14 forms a tri-diagonal matrix, similar to and solved in the same way as the equation for liquid water flow (Eq. 12).

SNOWPACK by default uses the Crank-Nicolson scheme. The fully implicit scheme is only first order accurate, whereas the 20 Crank-Nicolson scheme is second order accurate. Both schemes are unconditionally stable and suffer only minimal numerical diffusion for advection. As with many other common schemes, the advection part does not perfectly conserve sharp transitions. The Crank Nicolson scheme is, in spite of being unconditionally stable, prone to spurious oscillations in the solution. To choose adequate time steps, we apply the Courant-Friedrichs-Lowy (CFL) condition (Courant et al., 1928), typically required for stability of an explicit scheme, also for the Crank-Nicolson scheme:

$$25 \quad q \frac{\Delta t}{\Delta z} \leq 1 \quad (17)$$

Note that if the CFL condition is violated, the time step is reduced and the last time step for the Richards equation is also repeated with the reduced time step.

2.2.3 Boundary Conditions

The boundary conditions for the Richards equation (Eq. 3) are determined by a Neumann boundary condition at the top, consisting of the top water flux from rain, evaporation or condensation and a Dirichlet boundary condition at the bottom by prescribing the pressure head. The pressure head at the bottom of the sea ice corresponds to the water pressure at that depth, 5 which equals the sea level in the model domain (z_{sl} , m). This is determined from the isostatic balance:

$$z_{\text{sl}} = \frac{\text{SWE}}{(\rho_w + \beta S_o)}, \quad (18)$$

where S_o is the ocean water salinity (g kg^{-1}) and SWE is the snow water equivalent, defined as the sum over all elements N of the mass of each element j in the model:

$$\text{SWE} = \sum_{j=1}^N (\theta_{i,j} \rho_i + \theta_j \rho_j) \Delta z_j, \quad (19)$$

10 where $\theta_{i,j}$ and θ_j are the volumetric content ($\text{m}^3 \text{ m}^{-3}$) for layer j of ice and water, respectively. ρ_i is the density of freshwater ice (917 kg m^{-3}) and ρ_j the brine density of layer j (see Eq. 5).

The boundary conditions for the advection terms of the advection-diffusion equation (Eq. 13) are prescribed as a Neumann boundary condition, with fresh water at the top, and ocean salinity at the bottom. Only in case of an outgoing water flux at the top of the domain (evaporation), a zero-flux condition for salinity is used (i.e., salt will remain in the sea ice or snow with 15 evaporation).

For the diffusion terms in Eq. 13, we implemented a no-flux boundary condition at the top of the domain. This implies that there is no diffusion of salt with the atmosphere. This boundary condition is derived by considering the central differences scheme for the diffusion term on a nonuniform grid, determined according to:

$$\frac{\partial^2}{\partial z^2} (D\theta S_b) \approx \frac{\frac{\partial D\theta S_b}{\partial z} \Big|_{z_{i+1/2}} - \frac{\partial D\theta S_b}{\partial z} \Big|_{z_{i-1/2}}}{z_{i+1/2} - z_{i-1/2}} \approx \frac{\frac{D_{i+1}\theta_{i+1}S_{b,i+1} - D_i\theta_iS_{b,i}}{z_{\text{up}}} - \frac{D_i\theta_iS_{b,i} - D_{i-1}\theta_{i-1}S_{b,i-1}}{z_{\text{down}}}}{\frac{1}{2}(z_{\text{up}} + z_{\text{down}})} \quad (20)$$

20 In general, a no-flux boundary condition can be achieved by forcing gradients over the boundaries to be 0, such that either the left (upper boundary) or right (lower boundary) term in the numerator of Eq. 20 vanishes.

We only apply the no-flux boundary at the top. For the bottom boundary condition at $i = 0$, diffusion is calculated by assuming:

$$S_{b,i}^n = S_{b,i}^{n+1} = S_o. \quad (21)$$

25 2.2.4 Hydraulic Properties

For solving the Richards equation and the salinity transport equation, several parameters which depend on the snow and ice microstructure need to be specified. For saturated hydraulic conductivity (K_{sat}), we define elements with a porosity (i.e., $1 - \theta_i$) larger than 0.25 as snow, and smaller than 0.25 as ice.

For snow elements, a formulation based on Calonne et al. (2012) is typically used (see Wever et al. (2014)):

$$K_{\text{sat}} = \left(\frac{\rho g}{\mu} \right) \left[3.0 \left(\frac{r_{\text{es}}}{1000} \right)^2 \exp(-0.013\theta_i \rho_i) \right], \quad (22)$$

where r_{es} is the equivalent sphere radius (m). Note that Eq. 14 in Wever et al. (2014) erroneously shows a factor 0.75 (which corresponds to r_{es} being a grain diameter) instead of 3.0.

5 For sea ice, the saturated hydraulic conductivity (K_{sat}) is based on Golden et al. (2007):

$$K_{\text{sat}} = 3 \cdot 10^{-8} \left(\frac{\rho g}{\mu} \right) (1 - \theta_i)^3 \quad (23)$$

In unsaturated conditions, the van Genuchten-Mualem model (Mualem, 1976) is used to relate the hydraulic conductivity in saturated conditions (Eq. 22 and 23) to unsaturated conditions. For averaging the hydraulic conductivity between elements, we use the geometric mean (Wever et al., 2015), which is the preferred method (Haverkamp and Vauclin, 1979; Celia et al., 10 1990). Furthermore, in unsaturated conditions, the van Genuchten model is used for the water retention curve, which describes the relationship between capillary suction and LWC (van Genuchten, 1980). The coefficients in this parameterization of water retention in snow is based on the work by Yamaguchi et al. (2012). We extend this parameterization independent of porosity, by absence of any information of water retention in sea ice as a function of salinity and LWC. It has a relatively small impact, as the largest part of the sea ice is below sea level and the model typically simulates saturated conditions here.

15 3 Data and Simulation Setup

3.1 In-situ Buoys

We apply the sea ice version of SNOWPACK to snow and sea ice properties measured from two Snow Buoys (Nicolaus et al., 2017) and one Ice Mass-balance Buoy (IMB) in the Weddell Sea, Antarctica. Snow Buoys are autonomous ice tethered instruments, which measure snow surface changes/accumulation with four ultrasonic sensors at approximately 1.5 m above 20 the snow/ice interface (Nicolaus et al., in prep). We construct a time series by averaging the four ultrasonic sensors of each buoy, creating a time series of the surface elevation referenced to the initial snow/ice interface upon installation of the buoy. In addition to the surface elevation, the Snow Buoys measure barometric air pressure and air temperature.

Each IMB consists of a 4.8 m long thermistor chain, with a vertical sensor spacing of 0.02 m and provides sea ice temperature as well as interfaces from snow, sea ice, and sea water. The instruments are described by Jackson et al. (2013). It turned out to 25 be good practice to co-deploy Snow Buoys and thermistor chain IMBs in order to observe snow depth and sea ice properties at the same time. The full data set of all these Lagrangian observations is available from <http://www.meereisportal.de> (Grosfeld et al., 2015).

The two selected Snow Buoys (Snow Buoys 2014S12 (Nicolaus and Schwegmann, 2017) and 2016S31 (Arndt et al., 2017)) have long time series and cover different trajectories, as shown in Fig. 1. Unfortunately, IMB 2014T9 collocated with Snow 30 Buoy 2014S12 stopped transmitting data soon after deployment. IMB 2016T41, collocated with Snow Buoy 2016S31 measured

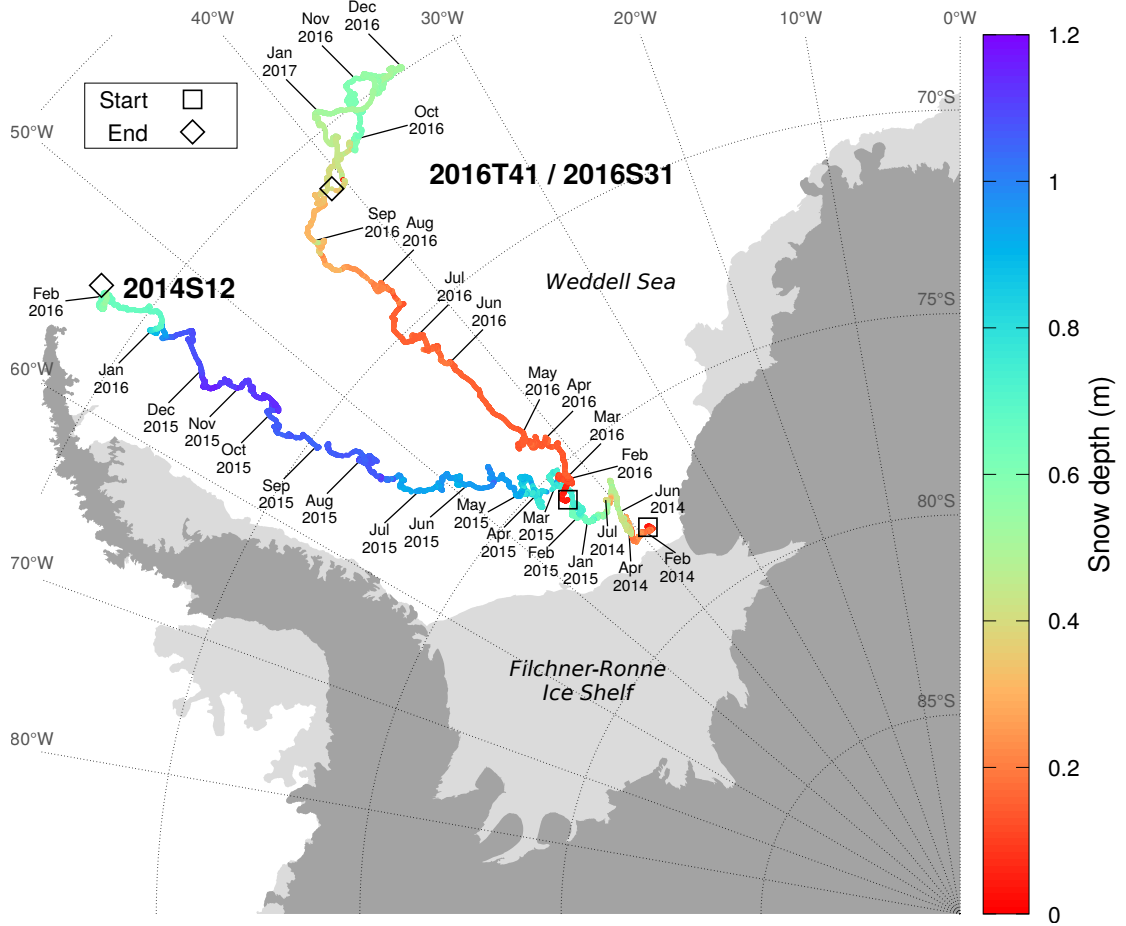


Figure 1. Trajectories of the two snow buoys used for the simulations. The average snow depth measured by the four snow depth sensors on each Snow Buoy is shown in color. Labels show the position of the respective Snow Buoy on the 1st day of the month. For buoy 2014S12, some labels at the beginning have been omitted for readability. The deployment location (start) is denoted by a square, the location of the last received data from the buoy (end) is denoted by a diamond. The collocated IMB buoy for the 2014S12 Snow Buoy (2014T9) stopped transmitting data shortly after installation and is ignored in the analysis. The collocated IMB buoy to Snow Buoy 2016S31 is 2016T41.

for almost the same period as the Snow Buoy. However, comparisons are limited to the sea ice temperature and ice thickness, excluding the snow cover on top, because the IMB was deployed directly onto the snow surface, without room to accommodate for snow accumulations after installation. Thus, the thermistor chain does not measure the snow cover properties, except for the lowest few cm.

Fig. 1 shows the trajectories with labels marking the location at the 1st of each month. Snow Buoy 2014S12 was deployed on 17 Jan 2014 and remained in the same area very close to the Filchner-Ronne Ice Shelf for the first year. From February 2015

onward, the Snow Buoy drifted northward parallel to the Antarctic Peninsula until data transmission was lost on 1 Feb 2016. During the last 18 hours no valid snow depth data were transmitted and the drift speeds were relatively high, suggesting that it is not a transmission or data logger failure, but rather an indication that flow deformation or breakup is the likely cause of the loss of the Snow Buoy. We consider this particular Snow Buoy due to its long time span, even though a collocated IMB data set is not available.

Snow Buoy 2016S31, collocated with IMB Buoy 2016T41, was deployed on 16 Jan 2016. This deployment first drifted on a predominantly northward course. Around the 1st of December, the northernmost position was reached and the deployment drifted southward again. The Snow Buoy transmitted data until 15 Jan 2017, 2:00 UTC, shortly before the last data transmission by the IMB Buoy (5 Feb 2017, 07:13 UTC). This combination of Snow Buoy and IMB Buoy is interesting for the long time span of collocated measurements.

3.2 Initial Conditions

To start each simulation, a description of the initial sea ice state is required. Upon installation of each Snow Buoy, the ice thickness, snow thickness and freeboard were determined. For simulations of these Snow Buoys, we distinguish three categories: (i) sea ice below sea level (ice thickness minus freeboard), (ii) sea ice above sea level (freeboard) and (iii) snow.

For the part of the sea ice below sea level, the volumetric ice content θ_i was fixed to 0.95, and the volumetric water content θ_w was subsequently calculated as:

$$\theta_w = (1 - \theta_i) \frac{\rho_i}{\rho_w} \quad (24)$$

This formulation leaves a small volumetric air content which can be filled when water refreezes and thereby expands. This is currently required for the stability of the numerical schemes in the SNOWPACK model, but in reality refreezing water would increase the pressure in the brine. The element temperature was initialized by the value recorded by the IMB upon installation. As it takes time for the thermistor chain to freeze into the ice and adapt to the surrounding ice temperature, this temperature is mostly representative of the ocean water. The brine salinity was set as the salinity for which the melting point corresponds to the measured temperatures.

For the part of sea ice above sea level, the volumetric ice content θ_i was also fixed to 0.95, but the remaining space was assigned to air content and the bulk salinity was set to 0 g kg⁻¹. In field studies, it was found that brine may exist above sea level, due to capillary wicking, or brine content is retained because of low conductivity in the brine channels (e.g., Cox and Weeks, 1974; Massom et al., 2001).

The initial snow layer was 10 cm for Snow Buoy 2014S12 and 2 cm for 2016S31. The snow cover was initialized with a density of 275 kg m⁻³, and a grain size of 0.15 mm. The grain shape was initialized as depth hoar with a sphericity and dendricity of 0. As the majority of the snowpack builds during the model simulations, the simulations are rather insensitive to the choice of initial snowpack properties. The element temperature was derived from the thermistor chain measurements. Finally, the depth of each element was set to 0.02 m.

3.3 Forcing Data

Simulations with the SNOWPACK model require air temperature, relative humidity, incoming shortwave radiation, incoming longwave radiation, wind speed and precipitation. Here, we used ERA5 (European Centre for Medium-range Weather Forecasts ECMWF Reanalysis 5) data to provide these parameters to drive the simulations. For each timestep and location, the simulated weather at the closest grid point in the ERA5 model was taken.

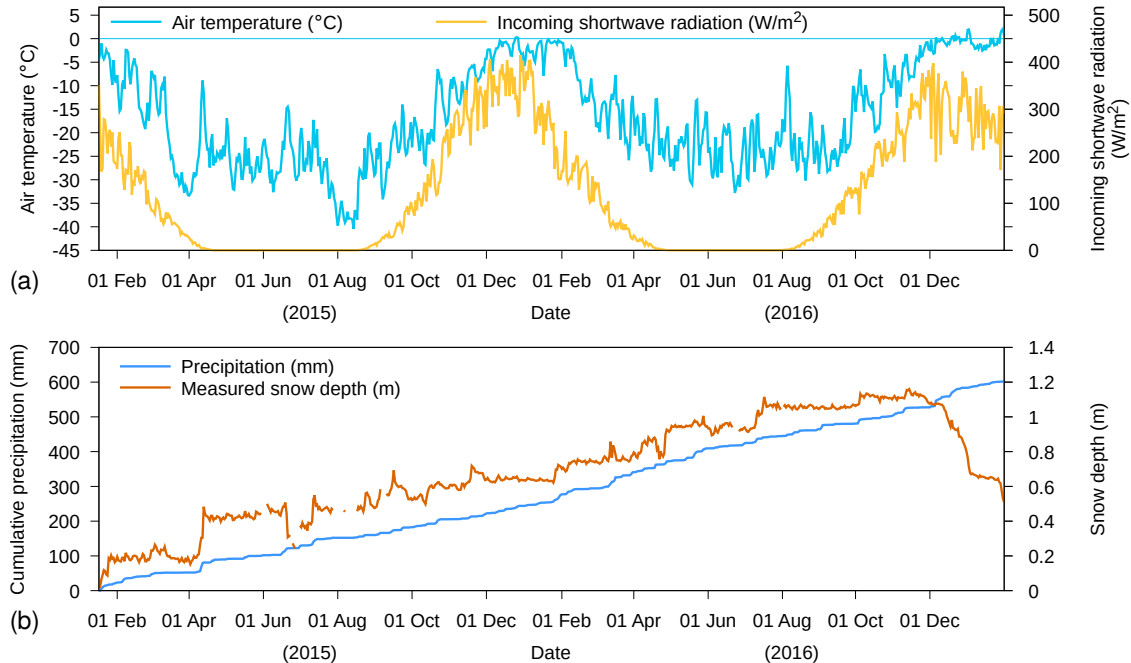


Figure 2. Meteorological forcing data from ERA5 for Snow Buoy 2014S12 for (a) daily average air temperature and daily average incoming shortwave radiation, and (b) cumulative precipitation. In (b), also measured snow depth by the buoy is shown.

Fig. 2 shows the daily average air temperature, incoming shortwave radiation and cumulative precipitation from the ERA5 forcing for Snow Buoy 2014S12. Additionally, the measured snow depth by the buoy is shown. We find that the daily average air temperature was mostly below 0°C, reaching -40°C in 2015. Near the end of the time series, when the Snow Buoy stopped transmitting data, daily average air temperature varied around 0°C. It can be expected that positive temperatures 10 during midday is associated with enhanced snow melt, which is indicated by the rapid decrease of measured snow depth starting from December 2016 onward. During austral winter 2015 and 2016, the Snow Buoy was located below the polar circle and consequently, there was no incoming shortwave radiation. In austral summer 2016/2017, the Snow Buoy drifted above the polar circle. Nevertheless, the average incoming shortwave radiation in the first austral summer is similar to the second austral summer. The cumulative precipitation from ERA5 reached around 600 mm for the almost two years that the buoy 15 was operative. The buoy recorded 1.2 m of snow accumulation. A marked increase in snow depth around April 1, 2015 is

accompanied by only a relatively small precipitation event. Except for this event, both the snow depth as well as the cumulative precipitation show a gradual increase over the two years until the melt phase starts.

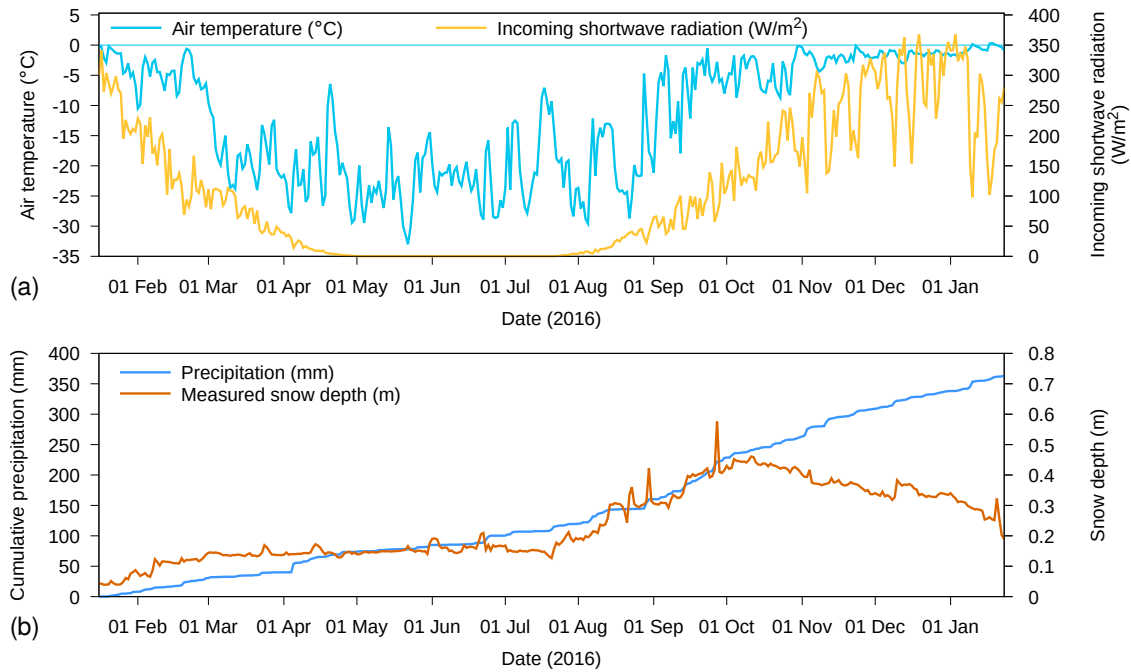


Figure 3. Meteorological forcing data from ERA5 for Snow Buoy 2016S31 for (a) daily average air temperature and daily average incoming shortwave radiation, and (b) cumulative precipitation. In (b), also measured snow depth by the buoy is shown.

Fig. 3 shows the daily average air temperature, incoming shortwave radiation and cumulative precipitation from the ERA5 forcing for Snow Buoy 2016S31. The yearly cycle in air temperature is similar to the year 2016 for Snow Buoy 2014S12, 5 with daily air temperatures reaching around -30°C in austral winter. In austral summer, air temperatures around 0°C suggest melting conditions, particularly from November 2016 to January 2017. This is reflected by the decrease in snow depth for this period. The Snow Buoy was also located south of the polar circle, resulting in the absence of shortwave radiation during austral winter. The precipitation sum for the year that the Snow Buoy was operative amounted to 350 mm. The snow depth does not change between March and July 2016, and shows an increase between August and October, after which a decrease occurs. The 10 cumulative precipitation show a similar pattern, with low precipitation between March and July, followed by a steady increase afterwards. Only during the melt phase, the increase in cumulative precipitation is not reflected by an increase in snow depth.

SNOWPACK has the possibility to either use a precipitation time series as input to determine when snow fall occurs, or to use a time series of snow depth to interpret increases in measured snow depth as snow fall events when simulated snow depth is less than the measured snow depth (Lehning et al., 1999). Note that there is no downward correction when the measured 15 snow depth is below the simulated snow depth (in case of melt, surface sublimation, snow erosion, etc.). In order to use the snow depth driven method for the Snow Buoys and base the mass balance on Snow Buoy data, a layer can be marked in the

simulations and tracked throughout the snow – sea ice continuum. By marking the layer that corresponds to the reference level for the snow depth measurements, the measured snow depth can be tracked relative to this marked layer. The output routines of the model have been adapted accordingly to reference the output to either the sea level, or to the marked reference layer.

The ocean heat flux determines the ice mass balance at the bottom of the ice. Its value can be highly variable and dependent 5 on ocean conditions below the sea ice (Ackley et al., 2015). From that study, we use a value of 8 W m^{-2} , unless otherwise noted.

4 Results

4.1 Example Simulation

Fig. 4 shows an example of model behaviour when an initially dry and fresh ice layer with a thickness of 1.58 m, consisting 10 of 94% ice and 6% air expressed as volumetric content, is positioned in ocean water with a salinity of 35 g kg^{-1} . The positive pressure head at the bottom of the sea ice corresponds with the pressure exerted by the displaced water. As a consequence, saline water enters the ice matrix (Fig. 4a,c), until it is in equilibrium with the sea level. The initial rate follows the saturated hydraulic conductivity for sea ice with a pore space of 6%, which is $3.55 \times 10^{-5} \text{ m s}^{-1}$ (Eq. 23).

As the pressure difference of the liquid water inside the ice matrix and the surrounding ocean water is decreasing, the salt 15 influx rate decreases over time (Fig. 4e). The brine salinity corresponds to the brine salinity of ocean water (35 g kg^{-1} , see Fig. 4d), corresponding to a bulk salinity of 1.65 g kg^{-1} (see Fig. 4c). The added mass to the sea ice (Fig. 4b) causes the ice to sink deeper inside the ocean water, decreasing the freeboard (Fig. 4f).

This example illustrates that the Crank-Nicolson scheme does not preserve the sharp transition in salinity, as both the bulk 20 (Fig. 4c) as well as the brine (Fig. 4d) salinity shows smoothing behaviour at the saline water front. This reduces the pore space by refreezing to adapt to the thermal conductivity, reducing the saturated hydraulic conductivity in the wetting front region.

4.2 Temperature Validation

Fig. 5a and 5b show the simulated temperature of the snow–sea ice system for simulations driven by in-situ measured snow 25 depth and ERA5 precipitation, respectively. Dashed lines denote the reference level, i.e., the snow–sea ice interface as determined upon installation of the Snow Buoy. The sea level as calculated from hydrostatic balance is indicated by the solid line. For the snow depth driven simulations, the sea level stays below the snow–sea ice interface, indicating that freeboard is positive during the whole simulation period. However, for the precipitation driven simulations, there is more snowfall, which causes negative freeboard from October onward.

Fig. 5c shows the measured sea ice temperatures from the corresponding IMB. Note that for this IMB, the thermistor chain 30 does not extend above the initial 2 cm snow layer on top of the sea ice, such that the time evolution of the snow cover is not recorded by the IMB. We find that the IMB confirms the strong cooling of the sea ice during the austral winter months, as found

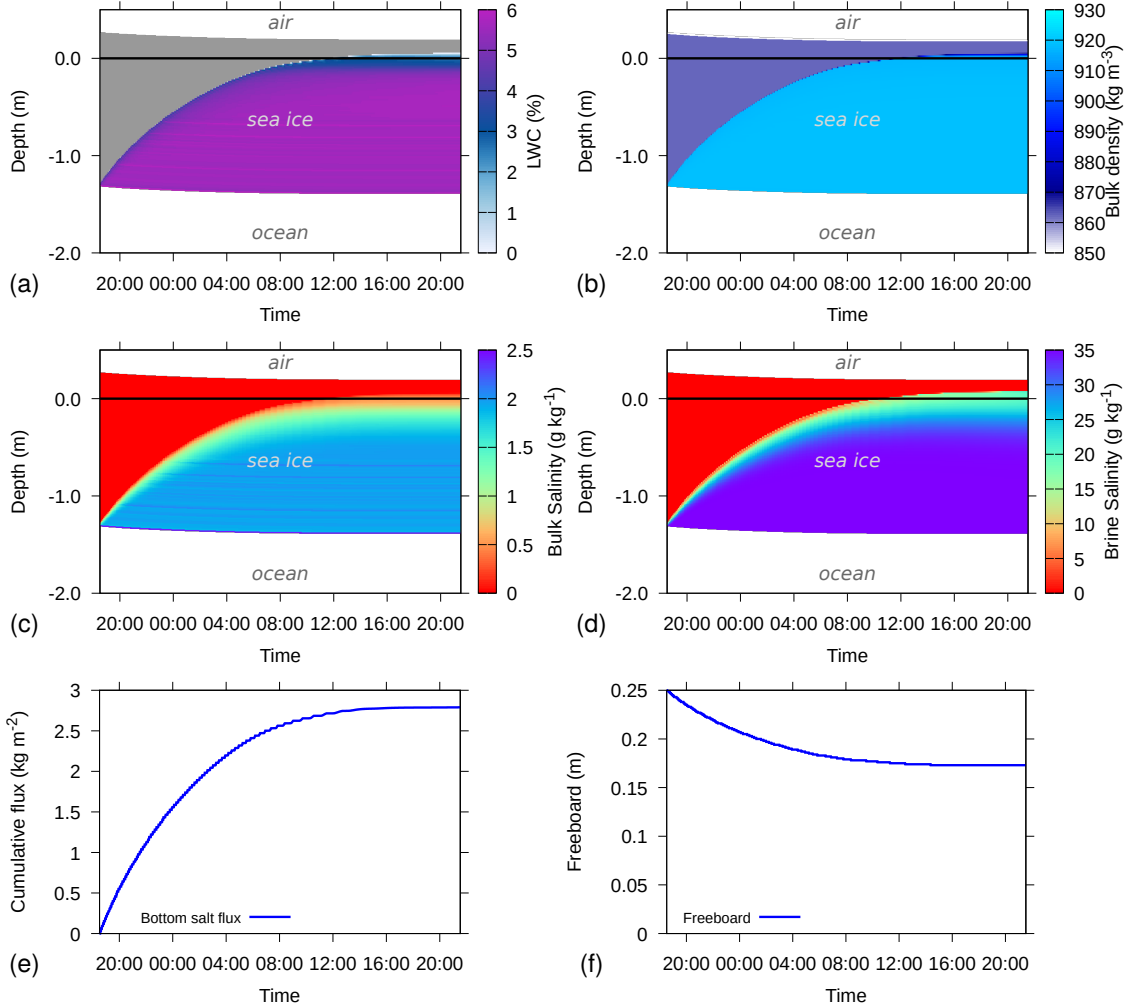


Figure 4. Example simulation where initially dry, porous freshwater ice with 94% volumetric ice content is placed into ocean water with a salinity of 35 g kg^{-1} . Shown are (a) liquid water content (LWC), (b) bulk density, (c) bulk salinity, (d) brine salinity, (e) cumulative salt flux at the bottom of the sea ice and (f) freeboard. In (a), dry parts of the ice are colored grey. In (a), (b), (c), and (d), the depth on the y-axis is relative to sea level, i.e., sea level is 0 and indicated by the solid black line.

in the simulations, as well as the near-surface warming to the melting point of fresh water shortly before the last transmission by the buoy.

Fig 6 shows difference plots of measured ice temperatures and simulated ice temperatures. Fig 6a compares the snow depth driven simulations (i.e., Fig 5a minus Fig. 5c) and Fig 6b compares the precipitation driven simulations (i.e., Fig 5b minus Fig. 5c). Positive values denote an overestimated temperature by the model and vice versa. Note that the bottom of the sea ice in the simulations is typically above the ice–ocean interface in the IMB data.

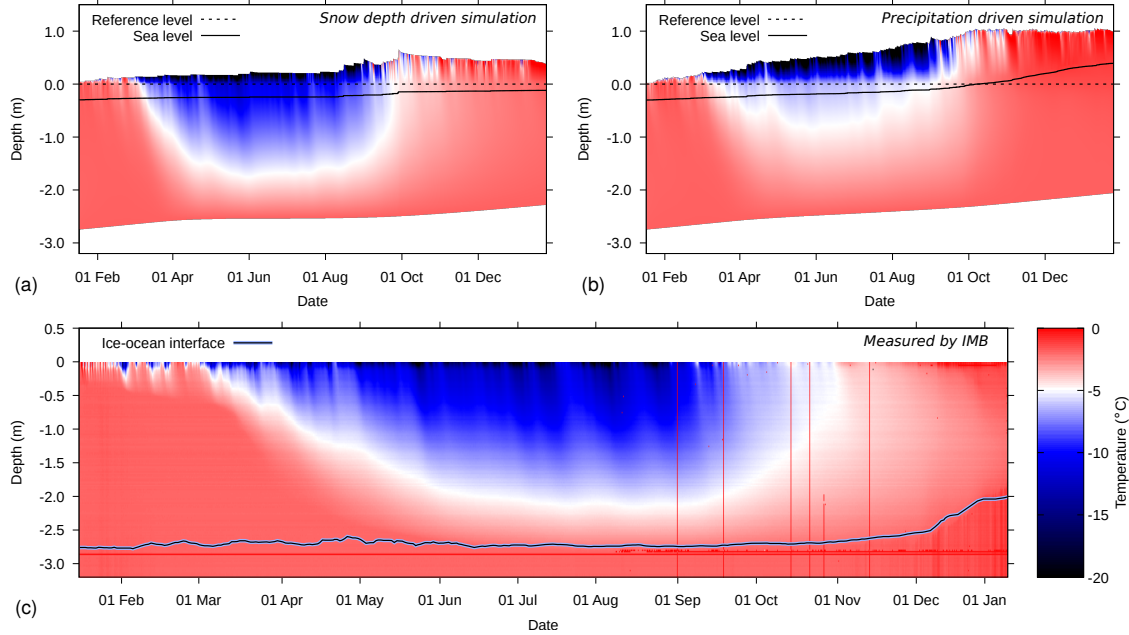


Figure 5. Snow and ice temperatures for Snow Buoy 2016S31 / IMB 2016T41, for (a) simulations driven by in-situ measured snow depth, (b) simulations driven by ERA5 precipitation, and (c) measured temperatures by the IMB. The depth on the y-axis is defined relative to the sea ice-snow interface, as determined upon installation (dashed line). In (a) and (b), the solid line denotes the sea level as determined by the simulations. In (c), the blue/black line denotes the ocean/sea ice interface, as determined for the IMB.

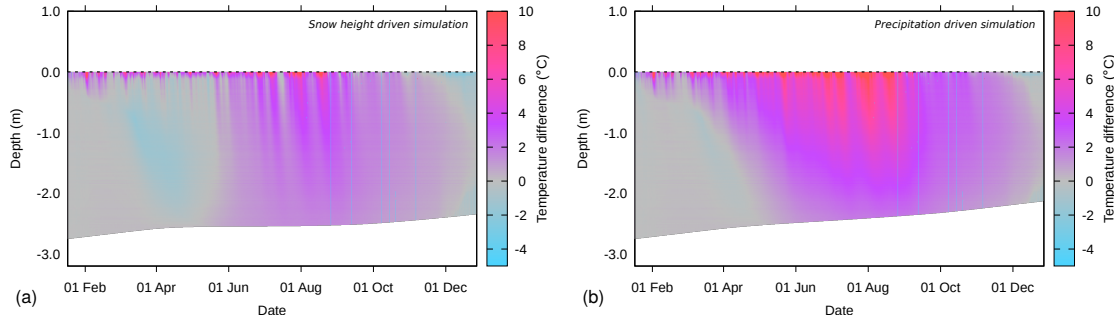


Figure 6. Difference between simulated and measured snow and ice temperatures for Snow Buoy 2016S31 / IMB 2016T41, for (a) simulations driven by in-situ measured snow depth, (b) simulations driven by ERA5 precipitation. The depth on the y-axis is defined relative to the sea ice-snow interface, as determined upon installation.

The comparison shows that in the period March to May, the snow depth driven simulation slightly underestimates the sea ice temperatures, which suggests an overestimation of the initial cooling of the sea ice towards austral winter. Both simulations underestimate the lowest temperatures reached in winter by up to 6-15°C near the snow-sea ice interface, which is located

at the top of the thermistor chain. Similarly, incidental cooling in near surface sea ice layers in February and March are also underestimated. This could on the one hand indicate an overestimation of incoming energy or an underestimation of outgoing energy in the forcing data or by the model. On the other hand, an underestimated (new) snow density would result in an underestimated thermal conductivity and overestimated thermal insulation in the model, as thermal conductivity typically increases with increasing snow density. Heat from the sea ice part would then not be able to be effectively transported through the snowpack and exchanged with the atmosphere.

The simulations driven by ERA5 precipitation show about twice as much snow accumulating on the sea ice (Fig. 5b) compared to accumulations determined from the snow height measurements (Fig. 5a). Also the reanalysis provides precipitation (and thus snow accumulating) in the austral winter time, which is not found in the snow depth time series. This is not necessarily a bias in ERA5, because snow erosion by wind can keep the snow depth constant over extended periods of time. Due to this discrepancy, the total snow depth may be overestimated by the ERA5 input at the end of the simulation. Furthermore, the thick snow cover in the precipitation driven simulation better insulates the underlying ice, resulting in a stronger overestimation of ice temperatures compared to the snow height driven simulation.

The thermistor chain is also used to determine the heat capacity by heating the chain for 1 or 2 minutes and analyzing the temperature response. By combining the absolute temperatures and the heating rates, the ice–ocean interface has been manually determined and is shown in Fig. 5c. The IMB data confirm the modelling result that the strong negative energy balance at the top of the snow–sea ice system during austral winter has not resulted in an ice thickness increase. The warmer sea ice in the precipitation driven simulations resulted in a thinning of the ice by the ocean heat flux, which is not confirmed by the IMB data. The decrease in ice thickness in December 2016 is not reproduced by either one of the simulation setups. The trajectory of the buoy shows a marked change in drift direction (Fig. 1), changing from a northward to a southward drifting course during this period. This change of direction may have been accompanied by an intrusion of warm ocean water below the sea ice and an increased ocean heat flux.

LWC, bulk and brine salinity, as well as the bottom salt flux for the simulations driven by measured snow depth are shown in Fig. 7. LWC (Fig. 7a) shows a strong reduction in austral winter due to the freezing brine, causing brine salinity to increase (Fig. 7c). The snow is dry most of the time, except towards the end of the simulation when meltwater percolates downward.

Furthermore, we find a thin layer with low values of LWC just above sea level. This is caused by capillary forces causing upward motion of sea water above sea level.

Fig. 7b shows that the bulk salinity of the sea ice hardly changes over the course of the simulation, whereas the brine salinity (Fig. 7c) clearly shows a relationship with the temperature. This reflects the prescribed thermal equilibrium between brine and the ice, assuming that the brine is at melting temperature. Fig. 7d shows that the added weight of the accumulating snow pushes the sea ice deeper into the ocean, increasing the pressure head at the bottom of the sea ice. This leads to an influx of saline water, even though the sea level remains below the snow–ice interface. Combined with rising temperatures, a layer with increased bulk salinity and increased LWC forms around and just below sea level around the 1st of October.

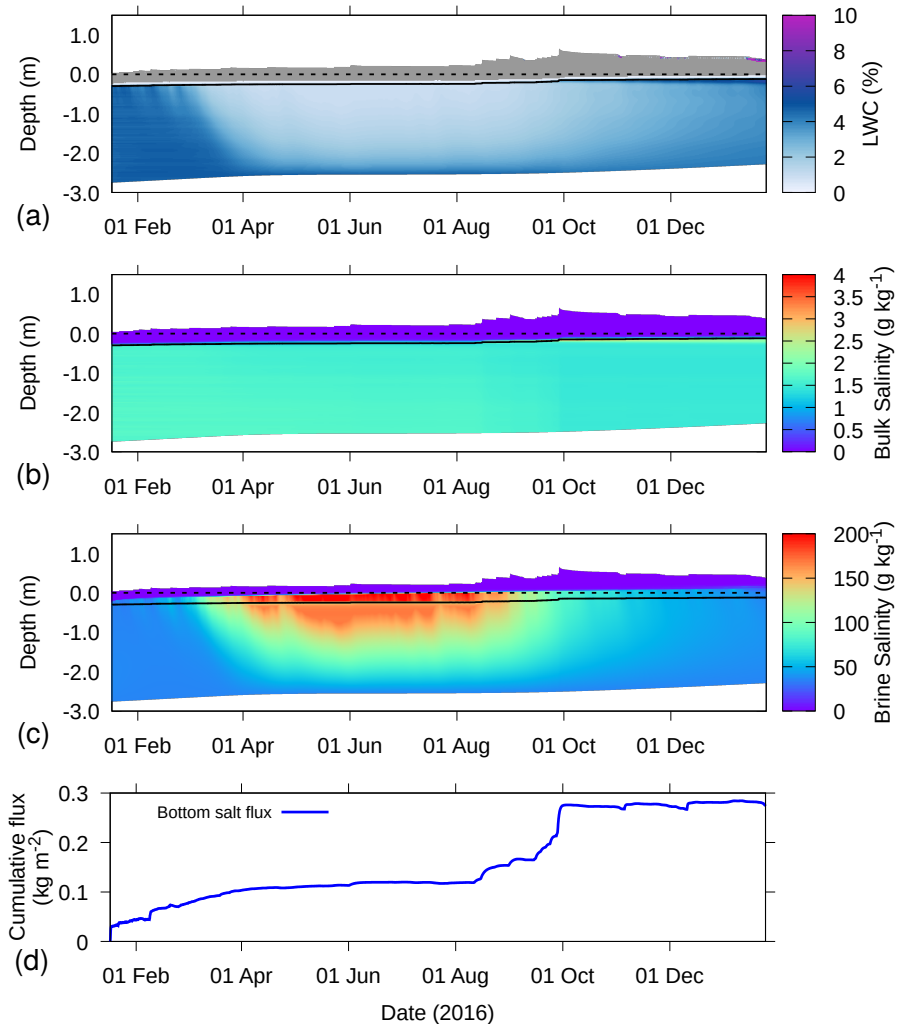


Figure 7. Example simulation for Snow Buoy 2016S31, where measured snow depth was used to derive the precipitation events, for (a) LWC, (b) bulk salinity, (c) brine salinity and (d) cumulative salt flux at the bottom of the sea ice. In (a), dry parts of the snow – sea ice system are colored grey. In (a), (b), and (c), the depth is defined relative to the sea ice-snow interface, as determined upon installation (dashed line). The solid line denotes the sea level as determined by the simulation. In (d), an increasing cumulative flux denotes inflow and vice versa.

4.3 Flooding and Superimposed Ice Formation

Figs. 8 and 9 show an example simulation for Snow Buoy 2014S12. The simulations were driven by the snow depth measurements from the buoy. Upon installation of the buoy, the snow depth was referenced to the sea ice surface. This reference level is shown by the dashed line. Due to basal ice melt and growth, as well as additional snowfall, the simulated sea level became 5 higher w.r.t. to the snow depth sensor, as indicated by the solid line. This is congruent with a negative freeboard. It indicates that significant flooding occurred, as also evidenced by the LWC in Fig. 8b and associated high bulk salinity (Fig. 8c). Fig. 9a shows that the bulk density of the flooded part is similar to the underlying ice density, illustrating the depletion of pore space. Fig. 9b shows that much of the sea water flooding the snow refroze, adding substantial ice mass.

The simulated temperature (Fig. 8a) shows the two austral winters with low temperatures, and the two austral summers 10 with temperatures close to 0°C . Interestingly, the low temperatures in the first austral winter impacted the part below sea level stronger than the second austral winter, as demonstrated by the lower temperatures in that part of the domain. During the second austral winter, the flooding in the simulation increased the liquid water content of the snow and consequently, much of the energy loss by the sea ice in this period was balanced by the energy release from refreezing liquid water, rather than decreasing temperatures.

15 Fig. 8e shows that flooding also leads to a strong influx of salt to the snow-sea ice system. The flooding saturates the snow, which has significant pore space compared to the sea ice. Therefore, snowfall events of similar magnitude have different effects on the salt influx, depending on whether or not flooding occurs at the time.

Note that the flooding, as depicted in simulations with the Richards equation coupled to the transport equation, is governed by the hydraulic conductivity of ice. In cold ice, hydraulic conductivity can be so low that negative freeboard remains for extended 20 period of times, even without flooding. On the other hand, flooding may also be triggered by deformation and cracking of the sea ice, combined with lateral flow effects. However, Maksym and Jeffries (2000) have shown that the simpler assumption (i.e., negative freeboard will trigger flooding) can already yield satisfying results. In the model, the maximum ice contents is fixed to $0.99 \text{ m}^3 \text{ m}^{-3}$ and is typically lower, such that hydraulic conductivity is generally large enough for instantaneous flooding.

The brine salinity in Fig. 8d shows spurious oscillations. These originate from the lower boundary and could be caused by 25 the strong transition of brine salinity to ocean salinity. Also, the oscillations are partly attributed to the maximum allowed ice contents of 99% in the simulations, as they occur in the same area. The exact numerical mechanism and a possible solution is unknown at the stage.

Figs. 9c and 9d show the snow microstructure as simulated by the model. Even though validation for this specific floe is not possible, we find several features consistent with other field observations. For example, a wet slush layer (coloured red) at the 30 interface between snow and ice is visible, triggered by capillary suction and flooding. This is also reported in Nicolaus et al. (2009) and Arndt and Paul (2018) for the same geographical region. Even though those field observations report the presence of depth hoar layers in snowpacks, particularly in deeper snowpacks (exceeding 30 cm), the simulations seem to show more deep depth hoar layers (coloured blue). The field observations often report wind slabs or other hard layers in between depth hoar layers. Simulating those kind of layers is a well-known problem for snowpack models (Domine et al., 2019).

The grain size shown in 9d ranges from 2-2.5 cm in the depth hoar layers at the base of the snowpack to 0.5-1 cm near the top of the snowpack. These simulated grain sizes corresponds to the range of values reported by the field studies listed earlier (1-5 mm), yet exact validation remains difficult.

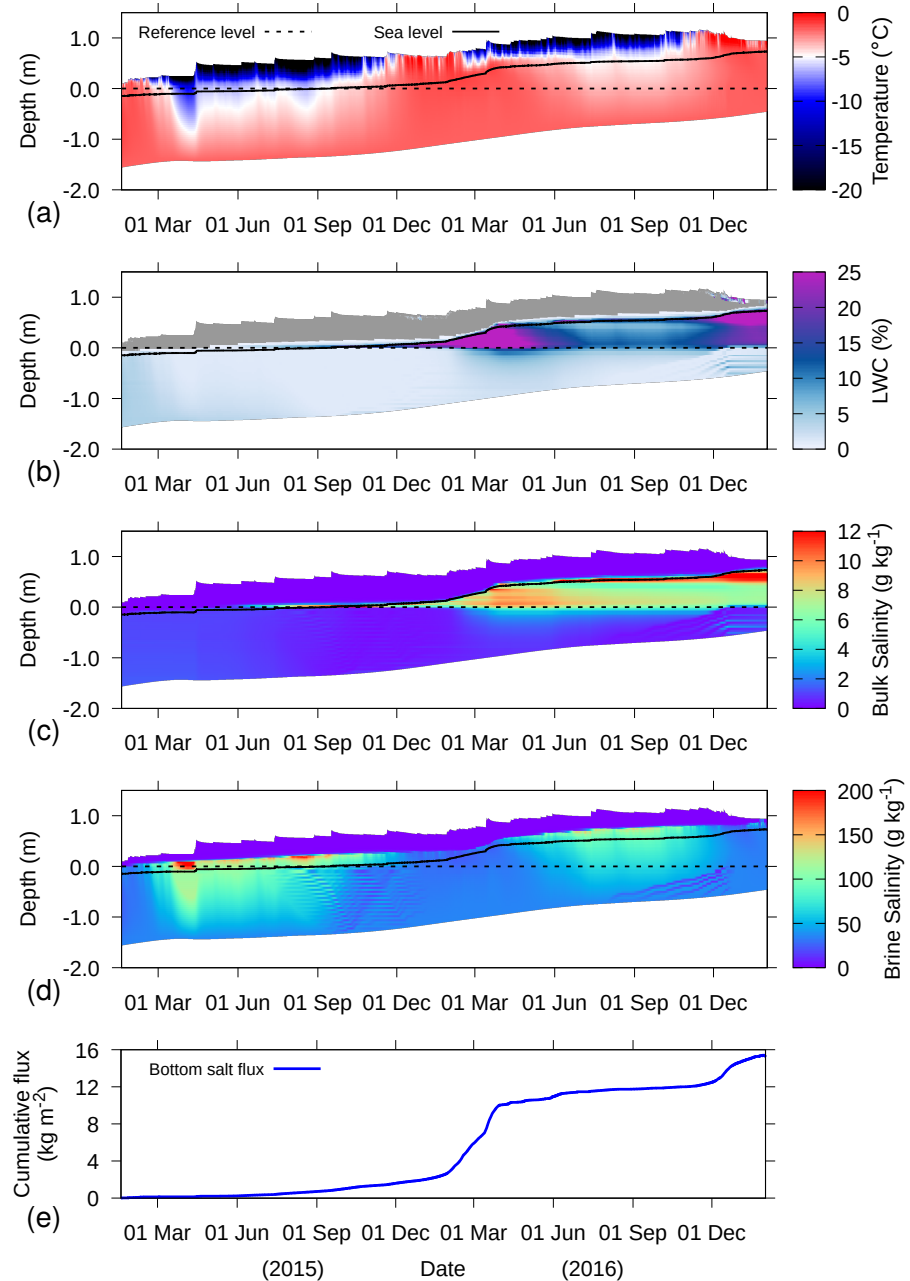


Figure 8. Example simulation for buoy 2014S12, where measured snow depth was used to derive the precipitation events, for (a) temperature, (b) LWC, (c) bulk salinity, (d) brine salinity and (e) cumulative salt flux at the bottom of the sea ice. In (b), dry parts of the snow – sea ice system are colored grey. In (a), (b), (c), and (d), the depth is defined relative to the sea ice-snow interface, as determined upon installation (dashed line). The solid line denotes the sea level as determined by the simulation. In (e), an increasing cumulative flux denotes inflow and vice versa.

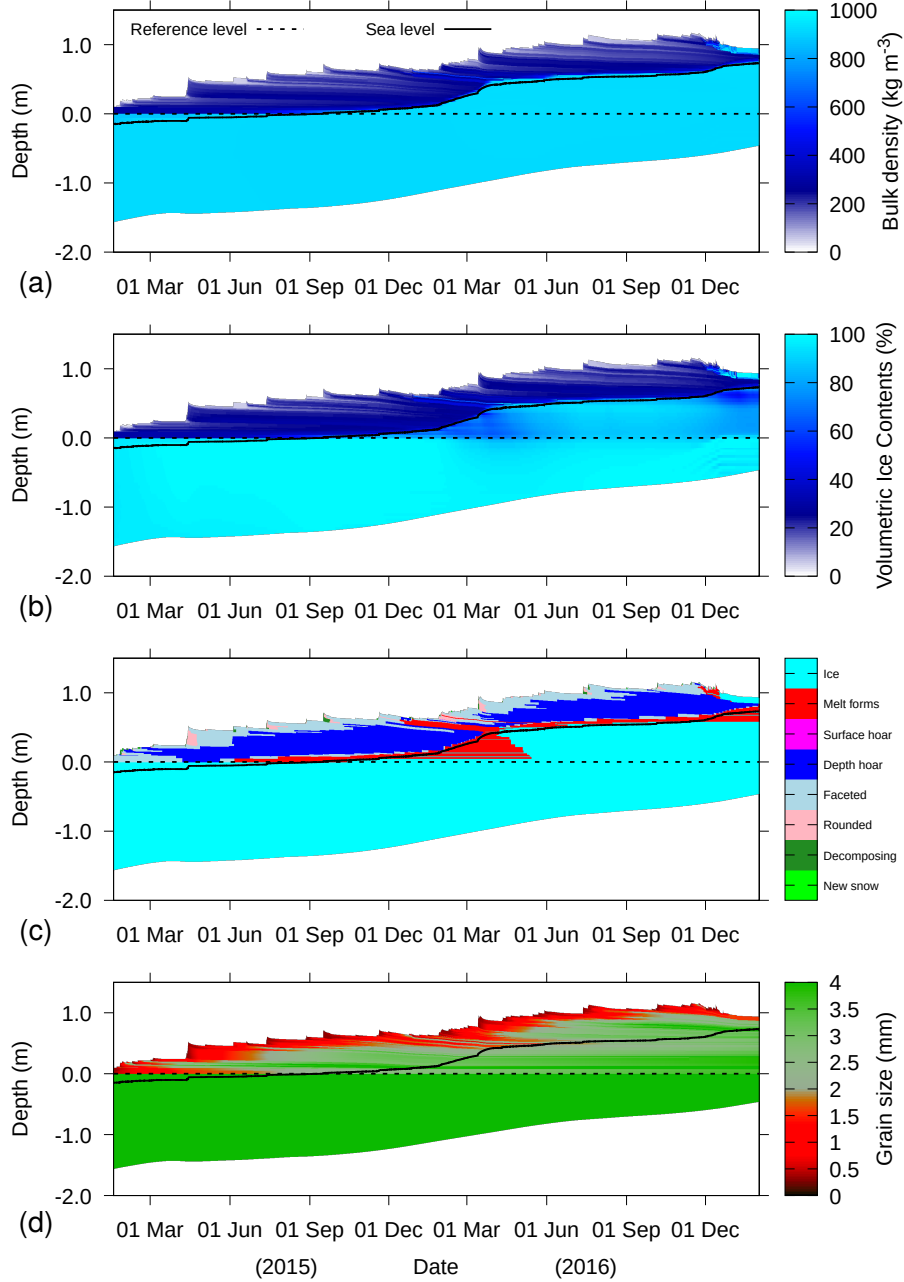


Figure 9. Example simulation for buoy 2014S12, where measured snow depth was used to derive the precipitation events, for (a) total bulk density, (b) volumetric ice content, (c) grain type and (d) grain size. The depth on the y-axis is defined relative to the sea ice-snow interface, as determined upon installation (dashed line). The solid line denotes the sea level as determined by the simulation.

4.4 Forced Warming and Cooling

Warming conditions increase the brine volume and the hydraulic conductivity of the sea ice, but also can cause freshwater percolation from snow melt. Similarly, cooling conditions decrease brine volume and increase brine salinity and density. When brine channels allow, the dense brine may drain from the sea ice.

5 To test how our model simulations would react to continuous warming or cooling conditions, we used Snow Buoy 2016S31 for two experiments where we forced constant warming and constant cooling conditions by modifying the meteorological driving data starting April 1, 2016. To force warming conditions, we prescribed a constant air temperature of $+5^{\circ}\text{C}$, a relative humidity of 80%, a wind speed of 3 m s^{-1} and an incoming shortwave radiation of 300 W m^{-2} .

Fig. 10 and 11 show the simulation result for the warming experiment with buoy 2016S31. Fig. 10 shows that as soon as 10 melting conditions were enforced (starting April 1st), the snowpack very quickly reached melting temperature. The fresh water percolating as a result from snow melt first started accumulating on below-freezing sea ice with low porosity (see Fig. 10b). This process is visible in April and leads to a thin layer of superimposed ice (Fig. 11b and 11c). Starting April 15, the bulk density of the snow – sea ice system was homogeneously around ice density, showing that the pore space has been depleted (11a).

15 The fresh water started flushing the ice around April 10, leading to a rapid reduction of bulk and brine salinity (Fig. 10c,d), due to the outflow of saline water at the bottom of the sea ice (Fig. 10e). When the brine decreases, water freezes and the permeability of the sea ice is low compared to the surface melt. We find that the meltwater accumulates on the top of the sea ice (Fig. 10b), which can be interpreted as the formation of a melt pond.

The sea ice thins continuously upon continued warming (Fig. 11b), until the ice has melted and the melt pond disappears. 20 At this point, the simulations showed strong instabilities in the bottom salt flux, such that the cumulative flux in Fig. 10e is only shown for the time period with ice below the liquid water. Note that the melt pond in the model consists of a little bit of ice (Fig. 11b), which results from the SNOWPACK numerics.

Fig. 12 shows an example where cooling conditions were enforced. Similar to the warming example, the meteorological forcing conditions were replaced from April 1 onward by setting a constant air temperature of -30°C , a wind speed of 1 m s^{-1} 25 and no incoming shortwave radiation. The ocean heat flux was set at 8 W m^{-2} . As soon as cooling conditions were present, a freezing front progressed through the sea ice. The interface between the sea ice and the ocean remained at the freezing point of ocean water, while the sea ice freezed and increased thickness.

With the decrease in temperature, brine salinity increased (Fig. 12d). This is achieved by freezing the liquid water, as shown by the decrease in LWC (Fig. 12b).

30 An increase in brine salinity also increases the density of the brine. This may lead to flushing of the sea ice, when the heavy brine moves downward and is replaced by lighter ocean water. However, in our simulations, there is only a very small outflow of salinity at the bottom (Fig. 12e) and the bulk salinity remains approximately constant (Fig. 12c). This result shows that without a description of the convective processes in sea ice resulting from cooling (Griewank and Notz, 2013), the salinity depletion found due to cooling is strongly underestimated by this model approach.

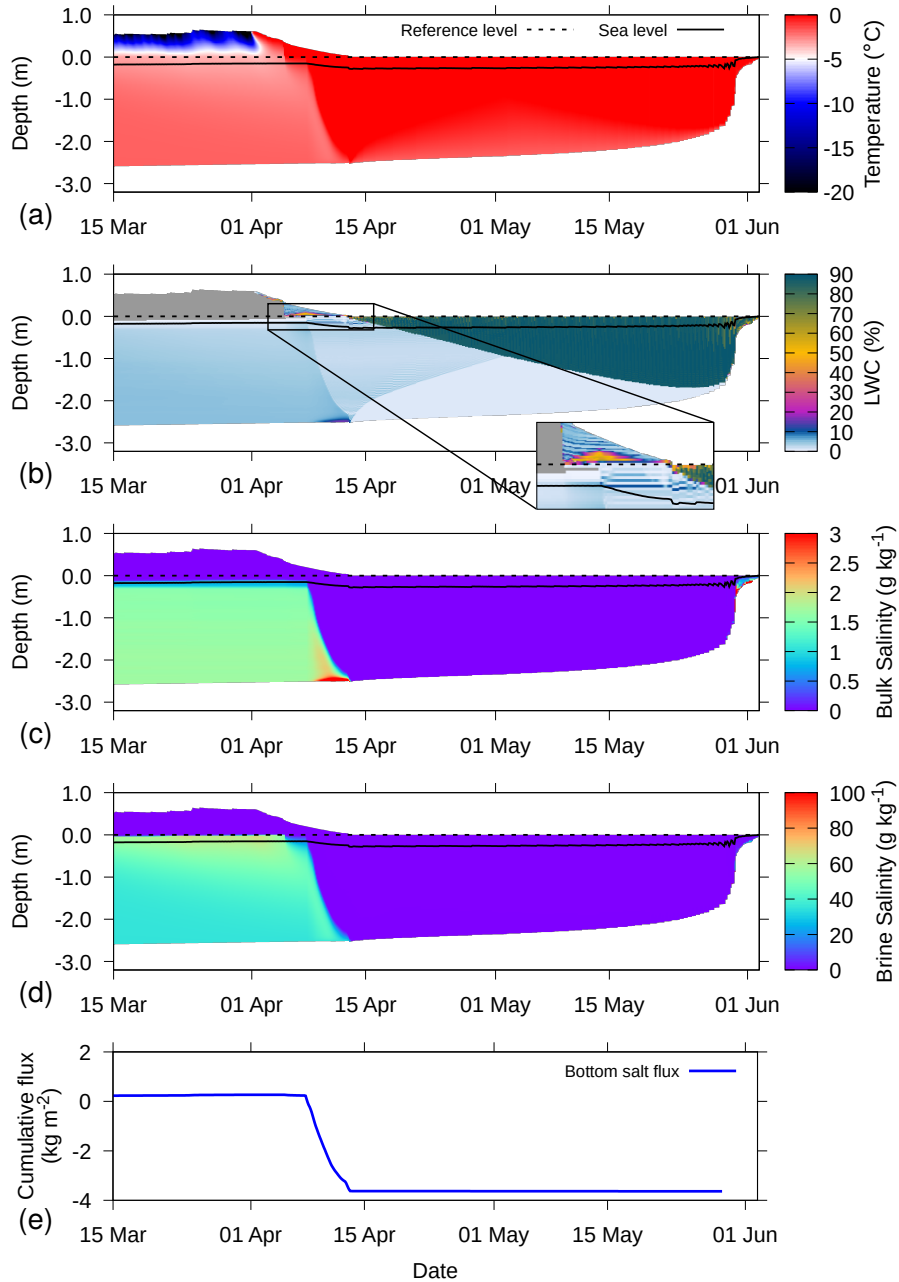


Figure 10. Simulation for 2016S31, where from April 1 onward, melting conditions were enforced, for (a) temperature, (b) LWC, (c) bulk salinity, (d) brine salinity and (e) cumulative salt flux at the bottom of the sea ice. In (b), dry parts of the snow – sea ice system are colored grey. In (a), (b), (c), and (d), the depth on the y-axis is defined relative to the sea ice-snow interface, as determined upon installation (dashed line). The solid line denotes the sea level as determined by the simulations. An increasing cumulative flux denotes inflow and vice versa.

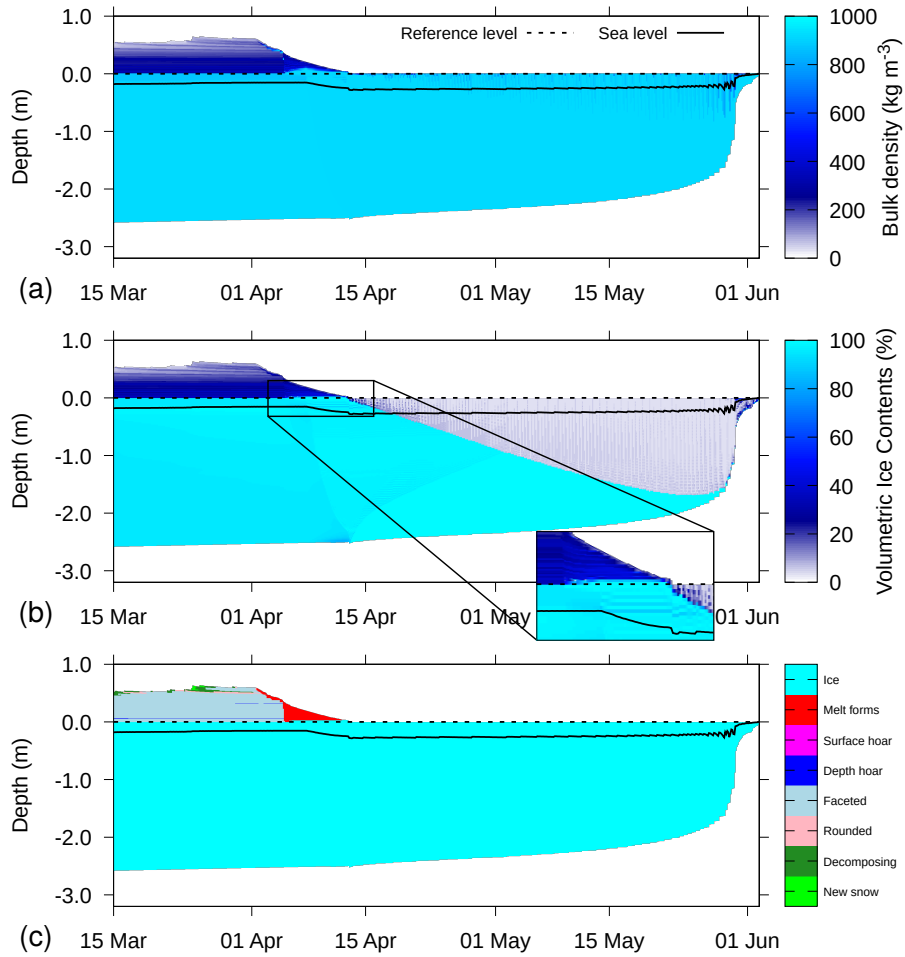


Figure 11. Simulation for 2016S31, where from April 1 onward, melting conditions were enforced, for (a) total bulk density, (b) volumetric ice content, and (c) grain type. The depth on the y-axis is defined relative to the sea ice-snow interface, as determined upon installation (dashed line). The solid line denotes the sea level as determined by the simulations.

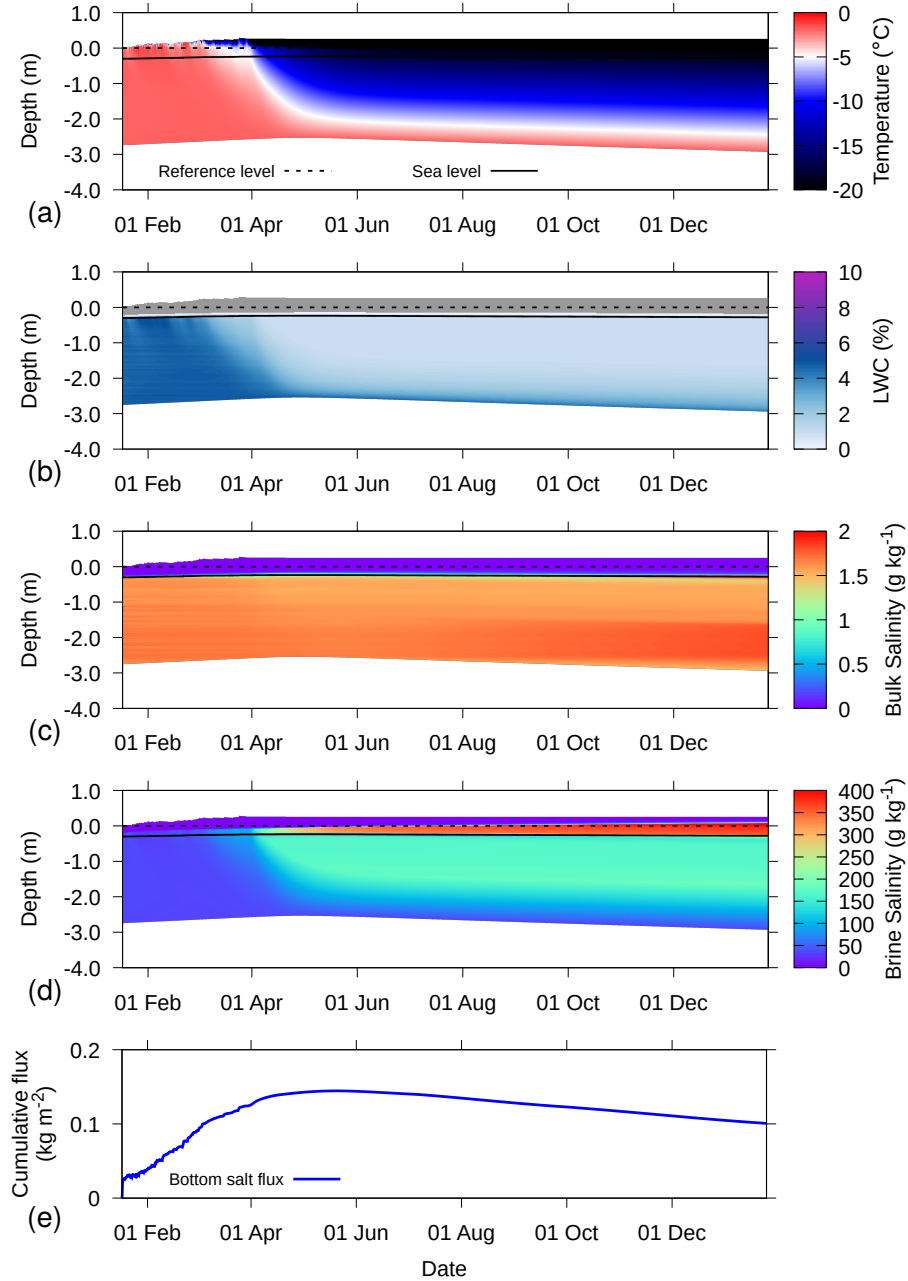


Figure 12. Simulation for 2016S31, where from April 1 onward, cooling conditions are enforced, for (a) temperature, (b) LWC, (c) bulk salinity, (d) brine salinity and (e) cumulative salt flux at the bottom of the sea ice. In (b), dry parts of the snow – sea ice system are colored grey. In (a), (b), (c), and (d), the depth on the y-axis is defined relative to the sea ice-snow interface, as determined upon installation (dashed line). The solid line denotes the sea level as determined by the simulations. An increasing cumulative flux denotes inflow and vice versa.

4.5 Thin Ice

A final test is run by starting with only 2 cm of ice, with constant atmospheric conditions to simulate thin ice evolution. The atmospheric conditions were set as $-10\text{ }^{\circ}\text{C}$ air temperature, 100% relative humidity, no wind speed, no incoming solar radiation and a constant incoming longwave radiation of 230 W m^{-2} . The ocean heat flux was set to 0 W m^{-2} .

5 The simulations were run for 1 month, which resulted in approximately 50 cm ice growth (Fig. 13). The temperature distribution (Fig. 13a) shows a very strong gradient, as the bottom temperature is forced to the ocean water temperature, whereas the surface cools from radiation loss and sensible and latent heat exchange. The relatively warm sea ice compared to the air temperature results in a latent heat flux directed to the atmosphere, even though relative humidity is 100%. The evaporation at the top of the sea ice leads to an outflow of fresh water at the top of the snowpack, resulting in an accumulation of salt near 10 the surface (e.g., Kaleschke et al., 2004; Domine et al., 2005). This is found in Fig. 13b and Fig. 13c in a salty slush layer at the surface with high LWC and high bulk salinity. The brine salinity (Fig. 13d) mimics the temperature distribution (Fig. 13a), because of the forced thermal equilibrium with the brine by the model. When the ice is very thin, the evaporation at the top of the ice causes an influx of salt at the bottom (Fig. 13e). The transport of salt from below decreases with increasing ice thickness, as capillary forces are not strong enough anymore to bridge the freeboard.

15 5 Outlook

Here, we showed crucial modifications to the SNOWPACK model with the primary goal of simulating the snow covering sea ice. As we initially focus on the Southern Ocean, the modifications centered around liquid water percolation in the snow, and flooding with ocean water of the snow layer. These are crucial processes to simulate for interpreting snow height measurements.

Nevertheless, these first sets of simulations revealed several directions for future improvements. First of all, the used relationship between temperature and brine salinity (Eq. 2) is only valid for temperatures close to the melting temperature of 20 water. Other relationships have been proposed (Vancoppenolle et al., 2019) and may be important to include for more accurate simulations.

Brine dynamics in sea ice is a very complex process. Particularly gravity drainage of brine is complex to simulate (Notz and Worster, 2009) and can have a profound influence on bulk salinity profiles. Typically, a decreasing bulk salinity is found 25 with increasing floe thickness, due to gravity drainage (Kovacs, 1996). The current model framework is not able to reproduce this. Furthermore, cooling of thin ice during the freezing process increases the pressure in the brine pockets, which can cause upward brine migration and higher salinity near the sea ice surface. Our simulations show this as a result of an evaporative flux. However, this effect may potentially be described by an additional term to the capillary pressure (Eq. 4).

The Crank-Nicolson scheme used for the transport equation causes some numerical instabilities, particularly when the 30 volumetric ice content is at a prescribed upper limit of 99%. This is a known problem with the Crank-Nicolson scheme (Østerby, 2003), and could be mitigated by using other numerical schemes.

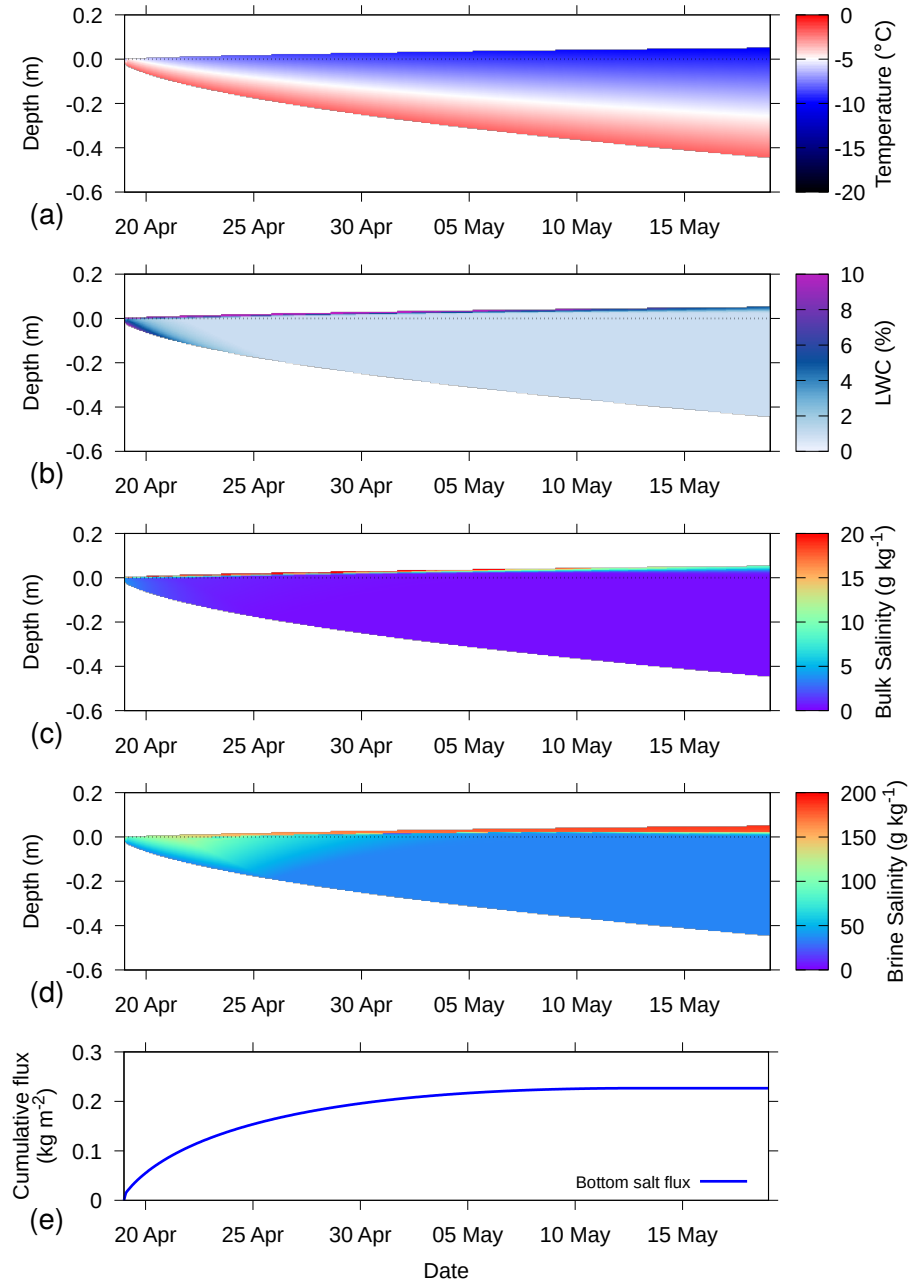


Figure 13. Simulation for ice growth of thin ice, for (a) temperature, (b) LWC, (c) bulk salinity, (d) brine salinity and (e) cumulative salt flux at the top and bottom of the sea ice. In (a), (b), (c), and (d), the depth on the y-axis is defined relative to sea level. An increasing cumulative flux denotes inflow and vice versa.

6 Conclusions

We introduced a series of modifications to the physics-based, multi-layer SNOWPACK model for simulations of the snow – sea ice system. The thermodynamic description in the model was modified to account for the varying melting point of ice based on salinity and adding domain restructuring to allow basal ice growth. Water transport through the snow – sea ice system can 5 optionally be described by the Richards equation, which describes water flow in porous media for the full range from saturated conditions (Darcy law) to unsaturated conditions. This equation is coupled to a concentration equation for salinity. With the adapted model, we explicitly describe several aspects of brine dynamics, such as flooding, superimposed ice formation and the percolation of fresh water from snow melt, flushing the sea ice. The model formulations allow for a certain amount of drainage of dense brine, but the process is largely underestimated compared to what is known from literature, as convective 10 brine transport is, thus far, not described by the model.

The snow microstructure descriptions previously developed in the SNOWPACK model can now be applied for sea ice conditions as well. The model is able to simulate the temporal evolution of snow density, grain size and shape and snow wetness over the life span of an ice floe. We find abundant depth hoar layers and melt layers, as well as superimposed ice formation due to flooding and percolation. The detailed snow microstructure evolution has the potential to be used to improve 15 remote sensing retrieval algorithms to assess snow depth and ice thickness from space and driving radiative transfer models such as the Snow Microwave Radiative Transfer model SMRT (Picard et al., 2018).

Driving the simulations using reanalysis model output seems to work well, apart from uncertainties in estimating the ocean heat flux from below and estimating precipitation amounts. The ability of SNOWPACK to use the in-situ snow depth to determine snow fall amounts was found to be useful for assessing the mass balance, but is difficult to upscale due to limited 20 measurement data from polar regions. The simulations based on Snow and IMB Buoy data demonstrate however the importance of such remote data collection systems for modelling.

Code and data availability. The SNOWPACK model and the MeteoIO meteorological preprocessing library (Bavay and Egger, 2014) needed to run SNOWPACK are available under a LGPLv3 license under <https://models.slf.ch>. The source code of the version used for the simulations presented in this study is available in the Online Supplement, and corresponds to revision 2508 of MeteoIO (<https://models.slf.ch/svn/meteoio/trunk>) and revision 1799 of SNOWPACK (<https://models.slf.ch/svn/snowpack/branches/dev>). The source code, input and configuration files, as well 25 as run, postprocessing and plotting scripts for the example simulations in this study are also available in the Online Supplement. The website <https://niviz.org/> can be used to visualize the SNOWPACK output files.

The data for Snow Buoys 2014S12 and 2016S31 can be acquired via doi: 10.1594/PANGAEA.875272 (Nicolaus and Schwegmann, 2017) and doi: 10.1594/PANGAEA.875287 (Arndt et al., 2017), respectively. IMB data from Buoy 2016T41 are available at <http://www.meereisportal.de>, direct link: http://data.meereisportal.de/gallery/index_new.php?active-tab1=method&buoytype=TB®ion=s&buoystate=inactive&submit3=display&lang=en_US&active-tab2=buoy. ERA5 data can be accessed via doi: 10.5065/D6X34W69 (ERA, 2017).

Author contributions. NW developed the model code and performed the simulations, LR performed code testing, LR, NM, KL, LK, MN and ML contributed to model conceptualization and design. NW prepared the manuscript with contributions from all co-authors.

Acknowledgements

We thank the captain, officers and crew of R/V Polarstern for their support during the campaigns to deploy the Snow Bouys and IMBs. Louisa von Hülsen from the Alfred Wegener Institute is acknowledged for providing preliminary IMB analysis data. N.W. was supported by the Swiss National Science Foundation (SNSF), grant no. P2ELP2_172299. This work was additionally supported by the US National Science Foundation (NSF) grant no. OPP-1142075 and Swiss National Science Foundation grant no. PZ00P2_142684. We also thank the German Research Council (DFG) for funding the Snow cover impacts on Antarctic Sea Ice (SCASI) project within the framework of the priority program "Antarctic Research with comparative investigations in Arctic ice areas" (grant no: NI 1096/5-1 and KA 2694/7-1). The Helmholtz infrastructure programs FRAM and ACROSS is acknowledged for funding the Snow and Ice Mass-balance Buoys. ERA5 data constitute modified Copernicus Climate Change Service Information [2018].

References

ERA5 Reanalysis, <https://doi.org/10.5065/D6X34W69>, 2017.

Ackley, S. F., Xie, H., and Tichenor, E. A.: Ocean heat flux under Antarctic sea ice in the Bellingshausen and Amundsen Seas: two case studies, *Ann. Glaciol.*, 56, 200–210, <https://doi.org/10.3189/2015AoG69A890>, 2015.

5 Allison, I., Brandt, R. E., and Warren, S. G.: East Antarctic sea ice: Albedo, thickness distribution, and snow cover, *J. Geophys. Res.*, 98, 12 417–12 429, <https://doi.org/10.1029/93JC00648>, <http://dx.doi.org/10.1029/93JC00648>, 1993.

Anderson, E., Bai, Z., Bischof, C., Blackford, S., Demmel, J., Dongarra, J., Du Croz, J., Greenbaum, A., Hammarling, S., McKenney, A., and Sorensen, D.: LAPACK Users' Guide, Society for Industrial and Applied Mathematics, Philadelphia, PA, third edn., 1999.

Andreas, E. L.: Parameterizing Scalar Transfer over Snow and Ice: A Review, *J. Hydrometeor.*, 3, 417–432, [https://doi.org/10.1175/1525-7541\(2002\)003<0417:PSTOSA>2.0.CO;2](https://doi.org/10.1175/1525-7541(2002)003<0417:PSTOSA>2.0.CO;2), 2002.

10 Arndt, S. and Paul, S.: Variability of Winter Snow Properties on Different Spatial Scales in the Weddell Sea, *J. Geophys. Res.*, 123, 8862–8876, <https://doi.org/10.1029/2018JC014447>, <https://agupubs.onlinelibrary.wiley.com/doi/abs/10.1029/2018JC014447>, 2018.

15 Arndt, S., Rossmann, L., and Nicolaus, M.: Snow height on sea ice and sea ice drift from autonomous measurements from buoy 2016S31, deployed during POLARSTERN cruise PS96 (ANT-XXXI/2), PANGAEA, <https://doi.org/10.1594/PANGAEA.875287>, <https://doi.org/10.1594/PANGAEA.875287>, in: Nicolaus, Marcel; Hoppmann, Mario; Arndt, Stefanie; Hendricks, Stefan; Katlein, Christian; König-Langlo, Gert; Nicolaus, Anja; Rossmann, Leonard; Schiller, Martin; Schwegmann, Sandra; Langevin, Danielle; Bartsch, Annekathrin (2017): Snow height and air temperature on sea ice from Snow Buoy measurements. Alfred Wegener Institute, Helmholtz Centre for Polar and Marine Research, Bremerhaven, PANGAEA, <https://doi.org/10.1594/PANGAEA.875638>, 2017.

Assur, A.: Composition of sea ice and its tensile strength, Research report 44, U.S. Army Snow, Ice and Permafrost Research Establishment, 20 Corps of Engineers, Wilmette, Ill., 1960.

20 Bartelt, P. and Lehning, M.: A physical SNOWPACK model for the Swiss avalanche warning Part I: Numerical model, *Cold Reg. Sci. Technol.*, 35, 123–145, [https://doi.org/10.1016/S0165-232X\(02\)00074-5](https://doi.org/10.1016/S0165-232X(02)00074-5), 2002.

Baunach, T., Fierz, C., Satyawali, P. K., and Schneebeli, M.: A model for kinetic grain growth, *Ann. Glaciol.*, 32, 1–6, <https://doi.org/10.3189/172756401781819427>, 2001.

25 Bavay, M. and Egger, T.: MeteoIO 2.4.2: a preprocessing library for meteorological data, *Geosci. Model Dev.*, 7, 3135–3151, <https://doi.org/10.5194/gmd-7-3135-2014>, <http://www.geosci-model-dev.net/7/3135/2014/>, 2014.

Bitz, C. M. and Lipscomb, W. H.: An energy-conserving thermodynamic model of sea ice, *J. Geophys. Res.*, 104, 15 669–15 677, <https://doi.org/10.1029/1999JC900100>, <http://dx.doi.org/10.1029/1999JC900100>, 1999.

Brandt, R. E., Warren, S. G., Worby, A. P., and Grenfell, T. C.: Surface Albedo of the Antarctic Sea Ice Zone, *J. Climate*, 18, 3606–3622, 30 <https://doi.org/10.1175/JCLI3489.1>, <https://doi.org/10.1175/JCLI3489.1>, 2005.

Brun, E., David, P., Sudul, M., and Brunot, G.: A numerical model to simulate snow-cover stratigraphy for operational avalanche forecasting, *J. Glaciol.*, 38, 13–22, 1992.

Buckingham, E.: Studies on the movement of soil moisture, Bureau of Soils, Bulletin 38, United States Department of Agriculture, Washington, DC, 1907.

35 Calonne, N., Flin, F., Morin, S., Lesaffre, B., du Roscoat, S. R., and Geindreau, C.: Numerical and experimental investigations of the effective thermal conductivity of snow, *Geophys. Res. Lett.*, 38, L23 501, <https://doi.org/10.1029/2011GL049234>, 2011.

Calonne, N., Geindreau, C., Flin, F., Morin, S., Lesaffre, B., Rolland du Roscoat, S., and Charrier, P.: 3-D image-based numerical computations of snow permeability: links to specific surface area, density, and microstructural anisotropy, *Cryosphere*, 6, 939–951, <https://doi.org/10.5194/tc-6-939-2012>, 2012.

Celia, M. A., Bouloutas, E. T., and Zarba, R. L.: A general mass-conservative numerical solution for the unsaturated flow equation, *Water Resour. Res.*, 26, 1483–1496, <https://doi.org/10.1029/WR026i007p01483>, 1990.

5 Chung, Y.-C., Bélair, S., and Mailhot, J.: Simulation of Snow on Arctic Sea Ice Using a Coupled Snow–Ice Model, *J. Hydrometeor.*, 11, 199–210, <https://doi.org/10.1175/2009JHM1112.1>, <https://doi.org/10.1175/2009JHM1112.1>, 2010.

Courant, R., Friedrichs, K., and Lewy, H.: Über die partiellen Differenzengleichungen der mathematischen Physik, *Math. Ann.*, 100, 32–74, <https://doi.org/10.1007/BF01448839>, in German., 1928.

10 Cox, G. F. N. and Weeks, W. F.: Salinity Variations in Sea Ice, *J. Glaciol.*, 13, 109–120, <https://doi.org/10.3189/S0022143000023418>, 1974.

Crank, J. and Nicolson, P.: A practical method for numerical evaluation of solutions of partial differential equations of the heat-conduction type, *Advances in Computational Mathematics*, 6, 207–226, <https://doi.org/10.1007/BF02127704>, <https://doi.org/10.1007/BF02127704>, 1996.

Curry, J. A., Schramm, J. L., and Ebert, E. E.: Sea Ice-Albedo Climate Feedback Mechanism, *J. Climate*, 8, 240–247, [https://doi.org/10.1175/1520-0442\(1995\)008<0240:SIACFM>2.0.CO;2](https://doi.org/10.1175/1520-0442(1995)008<0240:SIACFM>2.0.CO;2), 1995.

15 Déry, S. J. and Tremblay, L.-B.: Modeling the Effects of Wind Redistribution on the Snow Mass Budget of Polar Sea Ice, *J. Phys. Oceanogr.*, 34, 258–271, [https://doi.org/10.1175/1520-0485\(2004\)034<0258:MTEOWR>2.0.CO;2](https://doi.org/10.1175/1520-0485(2004)034<0258:MTEOWR>2.0.CO;2), 2004.

Domine, F., Sparapani, R., Ianniello, A., and Beine, H. J.: The origin of sea salt in snow on Arctic sea ice and in coastal regions, *Atmos. Chem. Phys.*, 4, 2259–2271, <https://doi.org/10.5194/acp-4-2259-2004>, 2004.

20 Domine, F., Taillandier, A. S., Simpson, W. R., and Severin, K.: Specific surface area, density and microstructure of frost flowers, *Geophys. Rese. Lett.*, 32, L13 502, <https://doi.org/10.1029/2005GL023245>, <https://agupubs.onlinelibrary.wiley.com/doi/abs/10.1029/2005GL023245>, 2005.

Domine, F., Picard, G., Morin, S., Barrere, M., Madore, J.-B., and Langlois, A.: Major Issues in Simulating Some Arctic Snowpack Properties Using Current Detailed Snow Physics Models: Consequences for the Thermal Regime and Water Budget of Permafrost, *J. Adv. Model. Earth Sy.*, 11, 34–44, <https://doi.org/10.1029/2018MS001445>, <https://agupubs.onlinelibrary.wiley.com/doi/abs/10.1029/2018MS001445>, 2019.

25 Drinkwater, M. R. and Crocker, G.: Modelling Changes in Scattering Properties of the Dielectric and Young Snow-Covered Sea Ice at GHz frequencies, *J. Glaciol.*, 34, 274–282, <https://doi.org/10.3189/S0022143000007012>, 1988.

Eicken, H., Lange, M. A., and Wadhams, P.: Characteristics and distribution patterns of snow and meteoric ice in the Weddell Sea and their 30 contribution to the mass balance of sea ice, *Ann. Geophys.*, 12, 80–93, <https://doi.org/10.1007/s00585-994-0080-x>, <http://dx.doi.org/10.1007/s00585-994-0080-x>, 1994.

Eicken, H., Fischer, H., and Lemke, P.: Effects of the snow cover on Antarctic sea ice and potential modulation of its response to climate change, *Ann. Glaciol.*, 21, 369–376, <https://doi.org/10.3189/S0260305500016086>, 1995.

35 Ferrari, R., Jansen, M. F., Adkins, J. F., Burke, A., Stewart, A. L., and Thompson, A. F.: Antarctic sea ice control on ocean circulation in present and glacial climates, *PNAS*, <https://doi.org/10.1073/pnas.1323922111>, <http://www.pnas.org/content/early/2014/05/29/1323922111>, 2014.

Fuller, M. C., Geldsetzer, T., Yackel, J., and Gill, J. P. S.: Comparison of a coupled snow thermodynamic and radiative transfer model with in situ active microwave signatures of snow-covered smooth first-year sea ice, *Cryosphere*, 9, 2149–2161, <https://doi.org/10.5194/tc-9-2149-2015>, <https://www.the-cryosphere.net/9/2149/2015/>, 2015.

Gallet, J.-C., Merkouriadi, I., Liston, G. E., Polashenski, C., Hudson, S., R"osel, A., and Gerland, S.: Spring snow conditions on Arctic sea ice north of Svalbard, during the Norwegian Young Sea ICE (N-ICE2015) expedition, *J. Geophys. Res.*, 122, 10,820–10,836, <https://doi.org/10.1002/2016JD026035>, <https://agupubs.onlinelibrary.wiley.com/doi/abs/10.1002/2016JD026035>, 2017.

Golden, K. M., Eicken, H., Heaton, A. L., Miner, J., Pringle, D. J., and Zhu, J.: Thermal evolution of permeability and microstructure in sea ice, *Geophys. Res. Lett.*, 34, <https://doi.org/10.1029/2007GL030447>, <https://agupubs.onlinelibrary.wiley.com/doi/abs/10.1029/2007GL030447>, 2007.

10 Goosse, H. and Fichefet, T.: Importance of ice-ocean interactions for the global ocean circulation: A model study, *J. Geophys. Res.*, 104, 23 337–23 355, <https://doi.org/10.1029/1999JC900215>, <https://agupubs.onlinelibrary.wiley.com/doi/abs/10.1029/1999JC900215>, 1999.

Gordon, A. L.: The Southern-Ocean and Global Climate, *Oceanus*, 31, 39–46, 1988.

Grenfell, T. C. and Perovich, D. K.: Spectral albedos of sea ice and incident solar irradiance in the southern Beaufort Sea, *J. Geophys. Res.*, 89, 3573–3580, <https://doi.org/10.1029/JC089iC03p03573>, <https://agupubs.onlinelibrary.wiley.com/doi/abs/10.1029/JC089iC03p03573>, 1984.

15 Griewank, P. J. and Notz, D.: Insights into brine dynamics and sea ice desalination from a 1-D model study of gravity drainage, *J. Geophys. Res.*, 118, 3370–3386, <https://doi.org/10.1002/jgrc.20247>, 2013.

Groot Zwaftink, C. D., Cagnati, A., Crepaz, A., Fierz, C., Macelloni, G., Valt, M., and Lehning, M.: Event-driven deposition of snow on the Antarctic Plateau: analyzing field measurements with SNOWPACK, *Cryosphere*, 7, 333–347, <https://doi.org/10.5194/tc-7-333-2013>, 2013.

20 Grosfeld, K., Treffeisen, R., Asseng, J., Bartsch, A., Bräuer, B., Fritzsch, B., Gerdts, R., Hendricks, S., Hiller, W., Heygster, G., Krumpen, T., Lemke, P., Melsheimer, C., Nicolaus, M., Ricker, R., and Weigelt, M.: Online sea-ice knowledge and data platform <www.meereisportal.de>, *Polarforschung*, 85, 143–155, <https://doi.org/10.2312/polfor.2016.011>, 2015.

Haas, C., Thomas, D. N., and Bareiss, J.: Surface properties and processes of perennial Antarctic sea ice in summer, *J. Glaciol.*, 47, 613–625, <https://doi.org/10.3189/172756501781831864>, 2001.

25 Haas, C., Beckers, J., King, J., Silis, A., Stroeve, J., Wilkinson, J., Notenboom, B., Schweiger, A., and Hendricks, S.: Ice and Snow Thickness Variability and Change in the High Arctic Ocean Observed by In Situ Measurements, *Geophys. Res. Lett.*, 44, 10,462–10,469, <https://doi.org/10.1002/2017GL075434>, <https://agupubs.onlinelibrary.wiley.com/doi/abs/10.1002/2017GL075434>, 2017.

Haverkamp, R. and Vauclin, M.: A note on estimating finite difference interblock hydraulic conductivity values for transient unsaturated flow problems, *Water Resour. Res.*, 15, 181–187, <https://doi.org/10.1029/WR015i001p00181>, 1979.

30 Hunke, E. C., Notz, D., Turner, A. K., and Vancoppenolle, M.: The multiphase physics of sea ice: a review for model developers, *Cryosphere*, 5, 989–1009, <https://doi.org/10.5194/tc-5-989-2011>, <https://www.the-cryosphere.net/5/989/2011/>, 2011.

Huwald, H., Tremblay, L.-B., and Blatter, H.: A multilayer sigma-coordinate thermodynamic sea ice model: Validation against Surface Heat Budget of the Arctic Ocean (SHEBA)/Sea Ice Model Intercomparison Project Part 2 (SIMIP2) data, *J. Geophys. Res.*, 110, C05 010, <https://doi.org/10.1029/2004JC002328>, <https://agupubs.onlinelibrary.wiley.com/doi/abs/10.1029/2004JC002328>, 2005.

35 Jackson, K., Wilkinson, J., Maksym, T., Meldrum, D., Beckers, J., Haas, C., and Mackenzie, D.: A Novel and Low-Cost Sea Ice Mass Balance Buoy, *J. Atmos. Ocean Technol.*, 30, 2676–2688, <https://doi.org/10.1175/JTECH-D-13-00058.1>, <https://doi.org/10.1175/JTECH-D-13-00058.1>, 2013.

Jeffries, M. O., Morris, K., Weeks, W., and Worby, A. P.: Seasonal variations in the properties and structural composition of sea ice and snow cover in the Bellingshausen and Amundsen Seas, Antarctica, *J. Glaciol.*, 43, 138–151, <https://doi.org/10.3198/1997JoG43-143-138-151>, 1997.

Jordan, R. E., Andreas, E. L., and Makshtas, A. P.: Heat budget of snow-covered sea ice at North Pole 4, *J. Geophys. Res.*, 104, 7785–7806, 5 <https://doi.org/10.1029/1999JC900011>, <https://agupubs.onlinelibrary.wiley.com/doi/abs/10.1029/1999JC900011>, 1999.

Kaleschke, L., Richter, A., Burrows, J., Afe, O., Heygster, G., Notholt, J., Rankin, A. M., Roscoe, H. K., Hollwedel, J., Wagner, T., and Jacobi, H.-W.: Frost flowers on sea ice as a source of sea salt and their influence on tropospheric halogen chemistry, *Geophysical Research Letters*, 31, L16 114, <https://doi.org/10.1029/2004GL020655>, <https://agupubs.onlinelibrary.wiley.com/doi/abs/10.1029/2004GL020655>, 2004.

Kovacs, A.: Sea Ice. Part I. Bulk Salinity Versus Floe Thickness, CRREL report, U.S. Army Cold Regions Research and Engineering 10 Laboratory, 1996.

Lecomte, O., Fichefet, T., Vancoppenolle, M., and Nicolaus, M.: A new snow thermodynamic scheme for large-scale sea-ice models, *Ann. Glaciol.*, 52, 337–346, 2011.

Ledley, T. S.: Snow on sea ice: Competing effects in shaping climate, *J. Geophys. Res.*, 96, 17 195–17 208, 15 <https://doi.org/10.1029/91JD01439>, <https://agupubs.onlinelibrary.wiley.com/doi/abs/10.1029/91JD01439>, 1991.

Lehning, M., Bartelt, P., Brown, B., Russi, T., Stöckli, U., and Zimmerli, M.: SNOWPACK calculations for avalanche warning based upon a new network of weather and snow stations, *Cold Reg. Sci. Technol.*, 30, 145–157, [https://doi.org/10.1016/S0165-232X\(99\)00022-1](https://doi.org/10.1016/S0165-232X(99)00022-1), 1999.

Lehning, M., Bartelt, P., Brown, B., Fierz, C., and Satyawali, P.: A physical SNOWPACK model for the Swiss avalanche warning Part II: Snow microstructure, *Cold Reg. Sci. Technol.*, 35, 147–167, [https://doi.org/10.1016/S0165-232X\(02\)00073-3](https://doi.org/10.1016/S0165-232X(02)00073-3), 2002a.

Lehning, M., Bartelt, P., Brown, B., and Fierz, C.: A physical SNOWPACK model for the Swiss avalanche warning Part III: Meteorological 20 forcing, thin layer formation and evaluation, *Cold Reg. Sci. Technol.*, 35, 169–184, [https://doi.org/10.1016/S0165-232X\(02\)00072-1](https://doi.org/10.1016/S0165-232X(02)00072-1), 2002b.

Leonard, K. C. and Maksym, T.: The importance of wind-blown snow redistribution to snow accumulation on Bellingshausen Sea ice, *Ann. Glaciol.*, 52, 271–278, <https://doi.org/10.3189/172756411795931651>, 2011.

Lewis, M., Tison, J., Weissling, B., Delille, B., Ackley, S., Brabant, F., and Xie, H.: Sea ice and snow cover characteristics during 25 the winter-spring transition in the Bellingshausen Sea: An overview of SIMBA 2007, *Deep-Sea Res. Pt. II*, 58, 1019–1038, <https://doi.org/10.1016/j.dsr2.2010.10.027>, 2011.

Liston, G. E., Polashenski, C., Rösel, A., Itkin, P., King, J., Merkouriadi, I., and Haapala, J.: A Distributed Snow-Evolution Model for Sea-Ice Applications (SnowModel), *J. Geophys. Res.*, 123, 3786–3810, <https://doi.org/10.1002/2017JC013706>, <https://agupubs.onlinelibrary.wiley.com/doi/abs/10.1002/2017JC013706>, 2018.

Maksym, T. and Jeffries, M. O.: A one-dimensional percolation model of flooding and snow ice formation on Antarctic sea ice, *J. Geophys. Res.*, 105, 26 313–26 331, <https://doi.org/10.1029/2000JC900130>, 2000.

Markus, T. and Cavalieri, D. J.: Snow Depth Distribution Over Sea Ice in the Southern Ocean from Satellite Passive Microwave Data, pp. 19–39, American Geophysical Union (AGU), <https://doi.org/10.1029/AR074p0019>, <https://agupubs.onlinelibrary.wiley.com/doi/abs/10.1029/AR074p0019>, 1998.

Massel, S. R.: Internal Gravity Waves in the Shallow Seas, Springer International Publishing, Switzerland, <https://doi.org/10.1007/978-3-319-18908-6>, 2015.

Massom, R. A., Drinkwater, M. R., and Haas, C.: Winter snow cover on sea ice in the Weddell Sea, *J. Geophys. Res.*, 102, 1101–1117, 35 <https://doi.org/10.1029/96JC02992>, 1997.

Massom, R. A., Drinkwater, M. R., and Haas, C.: Winter snow cover on sea ice in the Weddell Sea, *J. Geophys. Res.*, 102, 1101–1117, <https://doi.org/10.1029/96JC02992>, <https://agupubs.onlinelibrary.wiley.com/doi/abs/10.1029/96JC02992>, 1998.

Massom, R. A., Eicken, H., Hass, C., Jeffries, M. O., Drinkwater, M. R., Sturm, M., Worby, A. P., Wu, X., Lytle, V. I., Ushio, S., Morris, K., Reid, P. A., Warren, S. G., and Allison, I.: Snow on Antarctic sea ice, *Rev. Geophys.*, 39, 413–445, <https://doi.org/10.1029/2000RG000085>, 5 2001.

Maykut, G. A. and Untersteiner, N.: Some results from a time-dependent thermodynamic model of sea ice, *J. Geophys. Res.*, 76, 1550–1575, <https://doi.org/10.1029/JC076i006p01550>, <https://agupubs.onlinelibrary.wiley.com/doi/abs/10.1029/JC076i006p01550>, 1971.

Merkouriadi, I., Gallet, J.-C., Graham, R. M., Liston, G. E., Polashenski, C., Rösel, A., and Gerland, S.: Winter snow conditions on Arctic sea ice north of Svalbard during the Norwegian young sea ICE (N-ICE2015) expedition, *J. Geophys. Res.*, 122, 10,837–10,854, 10 <https://doi.org/10.1002/2017JD026753>, <https://agupubs.onlinelibrary.wiley.com/doi/abs/10.1002/2017JD026753>, 2017.

Mualem, Y.: A new model for predicting the hydraulic conductivity of unsaturated porous media, *Water Resour. Res.*, 12, 513–522, <https://doi.org/10.1029/WR012i003p00513>, 1976.

Nicolaus, M. and Schwegmann, S.: Snow height on sea ice and sea ice drift from autonomous measurements from buoy 2014S12, deployed during POLARSTERN cruise PS82 (ANT-XXIX/9), PANGAEA, <https://doi.org/10.1594/PANGAEA.875272>, <https://doi.org/10.1594/PANGAEA.875272>, in: Nicolaus, Marcel; Hoppmann, Mario; Arndt, Stefanie; Hendricks, Stefan; Katlein, Christian; König-Langlo, Gert; Nicolaus, Anja; Rossmann, Leonard; Schiller, Martin; Schwegmann, Sandra; Langevin, Danielle; Bartsch, Annekathrin (2017): Snow height and air temperature on sea ice from Snow Buoy measurements. Alfred Wegener Institute, Helmholtz Centre for Polar and Marine Research, Bremerhaven, PANGAEA, <https://doi.org/10.1594/PANGAEA.875638>, 2017.

Nicolaus, M., Haas, C., and Bareiss, J.: Observations of superimposed ice formation at melt-onset on fast ice on Kongsfjorden, Svalbard, 20 *Phys. Chem. Earth*, 28, 1241–1248, <https://doi.org/10.1016/j.pce.2003.08.048>, 2003.

Nicolaus, M., Haas, C., Bareiss, J., and Willmes, S.: A model study of differences of snow thinning on Arctic and Antarctic first-year sea ice during spring and summer, *Ann. Glaciol.*, 44, 147–153, <https://doi.org/10.3189/172756406781811312>, 2006.

Nicolaus, M., Haas, C., and Willmes, S.: Evolution of first-year and second-year snow properties on sea ice in the Weddell Sea during spring-summer transition, *J. Geophys. Res.*, 114, <https://doi.org/10.1029/2008JD011227>, <https://agupubs.onlinelibrary.wiley.com/doi/abs/10.1029/2008JD011227>, 2009.

Nicolaus, M., Hoppmann, M., Arndt, S., Hendricks, S., Katlein, C., König-Langlo, G., Nicolaus, A., Rossmann, L., Schiller, M., Schwegmann, S., Langevin, D., and Bartsch, A.: Snow height and air temperature on sea ice from Snow Buoy measurements, <https://doi.org/10.1594/PANGAEA.875638>, <https://doi.org/10.1594/PANGAEA.875638>, 2017.

Notz, D.: Challenges in simulating sea ice in Earth System Models, *WIREs Clim. Change*, 3, 509–526, <https://doi.org/10.1002/wcc.189>, 30 <https://onlinelibrary.wiley.com/doi/abs/10.1002/wcc.189>, 2012.

Notz, D. and Worster, M. G.: Desalination processes of sea ice revisited, *J. Geophys. Res.*, 114, <https://doi.org/10.1029/2008JC004885>, <https://agupubs.onlinelibrary.wiley.com/doi/abs/10.1029/2008JC004885>, 2009.

Obleitner, F. and Lehning, M.: Measurement and simulation of snow and superimposed ice at the Kongsvegen glacier, Svalbard (Spitzbergen), *J. Geophys. Res.*, 109, <https://doi.org/10.1029/2003JD003945>, <https://agupubs.onlinelibrary.wiley.com/doi/abs/10.1029/2003JD003945>, 35 2004.

Østerby, O.: Five Ways of Reducing the Crank–Nicolson Oscillations, *BIT Numerical Mathematics*, 43, 811–822, <https://doi.org/10.1023/B:BITN.0000009942.00540.94>, <https://doi.org/10.1023/B:BITN.0000009942.00540.94>, 2003.

Perovich, D., Jones, K., Light, B., Eicken, H., Markus, T., Stroeve, J., and Lindsay, R.: Solar partitioning in a changing Arctic sea-ice cover, *Ann. Glaciol.*, 52, 192–196, <https://doi.org/10.3189/172756411795931543>, 2011.

Petty, A. A., Webster, M., Boisvert, L., and Markus, T.: The NASA Eulerian Snow on Sea Ice Model (NESOSIM) v1.0: initial model development and analysis, *Geosci. Model Dev.*, 11, 4577–4602, <https://doi.org/10.5194/gmd-11-4577-2018>, <https://www.geosci-model-dev.net/11/4577/2018/>, 2018.

Picard, G., Sandells, M., and Löwe, H.: SMRT: an active–passive microwave radiative transfer model for snow with multiple microstructure and scattering formulations (v1.0), *Geosci. Model Dev.*, 11, 2763–2788, <https://doi.org/10.5194/gmd-11-2763-2018>, <https://www.geosci-model-dev.net/11/2763/2018/>, 2018.

Poisson, A. and Papa, A.: Diffusion coefficients of major ions in seawater, *Mar. Chem.*, 13, 265–280, [https://doi.org/10.1016/0304-4203\(83\)90002-6](https://doi.org/10.1016/0304-4203(83)90002-6), 1983.

Powell, D. C., Markus, T., Cavalieri, D. J., Gasiewski, A. J., Klein, M., Maslanik, J. A., Stroeve, J. C., and Sturm, M.: Microwave Signatures of Snow on Sea Ice: Modeling, *IEEE T. Geosci. Remote*, 44, 3091–3102, <https://doi.org/10.1109/TGRS.2006.882139>, 2006.

Rankin, A. M., Wolff, E. W., and Martin, S.: Frost flowers: Implications for tropospheric chemistry and ice core interpretation, *J. Geophys. Res.*, 107, <https://doi.org/10.1029/2002JD002492>, <https://agupubs.onlinelibrary.wiley.com/doi/abs/10.1029/2002JD002492>, 2002.

Ricker, R., Hendricks, S., Helm, V., Skourup, H., and Davidson, M.: Sensitivity of CryoSat-2 Arctic sea-ice freeboard and thickness on radar-waveform interpretation, *Cryosphere*, 8, 1607–1622, <https://doi.org/10.5194/tc-8-1607-2014>, <https://www.the-cryosphere.net/8/1607/2014/>, 2014.

Steger, C. R., Reijmer, C. H., van den Broeke, M. R., Wever, N., Forster, R. R., Koenig, L. S., Kuipers Munneke, P., Lehning, M., Lhermitte, S., Ligtenberg, S. R. M., Miège, C., and Noël, B. P. Y.: Firn Meltwater Retention on the Greenland Ice Sheet: A Model Comparison, *Front. Earth Sci.*, 5, 3, <https://doi.org/10.3389/feart.2017.00003>, <https://www.frontiersin.org/article/10.3389/feart.2017.00003>, 2017.

Sturm, M., Holmgren, J., and Perovich, D. K.: Winter snow cover on the sea ice of the Arctic Ocean at the Surface Heat Budget of the Arctic Ocean (SHEBA): Temporal evolution and spatial variability, *J. Geophys. Res.*, 107, SHE 23–1–SHE 23–17, <https://doi.org/10.1029/2000JC000400>, 8047, 2002a.

Sturm, M., Perovich, D. K., and Holmgren, J.: Thermal conductivity and heat transfer through the snow on the ice of the Beaufort Sea, *J. Geophys. Res.*, 107, SHE 19–1–SHE 19–17, <https://doi.org/10.1029/2000JC000409>, <https://agupubs.onlinelibrary.wiley.com/doi/abs/10.1029/2000JC000409>, 2002b.

Toyota, T., Takatsuji, S., Tateyama, K., Naoki, K., and Ohshima, K. I.: Properties of sea ice and overlying snow in the Southern Sea of Okhotsk, *J. Oceanogr.*, 63, 393–411, <https://doi.org/10.1007/s10872-007-0037-2>, <https://doi.org/10.1007/s10872-007-0037-2>, 2007.

Tremblay, L.-B. and Mysak, L. A.: Modeling Sea Ice as a Granular Material, Including the Dilatancy Effect, *J. Phys. Oceanogr.*, 27, 2342–2360, [https://doi.org/10.1175/1520-0485\(1997\)027<2342:MSIAAG>2.0.CO;2](https://doi.org/10.1175/1520-0485(1997)027<2342:MSIAAG>2.0.CO;2), 1997.

Trujillo, E., Leonard, K., Maksym, T., and Lehning, M.: Changes in snow distribution and surface topography following a snowstorm on Antarctic sea ice, *J. Geophys. Res.*, 121, 2172–2191, <https://doi.org/10.1002/2016JF003893>, <https://agupubs.onlinelibrary.wiley.com/doi/abs/10.1002/2016JF003893>, 2016.

Turner, A. K. and Hunke, E. C.: Impacts of a mushy-layer thermodynamic approach in global sea-ice simulations using the CICE sea-ice model, *J. Geophys. Res.*, 120, 1253–1275, <https://doi.org/10.1002/2014JC010358>, <https://agupubs.onlinelibrary.wiley.com/doi/abs/10.1002/2014JC010358>, 2014.

Ukita, J. and Martinson, D. G.: An efficient adjustable-layering thermodynamic sea-ice model formulation for high-frequency forcing, *Ann. Glaciol.*, 33, 253–260, <https://doi.org/10.3189/172756401781818194>, 2001.

van Genuchten, M. T.: A Closed-form Equation for Predicting the Hydraulic Conductivity of Unsaturated Soils, *Soil Sci. Soc. Am. J.*, 44, 892–898, <https://doi.org/10.2136/sssaj1980.03615995004400050002x>, 1980.

Vancoppenolle, M., Goosse, H., de Montety, A., Fichefet, T., Tremblay, B., and Tison, J.-L.: Modeling brine and nutrient dynamics in Antarctic sea ice: The case of dissolved silica, *J. Geophys. Res.*, 115, <https://doi.org/10.1029/2009JC005369>, <https://agupubs.onlinelibrary.wiley.com/doi/abs/10.1029/2009JC005369>, 2010.

Vancoppenolle, M., Madec, G., Thomas, M., and McDougall, T. J.: Thermodynamics of Sea Ice Phase Composition Revisited, *J. Geophys. Res.*, 124, 615–634, <https://doi.org/10.1029/2018JC014611>, <https://agupubs.onlinelibrary.wiley.com/doi/abs/10.1029/2018JC014611>, 2019.

Veldman, A. E. P. and Rinzema, K.: Playing with nonuniform grids, *Journal of Engineering Mathematics*, 26, 119–130, <https://doi.org/10.1007/BF00043231>, <https://doi.org/10.1007/BF00043231>, 1992.

Weiss, A. I., King, J., Lachlan-Cope, T., and Ladkin, R.: On the effective aerodynamic and scalar roughness length of Weddell Sea ice, *J. Geophys/ Res.*, 116, D19 119, <https://doi.org/10.1029/2011JD015949>, <https://agupubs.onlinelibrary.wiley.com/doi/abs/10.1029/2011JD015949>, 2011.

Wever, N., Lehning, M., Clifton, A., Rüedi, J.-D., Nishimura, K., Nemoto, M., Yamaguchi, S., and Sato, A.: Verification of moisture budgets during drifting snow conditions in a cold wind tunnel, *Water Resour. Res.*, 45, <https://doi.org/10.1029/2008WR007522>, <http://dx.doi.org/10.1029/2008WR007522>, w07423, 2009.

Wever, N., Fierz, C., Mitterer, C., Hirashima, H., and Lehning, M.: Solving Richards Equation for snow improves snowpack meltwater runoff estimations in detailed multi-layer snowpack model, *Cryosphere*, 8, 257–274, <https://doi.org/10.5194/tc-8-257-2014>, 2014.

Wever, N., Schmid, L., Heilig, A., Eisen, O., Fierz, C., and Lehning, M.: Verification of the multi-layer SNOWPACK model with different water transport schemes, *Cryosphere*, 9, 2271–2293, <https://doi.org/10.5194/tc-9-2271-2015>, <http://www.the-cryosphere.net/9/2271/2015/>, 2015.

Wever, N., Würzer, S., Fierz, C., and Lehning, M.: Simulating ice layer formation under the presence of preferential flow in layered snowpacks, *Cryosphere*, 10, 2731–2744, <https://doi.org/10.5194/tc-10-2731-2016>, <http://www.the-cryosphere.net/10/2731/2016/>, 2016.

Willatt, R. C., Giles, K. A., Laxon, S. W., Stone-Drake, L., and Worby, A. P.: Field Investigations of Ku-Band Radar Penetration Into Snow Cover on Antarctic Sea Ice, *IEEE T. Geosci. Remote*, 48, 365–372, <https://doi.org/10.1109/TGRS.2009.2028237>, 2010.

Yamaguchi, S., Watanabe, K., Katsushima, T., Sato, A., and Kumakura, T.: Dependence of the water retention curve of snow on snow characteristics, *Ann. Glaciol.*, 53, 6–12, <https://doi.org/10.3189/2012AoG61A001>, 2012.

Version 1 of a sea ice module for the physics based, detailed, multi-layer SNOWPACK model

Nander Wever^{1,2,3}, Leonard Rossmann⁴, Nina Maaß⁵, Katherine C. Leonard^{1,2,6}, Lars Kaleschke⁴, Marcel Nicolaus⁴, and Michael Lehning^{2,3}

¹Department of Atmospheric and Oceanic Sciences, University of Colorado Boulder, Boulder, CO, USA.

²CRYOS, School of Architecture, Civil and Environmental Engineering, EPFL, Lausanne, Switzerland.

³WSL Institute for Snow and Avalanche Research SLF, Davos, Switzerland.

⁴Alfred Wegener Institute, Helmholtz Centre for Polar and Marine Research, Bremerhaven, Germany.

⁵University of Hamburg, Institute of Oceanography, CEN, Germany.

⁶Cooperative Institute for Research in Environmental Science (CIRES), University of Colorado Boulder, Boulder, CO, USA.

Correspondence: NANDER WEVER (nander.wever@colorado.edu)

Abstract. Sea ice is an important component of the global climate system. The presence of a snowpack covering sea ice can strongly modify the thermodynamic behaviour of the sea ice, due to the low thermal conductivity and high albedo of snow. The snowpack can be ~~strongly~~ stratified and change properties (density, water content, grain size and shape) throughout the seasons. ~~Fresh water percolation during snow melt can decrease the salinity~~ Melting snow provides fresh water which can

5 form melt ponds, or cause flushing of salt out of the underlying sea ice, while flooding of the snow layer by saline ocean water can strongly impact both the ice mass balance and the freezing point of the snow. To capture the complex dynamics from the snowpack, we introduce modifications to the physics-based, multi-layer SNOWPACK model to simulate the snow-sea ice system. ~~This involves modifications~~ Adaptations to the model thermodynamics and ~~to describe a description of~~ water and salt transport through the snow – sea ice system by coupling the transport equation to the Richards equation were added.

10 These modifications allow the snow microstructure descriptions developed in the SNOWPACK model to be applied to sea ice conditions as well. Here, we drive the model with data from Snow and Ice Mass-balance Buoys installed in the Weddell Sea in Antarctica. The model is able to simulate the temporal evolution of snow density, grain size and shape, and snow wetness. The model simulations show abundant depth hoar layers and melt layers, as well as superimposed ice formation due to flooding and percolation. Gravity drainage of dense brine is underestimated as convective processes are so far neglected. Furthermore, with 15 increasing model complexity, detailed forcing data for the simulations is required, which is difficult to acquire due to limited observations in polar regions.

1 Introduction

Sea ice is an important component of the global climate system (~~Goosse and Fichefet, 1999; Ferrari et al., 2014, e.g.~~)(e.g., Goosse and Fichefet, 1999; Ferrari et al., 2014, e.g.). During the freezing process of ocean water, salt is expelled from the ice and ~~high salinity, dense~~ saline water is formed. The negative buoyancy of the resulting dense water is an important mechanism driving global ocean circulation (~~Gordon, 1988, e.g.~~)(e.g., Gordon, 1988). Sea ice also forms the interface between the ocean and the atmosphere for extended

periods of time, altering the surface energy balance (Ledley, 1991; Brandt et al., 2005; Perovich et al., 2011, e.g.) (e.g., Ledley, 1991; Brandt, 2005; Perovich et al., 2011).

Antarctic sea ice is largely snow covered (Allison et al., 1993), which has major implications for the energy and mass balance of sea ice (Eicken et al., 1995; Massom et al., 2001). The layer of snow strongly modifies the energy balance both via its high albedo (Grenfell and Perovich, 1984; Brandt et al., 2005; Perovich et al., 2011), and through the thermal conductivity of snow, which insulates the sea ice and limits ice growth (Maykut and Untersteiner, 1971; Sturm et al., 2002b). In summer, however, the high albedo of the snow cover may limit ice melt (e.g., Curry et al., 1995). The thermal conductivity of snow also varies widely based on the snow microstructural properties, indicating the need to explicitly consider those properties and their spatial and vertical variability (Calonne et al., 2011; Sturm et al., 2002b).

Although the effect of snow on the energy balance reduces sea ice growth, it can also provide a positive contribution to the mass balance of the sea ice. The flooding of sea ice by ocean water, occurring when Particularly on Antarctic sea ice, it is regularly observed that the snow cover, due to its weight, pushes the sea ice below sea level. Flooding then may occur via cracks or through the brine channels. Refreezing of the flooded layer is an important mechanism increasing the ice mass over solely thermal growth in Antarctica in addition to basal thermodynamic growth in the Southern Ocean (Eicken et al., 1994; Jeffries et al., 1997). Snow melt meltwater or rain percolating and accumulating on top of the ice may can also (re)freeze and cause the formation of superimposed ice (Haas et al., 2001; Nicolaus et al., 2003; Obleitner and Lehning, 2004). The spatial and temporal scale variability of these processes is poorly known due to the uncertainties in limited knowledge of snow cover distribution and properties.

Assessing snow amounts on sea ice is not straight-forward from atmospheric forcing alone is not straight-forward, as the local precipitation is redistributed by wind, and an unknown fraction of precipitation never accumulates over level ice as it is either blown into leads or accumulates in the lee of surface topography (Déry and Tremblay, 2004; Leonard and Maksym, 2011; Trujillo et al., 2016; Liston et al., 2018; Petty et al., 2018), or is lost due to drifting snow sublimation (e.g., Wever et al., 2009). These processes result in snow depth patterns and accumulation patterns that are typically spatially highly variable (Trujillo et al., 2016; Haas et al., 2017). Also, the wind redistribution and smoothing effect of the snow cover modifies the aerodynamic roughness of the sea ice surface, influencing the momentum flux between atmosphere and sea ice (Andreas, 2002; Weiss et al., 2011) and consequently the large-scale movement of sea ice (Tremblay and Mysak, 1997).

Snow stratigraphy over sea ice can also be highly variable in space and time, and exhibit complex microstructural layering (Massom et al., 1998, 2001; Nicolaus et al., 2009). Strong temperature gradients over shallow snow covers can lead to facetting and grain growth, resulting in layers with faceted snow depth hoar crystals (Toyota et al., 2007; Lewis et al., 2011). Often Inhomogeneities caused by wind slabs, ice layers and melt-freeze crusts during the melt season are observed have been reported for both Arctic and Antarctic sea ice (e.g., Massom et al., 1997; Sturm et al., 2002a; Gallet et al., 2017; Merkouriadi et al., 2017; Arndt and As snow on sea ice is typically relatively shallow, the often complex layering is concentrated in shallow layers, increasing the up to a few decimeter for extended periods of time, and accumulation events are small, it is a challenge for numerical models to capture the important processes accurately enough vertical variability in the snow cover accurately.

Water transport processes in the snowpack can have a strong impact on the snow microstructure and the salinity distribution in the snow – sea ice system. Surface melt can create downward water percolation, which refreezes can refreeze lower down in the snowpack as ice layers or forms form superimposed ice (Nicolaus et al., 2009), or (particularly in the Arctic) form melt ponds. Upon warming of the underlying sea ice, increased hydraulic conductivity from expanding brine channels may cause 5 freshwater to flush salt out of the underlying ice (e.g., Notz and Worster, 2009). Upward motion of liquid water has also been observed due to capillary forces (Massom et al., 1998, 2001). Capillary wicking can move salt upward, creating a salty slush layer and frost flowers at the ice surface (Rankin et al., 2002; Domine et al., 2004), which may get buried beneath snow after snow fall, impacting the salinity and water content of the lowest snow layers.

The snow cover is also important for deriving sea ice thickness and snow depth from satellite remote sensing. For example, 10 the microwave signature (e.g., Markus and Cavalieri, 1998; Drinkwater and Crocker, 1988; Powell et al., 2006) and the radar penetration (e.g., Willatt et al., 2010; Ricker et al., 2014) of snow-covered sea ice depend on the properties and layering of the snow.

A wide range of sea ice models have been developed (Bitz and Lipscomb, 1999; Maksym and Jeffries, 2000; Ukita and Martinson, 2001; 15 e.g., Bitz and Lipscomb, 1999; Maksym and Jeffries, 2000; Ukita and Martinson, 2001; Huwald et al., 2005; Griewank and Notz, 2013; 19 20 . Due to the increasing importance attributed to important role of snow on sea ice, many sea ice models include a description of the snow cover in their models (Lecomte et al., 2011; Notz, 2012). The most important factors considered by sea ice models is the albedo and the insulating effect of the snow. However, for deriving sea ice thickness and snow depth from satellite remote sensing, brightness temperatures of snow are also required. These depend strongly on snow stratigraphy and snow properties. Several studies used the snow thermodynamics model SNTHERM, either using the internal sea ice module or coupled to a sea ice model (Jordan et al., 1999; Nicolaus et al., 2006; Chung et al., 2010; Fuller et al., 2015) to improve the thermodynamical upper boundary condition for sea ice, and assessing the snow microstructure on sea ice.

Rather than improving the representation of snow in ~~sea ice models~~an existing sea ice model, this paper presents a new sea ice module developed for the ~~physics-based~~physics-based, detailed, multi-layer snow cover model SNOWPACK. Our motivation is that the SNOWPACK model has a long development history with a focus on accurately representing physical processes in the snow cover. This includes a detailed representation of snow microstructure as well as liquid water flow processes (Bartelt and Lehning, 2002; Lehning et al., 2002a, b; Wever et al., 2015, 2016). The model has previously been successfully applied in Polar regions. For example, for the Greenland Ice Sheet (Steger et al., 2017), it was found to provide accurate simulations of water flow and refreezing processes. An application to the Antarctic Plateau (Groot Zwaftink et al., 2013) showed good agreement for new snow density and temperature profiles in a drifting snow dominated environment. Here, we apply the new SNOWPACK module to the Antarctic sea ice environment and demonstrate its ability to successfully simulate snow on sea ice conditions.

2 Methods

The SNOWPACK model has seen a long development history regarding snow processes. The model calculates the snow energy balance, the resulting temperature distribution, snow settling (densification), liquid water flow and the evolution of snow microstructure. The snow microstructure is described by four parameters: grain size, bond sizeradius, sphericity and dendricity.

5 Grain size is considered the average grain size (Baunach et al., 2001) and bond radius is defined to be the minimum constriction in the connection between to grains (see Fig. 2 in Lehning et al. (2002a)). As defined in Brun et al. (1992), dendricity describes how much of the original crystal shapes are still remaining in a snow layer, where 1 corresponds to perfect dendritic snow, and 0 to perfect rounds or faceted snow. Sphericity describes the ratio of rounded versus angular shapes, where 1 denotes perfectly round shapes, and 0 describes perfectly faceted shapes. Governing state equations describe the time evolution of
10 these parameters given snow temperature, density, liquid water content (LWC), etc. The full model description is presented in Bartelt and Lehning (2002); Lehning et al. (2002a, b)Bartelt and Lehning (2002) and Lehning et al. (2002a, b).

The basic model structure of SNOWPACK is congruent with the mushy-layer theory for sea ice (Hunke et al., 2011; Turner and Hunke, 2014). The model is 1-dimensional, with an arbitrary number of vertical layers of arbitrary depth. Typical layer depth, however, is 1-2 cm. Each layers-layer's total volume is subdivided into a part consisting of respectively ice, water and air.

15 Henceforth these layers are called "snow" layers. Note that SNOWPACK also considers soil as a category, which is hereafter ignored in the context of sea ice.

The sea ice extension of the model provides modifications to the model code to include the effect of salinity on thermal properties and liquid water flow. Furthermore, ice growth and melt at the bottom of the domain is assessed. Flooding is considered to occur only in one-dimension, and lateral advection of liquid water is ignored (Maksym and Jeffries, 2000).

20 Below, we detail the modifications of the SNOWPACK model to make it suitable for sea ice simulations. The modifications are implemented in the main version of SNOWPACK, and sea ice specific settings are only needed in the configuration files for the model. The code base of the SNOWPACK model is the same and future developments in other parts of the code will also be directly available for the sea ice version.

2.1 Heat equationEquation and thermodynamicsThermodynamics

25 SNOWPACK solves the heat equation using finite elements, as described in Bartelt and Lehning (2002), allowing to have a simulated snow surface temperature as well as a temperature at the bottom of the snow column. Each snow layer, called element, has two nodes with the adjacent elements. Several modifications were necessary to take into account the effect of salinity on thermodynamical properties.

30 First, it is assumed that all salt is concentrated in the liquid water in the brine pockets and that the volumetric ice content is free of salt, such that one can write:

$$S_b = \frac{S}{\theta}. \quad (1)$$

Here, S is the bulk salinity (g kg^{-1}), S_b is the brine salinity (g kg^{-1}) and θ is the volumetric liquid water contentLWC ($\text{m}^3 \text{ m}^{-3}$).

The melting point T_m (K) of each snow element can then be expressed as a function of brine salinity by the commonly used relationship (Assur, 1960):

$$T_m = -\mu S_b + T_0, \quad (2)$$

where μ is a constant ($0.054 \text{ K (g kg}^{-1}\text{)}^{-1}$) and T_0 is the melting point of fresh water (273.15 K). [Eq. 2 is valid between 0°C and -6°C \(Vancoppenolle et al., 2019\).](#)

To solve the heat equation, we assume equilibrium between the element temperature T_e (K) and the brine melting point T_m . When the ice is heating (cooling), brine [is supposed to melt \(freeze\) instantaneously volume is assumed to increase \(decrease\) instantaneously by phase changes in the surrounding ice](#), in order to maintain $T_e = T_m$. This is achieved by feeding back the energy associated with the phase change as a source/sink term in the heat equation (see Eq. 3 in Bartelt and Lehning (2002)).

10 Note that the latent heat released [\(used\) when water freezes \(melts\) increases \(decreases\) increases](#) the temperature locally, [thus counteracting the temperature change. In turn and vice versa. These effects on local temperature would reduce the energy released during freezing or energy available for melt. Additionally, the refreezing \(melting\) ice would impact or melting of ice impacts](#) brine salinity and thereby the melting temperature. These competing processes slow down the convergence in the solver for the heat equation, which can be mitigated by providing an improved estimate of the melting temperature which 15 satisfies: (i) the condition provided by Eq. 1 for the new LWC, (ii) Eq. 2 for the new melting temperature given the new brine salinity, and (iii) the change in ice content for the given deviation of the new element temperature from the melting point, by algebraically solving these three conditions with the three unknowns.

The bottom node of the domain represents the interface between sea ice and ocean and its temperature is prescribed as a Dirichlet boundary condition using the freezing temperature of the ocean water, which is determined by the prescribed ocean 20 salinity [\(set to 35 g kg⁻¹ in this study\)](#). Typically heat is advected [in the ocean from into the sea ice from the ocean](#) below, referred to as the ocean heat flux. We determine the net energy loss or gain at the bottom node, given the prescribed ocean heat flux and the internal heat flux in the lowest sea ice element. This net energy is translated into bottom ice growth or melt.

An uncertainty for ice growth is the ice porosity of the newly formed ice. We apply a similar approach to the one presented in Griewank and Notz (2013), where an ice content threshold is defined. When the lowest element has an ice content below 25 this value, the net energy is used to create a new ice element with a brine salinity equal to ocean salinity (Vancoppenolle et al., 2010). Otherwise, the bottom element grows in length. We set a threshold of $0.99 \text{ m}^3 \text{ m}^{-3}$, which we also prescribe as the maximum allowed ice content of a single layer. Mass loss is applied by reducing the element length.

2.2 Brine dynamics

The SNOWPACK model is equipped with [two water transport schemes: a simple bucket scheme and](#) a solver for the full 30 Richards equation for transport in porous media (Wever et al., 2014). [Below, we will outline how these water transport schemes were modified for sea ice.](#)

[A general modification is that the density of liquid water \(\$\rho\$ \) is adjusted for salinity as:](#)

$$\rho = \rho_w + \beta S_b,$$

where ρ_w is the density of fresh liquid water (1000 kg m^{-3}), β is a salinity coefficient, approximated as $0.824 \text{ kg}^2 \text{ g}^{-1} \text{ m}^{-3}$ (Massel, 2015, Appendix A).

2.2.1 Bucket Scheme for simple water transport

One of the simplest approaches to simulate liquid water flow through porous media is the so-called bucket scheme, which is 5 also available for the sea ice module in SNOWPACK. The scheme is described in Wever et al. (2014). For sea ice, the bucket scheme has been extended with a simple description of flooding. The pore space of the part of the simulated domain which is located below sea level is filled with liquid water with ocean water salinity S_o . The salinity distribution of the sea ice is described by a fixed salinity profile.

The position of the sea level inside the model domain z_{SL} (m) is determined from the isostatic balance:

10

$$\text{SWE}(\rho_w + \beta S_o),$$

where SWE is the snow water equivalent, defined as the sum over all elements N of the mass of each element j in the model:

$$\text{SWE} = \sum_{j=1}^N (\theta_{i,j} \rho_i + \theta_j \rho_j) \Delta z_j,$$

where $\theta_{i,j}$ and θ_j is the volumetric content ($\text{m}^3 \text{ m}^{-3}$) for layer j of ice and water, respectively. ρ_i is the density of ice 15 (917 kg m^{-3}) and ρ_j the brine density of layer j (see Eq. 5).

2.2.1 Explicit brine dynamics

As an alternative to the bucket scheme, a solver for Here, we modified the solver for the Richards equation to account for density variations and couple the Richards equation coupled to a transport equation can be used for salinity. This provides an explicit treatment of brine dynamics. First, the Richards equation solves the liquid water flow in the snow – sea ice system, 20 keeping the salinity constant with time. After each integration of the Richards equation, the advection-diffusion equation is solved for the same time step under the assumption of constant liquid water fluxes. The time step is limited to a maximum of 15 minutes, although stability criteria for both the Richards equation as well as the advection-diffusion equation for salinity may impose additional, stricter, time constraints. Below, we detail how this scheme for liquid water transport was modified for sea ice.

Richards equation for explicit water transport

2.2.1 Richards Equation for Water Flow

The mixed form of the Richards equation reads:

$$\frac{\partial \theta}{\partial t} - \frac{\partial}{\partial z} \left[\frac{\kappa}{\eta} \frac{\partial p}{\partial z} \right] - s = 0, \quad (3)$$

5 where t is time (s), z is the vertical coordinate (m), κ is the permeability (m^2), η is the viscosity (m s^{-2}) and s is a source/sink term ($\text{m}^3 \text{ m}^{-3} \text{ s}^{-1}$). The pressure p can be considered the sum of water potential and gravity potential:

$$p = \rho gh + \rho g z \cos(\gamma) \quad (4)$$

where h is the pressure head (m), g is the gravitational acceleration (m s^{-2}), ρ the density of the flowing liquid (kg m^{-3}) and γ is the slope angle. Note that Because SNOWPACK can be used in sloped terrain. For completeness of the model description,

10 we keep this term, although for sea ice for completeness of the model description, although γ is obviously 0 for sea ice.

The density of liquid water (ρ) is adjusted for salinity according to:

$$\rho = \rho_w + \beta S_b, \quad (5)$$

where ρ_w is the density of fresh liquid water (1000 kg m^{-3}), β is a salinity coefficient, approximated as $0.824 \text{ kg}^2 \text{ g}^{-1} \text{ m}^{-3}$ (Massel, 2015, Appendix A).

15 The permeability κ is replaced by the hydraulic conductivity K , which relates to κ via:

$$K = \kappa \frac{\rho g}{\mu}, \quad (6)$$

where μ is the dynamic viscosity of water ($0.001792 \text{ kg (m s)}^{-1}$).

A critical assumption in the typical application of the Richards equation is that it is assumed that both g and ρ are constant in time and z , and consequently can be eliminated from the equation. Due to salinity variations in sea ice, variations of density 20 of the flowing liquid can occur and are actually considered the driving mechanism in the temporal and spatial evolution of the salinity of sea ice.

Therefore, we rewrite the Richards equation for sea ice by considering ρ as a function of z and only eliminating g , arriving at:

$$\frac{\partial \theta}{\partial t} - \frac{\partial}{\partial z} \left[\frac{K}{\rho} \frac{\partial}{\partial z} (\rho h + \rho z \cos(\gamma)) \right] - s = 0, \quad (7)$$

25 As outlined in Wever et al. (2014), the Richards equation is implemented in SNOWPACK by the discretization proposed by Celia et al. (1990). The backward Euler approximation in time coupled with a simple Picard iteration, as shown in Eq. 14 of Celia et al. (1990), becomes, for Eq. 7:

$$\frac{\theta^{n+1,m+1} - \theta^n}{\Delta t} - \frac{\partial}{\partial z} \left(\frac{K^{n+1,m}}{\rho} \frac{\partial \rho h^{n+1,m+1}}{\partial z} \right) - \cos(\gamma) \frac{\partial K^{n+1,m}}{\partial z} - \cos(\gamma) \frac{\partial}{\partial z} \left(\frac{K^{n+1,m}}{\rho} \frac{\partial \rho}{\partial z} \right) - s = 0, \quad (8)$$

where n and m denote the time and iteration level, respectively. Here, we have used to chain rule to write:

$$\frac{\partial}{\partial z} \left[\frac{K}{\rho} \frac{\partial}{\partial z} (\rho z) \right] = \frac{\partial}{\partial z} \left[K \frac{\partial z}{\partial z} \right] + \frac{\partial}{\partial z} \left[\frac{K}{\rho} z \frac{\partial \rho}{\partial z} \right] = \frac{\partial K}{\partial z} + \frac{\partial}{\partial z} \left[\frac{K}{\rho} z \frac{\partial \rho}{\partial z} \right] \quad (9)$$

The last term on the right hand side expresses the liquid water flow driven by density differences.

After applying a Taylor expansion to Eq. 15 of Celia et al. (1990), and defining $\delta^m \equiv \rho h^{n+1,m+1} - \rho h^{n+1,m}$, we arrive at:

$$\left(\frac{1}{\Delta t} \frac{C^{n+1,m}}{\rho} \right) \delta^m + \frac{\theta^{n+1,m} - \theta^n}{\Delta t} - \frac{\partial}{\partial z} \left(\frac{K^{n+1,m}}{\rho} \frac{\partial \rho h^{n+1,m+1}}{\partial z} \right) - \cos(\gamma) \frac{\partial K^{n+1,m}}{\partial z} - \cos(\gamma) \frac{\partial}{\partial z} \left(\frac{K^{n+1,m}}{\rho} z \frac{\partial \rho}{\partial z} \right) - s = 0. \quad (10)$$

5

Finally, Eq. 16 in Celia et al. (1990) becomes:

$$\begin{aligned} \left(\frac{1}{\Delta t} \frac{C^{n+1,m}}{\rho} \right) \delta^m - \frac{\partial}{\partial z} \left(\frac{K^{n+1,m}}{\rho} \frac{\partial \delta^m}{\partial z} \right) \\ = \frac{\partial}{\partial z} \left(\frac{K^{n+1,m}}{\rho} \frac{\partial \rho h^{n+1,m+1}}{\partial z} \right) + \cos(\gamma) \frac{\partial K^{n+1,m}}{\partial z} + \cos(\gamma) \frac{\partial}{\partial z} \left(\frac{K^{n+1,m}}{\rho} z \frac{\partial \rho}{\partial z} \right) - \frac{\theta^{n+1,m} - \theta^n}{\Delta t} + s \end{aligned} \quad (11)$$

10 After applying the standard finite difference approximation in space, Eq. 16 in Celia et al. (1990) translates into (i denoting the spatial coordinate):

$$\begin{aligned} \frac{C_i^{n+1,m}}{\rho_i} \frac{\delta_i^m}{\Delta t} - \frac{1}{(\Delta z)^2} \left[\frac{K_{i+1/2}^{n+1,m}}{\rho_{i+1/2}} (\delta_{i+1}^m - \delta_i^m) - \frac{K_{i-1/2}^{n+1,m}}{\rho_{i-1/2}} (\delta_i^m - \delta_{i-1}^m) \right] \\ = \frac{1}{(\Delta z)^2} \left[\frac{K_{i+1/2}^{n+1,m}}{\rho_{i+1/2}} (\rho_{i+1} h_{i+1}^{n+1,m} - \rho_i h_i^{n+1,m}) - \frac{K_{i-1/2}^{n+1,m}}{\rho_{i-1/2}} (\rho_i h_i^{n+1,m} - \rho_{i-1} h_{i-1}^{n+1,m}) \right] \\ 15 + \cos(\gamma) \frac{K_{i+1/2}^{n+1,m} - K_{i-1/2}^{n+1,m}}{\Delta z} + \cos(\gamma) \frac{\frac{K_{i+1/2}^{n+1,m}}{\rho_{i+1/2}} z_{i+1/2} \frac{\rho_{i+1} - \rho_i}{\Delta z} - \frac{K_{i-1/2}^{n+1,m}}{\rho_{i-1/2}} z_{i-1/2} \frac{\rho_i - \rho_{i-1}}{\Delta z}}{\Delta z} - \frac{\theta_i^{n+1,m} - \theta_i^n}{\Delta t} + s_i \\ \equiv \left(R_i^{n+1,m} \right) \text{MPFD} \text{MPFD}, \end{aligned} \quad (12)$$

where the notation $R_i^{n+1,m}$ is kept for consistency with Celia et al. (1990). The system of equations described by Equation 12 forms a tri-diagonal matrix. As in Wever et al. (2014), the function `DGTSV` from the `LAPACK` library (Anderson et al., 1999) is called to compute the solution. When `LAPACK` is not available, or not selected on compile time, the Thomas algorithm is used as the implemented default alternative, which does not depend on external libraries. However the Thomas algorithm is not the preferred option as in contrast to `DGTSV`, it lacks partial pivoting and may suffer from numerical instabilities.

Salinity

2.2.2 Transport Equation for Salinity

The governing equation in 1-dimension for concentration describes the change in salinity as a combination of a diffusion and advection process:

$$5 \quad \frac{\partial}{\partial t} (\theta S_b) - \frac{\partial}{\partial z} \left(D \theta \frac{\partial S_b}{\partial z} \right) - \frac{\partial}{\partial z} (q S_b) - s_{sb} = 0 \quad (13)$$

Where D is the diffusion coefficient ($\text{m}^2 \text{ s}^{-1}$), considered here as a first approximation independent of temperature, taken. In this study, D is set as $10^{-10} \text{ m}^2 \text{ s}^{-1}$ (Poisson and Papa, 1983). q denotes the liquid water flux (m s^{-1}) and s_{sb} is a source/sink term for salinity (assumed here to be $0 \text{ g kg}^{-1} \text{ s}^{-1}$).

An implicit numerical scheme for Equation 13 becomes in discretized form (n and i again denoting time and spatial level, respectively):

$$15 \quad \begin{aligned} & \frac{\left(\theta_i^{n+1} S_{b,i}^{n+1} - \theta_i^n S_{b,i}^n \right)}{\Delta t} \\ & - f \left[\left(\frac{2D_{i+1}^n \theta_{i+1}^{n+1} S_{b,i+1}^{n+1}}{\Delta z_{\text{up}} (\Delta z_{\text{up}} + \Delta z_{\text{down}})} - \frac{2D_i^n \theta_i^{n+1} S_{b,i}^{n+1}}{(\Delta z_{\text{up}} \Delta z_{\text{down}})} + \frac{2D_{i-1}^n \theta_{i-1}^{n+1} S_{b,i-1}^{n+1}}{\Delta z_{\text{down}} (\Delta z_{\text{up}} + \Delta z_{\text{down}})} \right) \right] \\ & - (1-f) \left[\left(\frac{2D_{i+1}^n \theta_{i+1}^n S_{b,i+1}^n}{\Delta z_{\text{up}} (\Delta z_{\text{up}} + \Delta z_{\text{down}})} - \frac{2D_i^n \theta_i^n S_{b,i}^n}{(\Delta z_{\text{up}} \Delta z_{\text{down}})} + \frac{2D_{i-1}^n \theta_{i-1}^n S_{b,i-1}^n}{\Delta z_{\text{down}} (\Delta z_{\text{up}} + \Delta z_{\text{down}})} \right) \right] \\ & - f \left[\left(\frac{q_{i+1}^n S_{b,i+1}^{n+1} - q_{i-1}^n S_{b,i-1}^{n+1}}{(\Delta z_{\text{up}} + \Delta z_{\text{down}})} \right) \right] - (1-f) \left[\left(\frac{q_{i+1}^n S_{b,i+1}^n - q_{i-1}^n S_{b,i-1}^n}{(\Delta z_{\text{up}} + \Delta z_{\text{down}})} \right) \right] - s_{sb} = 0 \quad (14) \end{aligned}$$

Here, taking $f = 1$ results in a fully implicit scheme, whereas taking $f = 0.5$ corresponds to the Crank-Nicolson scheme (Crank and Nicolson, 1996). The equation is solved after every time step for liquid water flow, assuming that the water flux q is constant with time and can be referenced with the time level n . Furthermore, for LWC θ , both θ^n , as well as θ^{n+1} are known from solving Eq. 12. Furthermore, it is assumed that the water flux q is constant with time and can be referenced with the time level n . The liquid water flux is directly obtained from the Darcy-Buckingham law (Buckingham, 1907), which forms the basis of Richards equation:

$$25 \quad (\Delta z_{\text{up}})^2 + \cos(\gamma) K_{i+1/2} + \cos(\gamma) \frac{K_{i+1/2}}{\rho_{i+1/2}} z_{i+1/2} \left(\frac{\rho_{i+1} - \rho_i}{\Delta z_{\text{up}}} \right), \quad (15)$$

and

$$\underline{(\Delta z_{\text{down}})^2} + \cos(\gamma) K_{i-1/2} + \cos(\gamma) \frac{K_{i-1/2}}{\rho_{i-1/2}} z_{i-1/2} \left(\frac{\rho_i - \rho_{i-1}}{\Delta z_{\text{down}}} \right).$$

(16)

5

The domain in SNOWPACK is typically nonuniform and the spatial discretizations in Eq. 14 for the a nonuniform grid are based on Veldman and Rinzema (1992). The system of equations described by Equation 14 forms a tri-diagonal matrix, similar to and solved in the same way as the equation for liquid water flow (Eq. 12).

SNOWPACK by default uses the Crank-Nicolson scheme. The fully implicit scheme is only first order accurate, whereas the 10 Crank-Nicolson scheme is second order accurate. Both schemes are unconditionally stable and suffer only minimal numerical diffusion for advection. As with many other common schemes, the advection part does not perfectly conserve sharp transitions. The Crank Nicolson scheme is, in spite of being unconditionally stable, prone to spurious oscillations in the solution. To choose adequate time steps, w apply the CFL condition we apply the Courant-Friedrichs-Lowy (CFL) condition (Courant et al., 1928) , typically required for stability of an explicit scheme, also for the Crank-Nicolson scheme:

$$15 \quad q \frac{\Delta t}{\Delta z} \leq 1 \quad (17)$$

Note that if the CFL condition is violated, the time step is reduced and the last time step for the Richards equation is also repeated with the reduced time step.

Boundary Conditions

2.2.3 Boundary Conditions

20 The boundary conditions for the Richards equation (Eq. 3) are determined by a Neumann boundary condition at the top, consisting of the top water flux from rain, evaporation or condensation and a Dirichlet boundary condition at the bottom by prescribing the bottom pressure head. The pressure head at the bottom of the sea ice corresponds to the water pressure at that depth, which equals the sea level (in the model domain (z_{sl} , m). This is determined from the isostatic balance:

$$\underline{\text{SWE}(\rho_w + \beta S_o)},$$

25

(18)

where S_o is the ocean water salinity (g kg^{-1}) and SWE is the snow water equivalent, defined as the sum over all elements N of the mass of each element j in the model:

$$\text{SWE} = \sum_{j=1}^N (\theta_{i,j} \rho_i + \theta_j \rho_j) \Delta z_j, \quad (19)$$

5 where $\theta_{i,j}$ and θ_j are the volumetric content ($\text{m}^3 \text{ m}^{-3}$) for layer j of ice and water, respectively. ρ_i is the density of freshwater ice (917 kg m^{-3}) and ρ_j the brine density of layer j (see Eq. 485).

The boundary conditions for the advection terms of the advection-diffusion equation (Eq. 13) are prescribed as a Neumann boundary condition, with fresh water at the top, and ocean salinity at the bottom. Only in case of an outgoing water flux at the top of the domain (evaporation), a zero-flux condition for salinity is used (i.e., salt will remain in the sea ice or snow with 10 evaporation).

For the diffusion terms in Eq. 13, we implemented a no-flux boundary conditions. These are condition at the top of the domain. This implies that there is no diffusion of salt with the atmosphere. This boundary condition is derived by considering the central differences scheme for the diffusion term on a nonuniform grid, determined according to:

$$\frac{\partial^2}{\partial z^2} (D\theta S_b) \approx \frac{\frac{\partial D\theta S_b}{\partial z} \Big|_{z_{i+1/2}} - \frac{\partial D\theta S_b}{\partial z} \Big|_{z_{i-1/2}}}{z_{i+1/2} - z_{i-1/2}} \approx \frac{\frac{D_{i+1}\theta_{i+1}S_{b,i+1} - D_i\theta_iS_{b,i}}{z_{\text{up}}} - \frac{D_i\theta_iS_{b,i} - D_{i-1}\theta_{i-1}S_{b,i-1}}{z_{\text{down}}}}{\frac{1}{2}(z_{\text{up}} + z_{\text{down}})} \quad (20)$$

15 A In general, a no-flux boundary condition can be achieved by forcing gradients over the boundaries to be 0, such that either the left (upper boundary) or right (lower boundary) term in the numerator of Eq. 20 vanishes.

Hydraulic Properties

We only apply the no-flux boundary at the top. For the bottom boundary condition at $i = 0$, diffusion is calculated by assuming:

$$20 \quad S_{b,i}^n = S_{b,i}^{n+1} = S_o. \quad (21)$$

2.2.4 Hydraulic Properties

For solving the Richards equation and the salinity transport equation, several parameters which depend on the snow and ice microstructure need to be specified. For saturated hydraulic conductivity (K_{sat}), we define elements with a porosity (i.e., $1 - \theta_i$) larger than 0.25 as snow, and smaller than 0.25 as ice.

For snow elements, a formulation based on Calonne et al. (2012) is typically used (see Wever et al. (2014)):

$$K_{\text{sat}} = \left(\frac{\rho g}{\mu} \right) \left[3.0 \left(\frac{r_{\text{es}}}{1000} \right)^2 \exp(-0.013\theta_i \rho_i) \right], \quad (22)$$

where r_{es} is the equivalent sphere radius (m). Note that Eq. 14 in Wever et al. (2014) erroneously shows a factor 0.75 (which corresponds to r_{es} being a grain diameter) instead of 3.0.

5 For sea ice, the saturated hydraulic conductivity (K_{sat}) is based on Golden et al. (2007):

$$K_{\text{sat}} = 3 \cdot 10^{-8} \left(\frac{\rho g}{\mu} \right) (1 - \theta_i)^3 \quad (23)$$

In unsaturated conditions, the van Genuchten-Mualem model (Mualem, 1976) is used to relate the hydraulic conductivity in saturated conditions (Eq. 22 and 23) to unsaturated conditions. For averaging the hydraulic conductivity between elements, we use the geometric mean (Wever et al., 2015), which is the preferred method (Haverkamp and Vauclin, 1979; Celia et al., 1990)

10 Furthermore, in unsaturated conditions, the van Genuchten model is used for the water retention curve, which describes the relationship between capillary suction and LWC (van Genuchten, 1980). The coefficients in this parameterization of water retention in snow is based on the work by Yamaguchi et al. (2012) ~~for snow~~. We extend this parameterization independent of porosity, by absence of any information of water retention in sea ice as a function of salinity and LWC. It has a relatively small impact, as the largest part of the sea ice is below sea level and ~~thus saturated the model typically simulates saturated conditions~~

15 here.

3 Data and Simulation Setup

3.1 In-situ Buoys

We apply the sea ice version of SNOWPACK to snow and sea ice properties measured from two ~~pairs of Snow Buoys~~ Snow Buoys (Nicolaus et al., 2017) and one Ice Mass-balance Buoy (IMB) in the Weddell Sea, Antarctica. Snow Buoys are autonomous ice tethered instruments, which measure snow surface changes/accumulation with four ultrasonic sensors at approximately 1.5 m above the snow/ice interface (Nicolaus et al., in prep). We construct a time series by averaging the four snow-depth ultrasonic sensors of each buoy, creating a time series of the surface elevation referenced to the initial snow/ice interface upon installation of the buoy. In addition to snow-depth the surface elevation, the Snow Buoys measure barometric air pressure and air temperature.

25 Each IMB consists of a 4.8 m long thermistor string chain, with a vertical sensor spacing of 0.02 m and provides sea ice temperature as well as interfaces from snow, sea ice, and sea water. The instruments are described by Jackson et al. (2013). It turned out to be good practice to co-deploy Snow Buoys and thermistor string chain IMBs in order to observe snow depth and sea ice properties at the same time. The full data set of all these Lagrangian observations is available from <http://www.meereisportal.de> (Grosfeld et al., 2015).

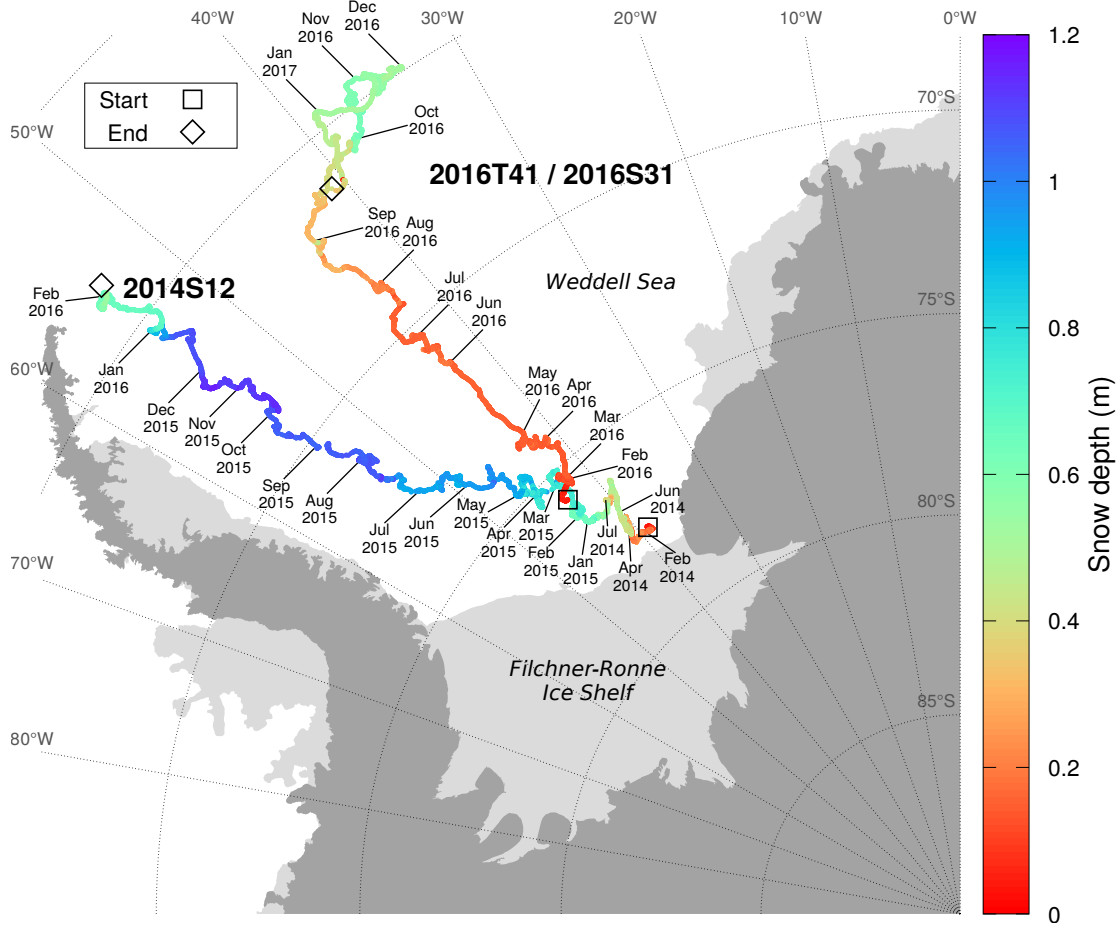


Figure 1. Trajectories of the two sea ice snow buoys used for the simulations. The average snow depth measured by the four snow depth sensors on each Snow Buoy is shown in color. The location Labels show the position of the buoys respective Snow Buoy on the 1st day of each month is labelled by the month and year. The collocated IMB For buoy for the 2014S12 Snow Buoy (2014T9) stopped transmitting data very soon and is ignored in some labels at the analysis. The collocated IMB buoy to Snow Buoy 2016S31 is 2016T41 beginning have been omitted for readability. The deployment location (start) is denoted by a square, the location of the last received data from the buoy (end) is denoted by a diamond. The collocated IMB buoy for the 2014S12 Snow Buoy (2014T9) stopped transmitting data shortly after installation and is ignored in the analysis. The collocated IMB buoy to Snow Buoy 2016S31 is 2016T41.

The two selected Snow Buoys (Snow Buoys 2014S12 ([Nicolaus and Schwegmann, 2017](#)) and 2016S31 ([Arndt et al., 2017](#))) have long time series and cover different trajectories, as shown in Fig. 1. Unfortunately, IMB 2014T9 collocated with Snow Buoy 2014S12 stopped transmitting data soon after deployment. IMB 2016T41, collocated with Snow Buoy 2016S31 measured for almost the same period as the Snow Buoy. However, comparisons have to focus on are limited to the sea ice properties

~~temperature and ice thickness~~, excluding the snow cover on top, because the IMB was deployed directly onto the ~~sea-ice surface~~ and ~~snow surface~~, without room to accommodate for snow accumulations after installation. Thus, the thermistor chain does not measure the snow cover properties, except for the lowest few cm.

Fig. 1 shows the trajectories with labels marking the location at the 1st of each month. Snow Buoy 2014S12 was deployed 5 on 17 Jan 2014 and remained in the same area very close to the Filchner-Ronne Ice Shelf for the first year. From February 2015 onward, the Snow Buoy drifted northward parallel to the Antarctic Peninsula until data transmission was lost on 1 Feb 2016. During the last 18 hours no valid snow depth data were transmitted and the drift speeds were relatively high, suggesting that it is not a transmission or data logger failure, but rather an indication that flow deformation or breakup is the likely cause of the 10 loss of the Snow Buoy. We consider this particular Snow Buoy due to its long time span, even though a collocated IMB data set is not available.

Snow Buoy 2016S31, collocated with IMB Buoy 2016T41, was deployed on 16 Jan 2016. This deployment ~~first~~ drifted on a ~~northward course until December 2016~~, ~~predominantly northward course~~. Around the 1st of December, the northernmost position was reached ~~after which and~~ the deployment drifted southward again. The Snow Buoy transmitted data ~~up to until~~ 15 Jan 2017, 2:00 UTC, shortly before the last data transmission by the IMB Buoy (5 Feb 2017, 07:13 UTC). This combination 15 of Snow Buoy and IMB Buoy is interesting for the long time span of collocated measurements.

3.2 Initial Conditions

To start each simulation, a description of the initial sea ice state is required. Upon installation of each Snow Buoy, the ice thickness, snow thickness and freeboard ~~was were~~ determined. For simulations of these Snow Buoys, we distinguish three categories: (i) sea ice below sea level (ice thickness minus freeboard), (ii) sea ice above sea level (freeboard) and (iii) snow.

20 For the part of the sea ice below sea level, the volumetric ice content θ_i was fixed to ~~0.90.95~~, and the volumetric water content θ_w was subsequently calculated as:

$$\theta_w = (1 - \theta_i) \frac{\rho_i}{\rho_w} \quad (24)$$

This formulation leaves a small volumetric air content which can be filled when water refreezes and thereby expands. This is currently required for the stability of the numerical schemes in the SNOWPACK model, but in reality refreezing water 25 would increase the pressure in the brine. The element temperature was initialized by the value recorded by the IMB upon installation. As it takes time for the thermistor ~~string chain~~ to freeze into the ice and adapt to the surrounding ice temperature, this temperature is mostly representative of the ocean water. The brine salinity was set as the salinity for which the melting point corresponds to the measured temperatures.

For the part of sea ice above sea level, the volumetric ice content θ_i was also fixed to ~~0.90.95~~, but the remaining space 30 was assigned to air content and the bulk salinity was set to 0 g kg^{-1} . ~~Snow~~ In field studies, it was found that brine may exist above sea level, due to capillary wicking, or brine content is retained because of low conductivity in the brine channels (e.g., Cox and Weeks, 1974; Massom et al., 2001).

The initial snow layer was 10 cm for Snow Buoy 2014S12 and 2 cm for 2016S31. The snow cover was initialized with a density of 275 kg m^{-3} , and a grain size of 0.15 mm. The grain shape was initialized as depth hoar with a sphericity and dendricity of 0. As the majority of the snowpack builds during the model simulations, the simulations are rather insensitive to the choice of initial snowpack properties. The element temperature was derived from the thermistor string chain measurements.

5 Finally, the depth of each element was set to 0.02 m.

3.3 Forcing Data

Simulations with the SNOWPACK model require air temperature, relative humidity, incoming shortwave radiation, incoming longwave radiation, wind speed and precipitation. Here, we used ERA5 (European Centre for Medium-range Weather Forecasts ECMWF Reanalysis 5) data to provide these parameters to drive the simulations. For each timestep and location, the simulated 10 weather at the closest grid point in the ERA5 model was taken.

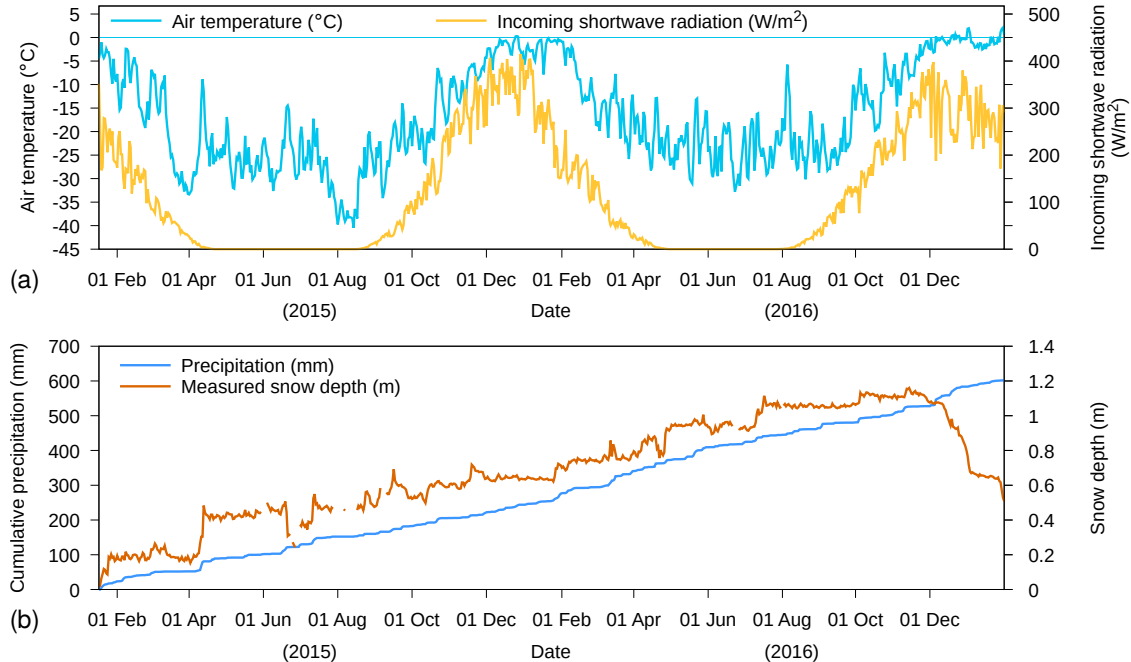


Figure 2. Meteorological forcing data from ERA5 for Snow Buoy 2014S12 for (a) daily average air temperature and daily average incoming shortwave radiation, and (b) cumulative precipitation. In (b), also measured snow depth by the buoy is shown.

Fig. 2 shows the daily average air temperature, incoming shortwave radiation and cumulative precipitation from the ERA5 forcing for Snow Buoy 2014S12. Additionally, the measured snow depth by the buoy is shown. We find that the daily average air temperature was mostly below 0°C , reaching -40°C in 2015. Near the end of the time series, when the Snow Buoy stopped transmitting data, daily average air temperature varied around 0°C . It can be expected that positive temperatures

5 during midday is associated with enhanced snow melt, which is indicated by the rapid decrease of measured snow depth starting from December 2016 onward. During austral winter 2015 and 2016, the Snow Buoy was located below the polar circle and consequently, there was no incoming shortwave radiation. In austral summer 2016/2017, the Snow Buoy drifted above the polar circle. Nevertheless, the average incoming shortwave radiation in the first austral summer is similar to the second austral summer. The cumulative precipitation from ERA5 reached around 600 mm for the almost two years that the buoy was operative. The buoy recorded 1.2 m of snow accumulation. A marked increase in snow depth around April 1, 2015 is accompanied by only a relatively small precipitation event. Except for this event, both the snow depth as well as the cumulative precipitation show a gradual increase over the two years until the melt phase starts.

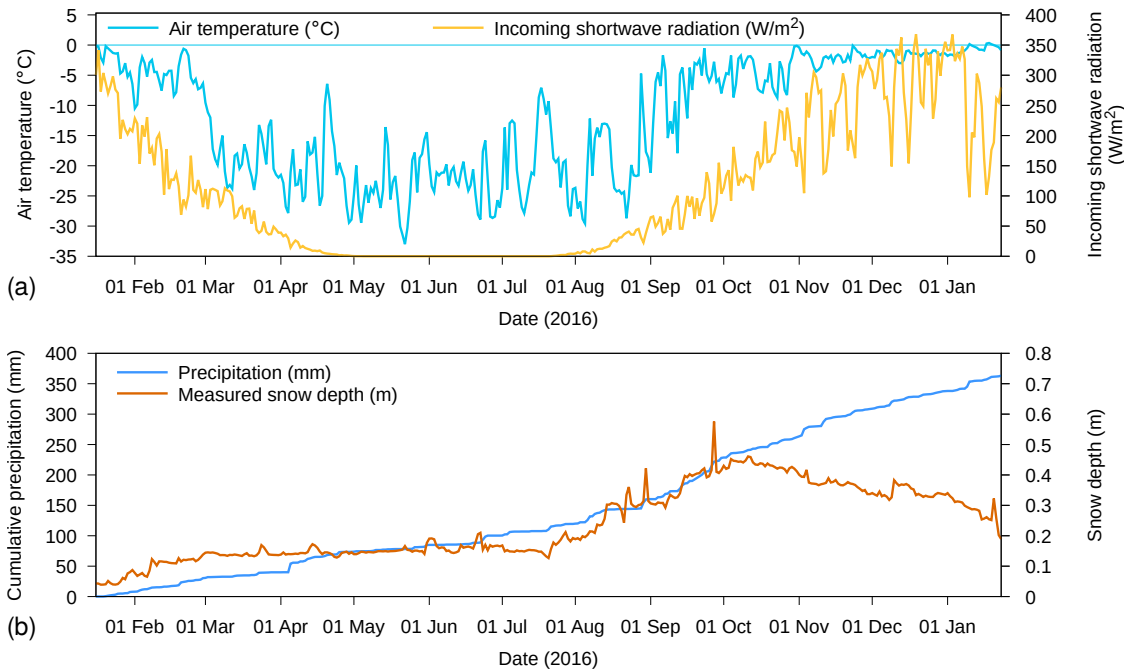


Figure 3. Meteorological forcing data from ERA5 for Snow Buoy 2016S31 for (a) daily average air temperature and daily average incoming shortwave radiation, and (b) cumulative precipitation. In (b), also measured snow depth by the buoy is shown.

10 Fig. 3 shows the daily average air temperature, incoming shortwave radiation and cumulative precipitation from the ERA5 forcing for Snow Buoy 2016S31. The yearly cycle in air temperature is similar to the year 2016 for Snow Buoy 2014S12, with daily air temperatures reaching around -30°C in austral winter. In austral summer, air temperatures around 0°C suggest melting conditions, particularly from November 2016 to January 2017. This is reflected by the decrease in snow depth for this period. The Snow Buoy was also located south of the polar circle, resulting in the absence of shortwave radiation during austral winter. The precipitation sum for the year that the Snow Buoy was operative amounted to 350 mm. The snow depth does not 15 change between March and July 2016, and shows an increase between August and October, after which a decrease occurs. The

cumulative precipitation show a similar pattern, with low precipitation between March and July, followed by a steady increase afterwards. Only during the melt phase, the increase in cumulative precipitation is not reflected by an increase in snow depth.

SNOWPACK has the possibility to either use a precipitation time series as input to determine when snow fall occurs, or to use a time series of snow depth to interpret increases in measured snow depth as snow fall events when simulated snow

5 depth is ~~below less than the~~ measured snow depth (Lehning et al., 1999). Note that there is no downward correction when the measured snow depth is below the simulated snow depth (in case of melt, surface sublimation, snow erosion, etc.). In order to use the ~~latter~~ snow depth driven method for the Snow Buoys and base the mass balance on Snow Buoy data, a layer can be marked in the simulations and tracked throughout the snow – sea ice continuum. By marking the layer that corresponds to the reference level for the snow depth measurements, the measured snow depth can be tracked relative to this marked layer. The
10 output routines of the model have been adapted accordingly to reference the output to either the sea level, or to the marked reference layer.

The ocean heat flux determines the ice mass balance at the bottom of the ice. Its value can be highly variable and dependent on ocean conditions below the sea ice (Ackley et al., 2015). From that study, we use a value of 8 W m^{-2} , unless otherwise noted.

15 4 Results

4.1 ~~Explicit Brine Dynamics~~ Example [Simulation](#)

Fig. 4 shows an example of model behaviour when an initially dry and fresh ice layer with a thickness of 1.58 m, consisting of 94% ice and 6% air expressed as volumetric content, is positioned in ocean water with a salinity of 35 g kg^{-1} . The positive pressure head at the bottom of the sea ice corresponds with the pressure exerted by the displaced water. As a consequence,

20 saline water enters the ice matrix (Fig. 4a,c), until it is in equilibrium with the sea level. The initial rate follows the saturated hydraulic conductivity for sea ice with a pore space of 6%, which is $3.55 \times 10^{-5} \text{ m s}^{-1}$ (Eq. 23).

As the pressure difference of the liquid water inside the ice matrix and the surrounding ocean water is decreasing, the salt influx rate decreases over time (Fig. 4e). The brine salinity corresponds to the brine salinity of ocean water (35 g kg^{-1} , see Fig. 4d), corresponding to a bulk salinity of 1.65 g kg^{-1} (see Fig. 4c). The added mass to the sea ice (Fig. 4b) causes the ice to
25 sink deeper inside the ocean water, decreasing the freeboard (Fig. 4f).

This example illustrates that the Crank-Nicolson scheme does not preserve the sharp transition in salinity, as both the bulk (Fig. 4c) as well as the brine (Fig. 4d) salinity shows smoothing behaviour at the saline water front. This reduces the pore space by refreezing to adapt to the thermal conductivity, reducing the saturated hydraulic conductivity in the wetting front region.

4.2 ~~Temperature validation~~ Validation

30 Fig. 5a and 5b show the simulated temperature of the snow–sea ice system for simulations driven by in-situ measured snow depth and ERA5 precipitation, respectively. Dashed lines denote the reference level, i.e., the snow–sea ice interface as deter-

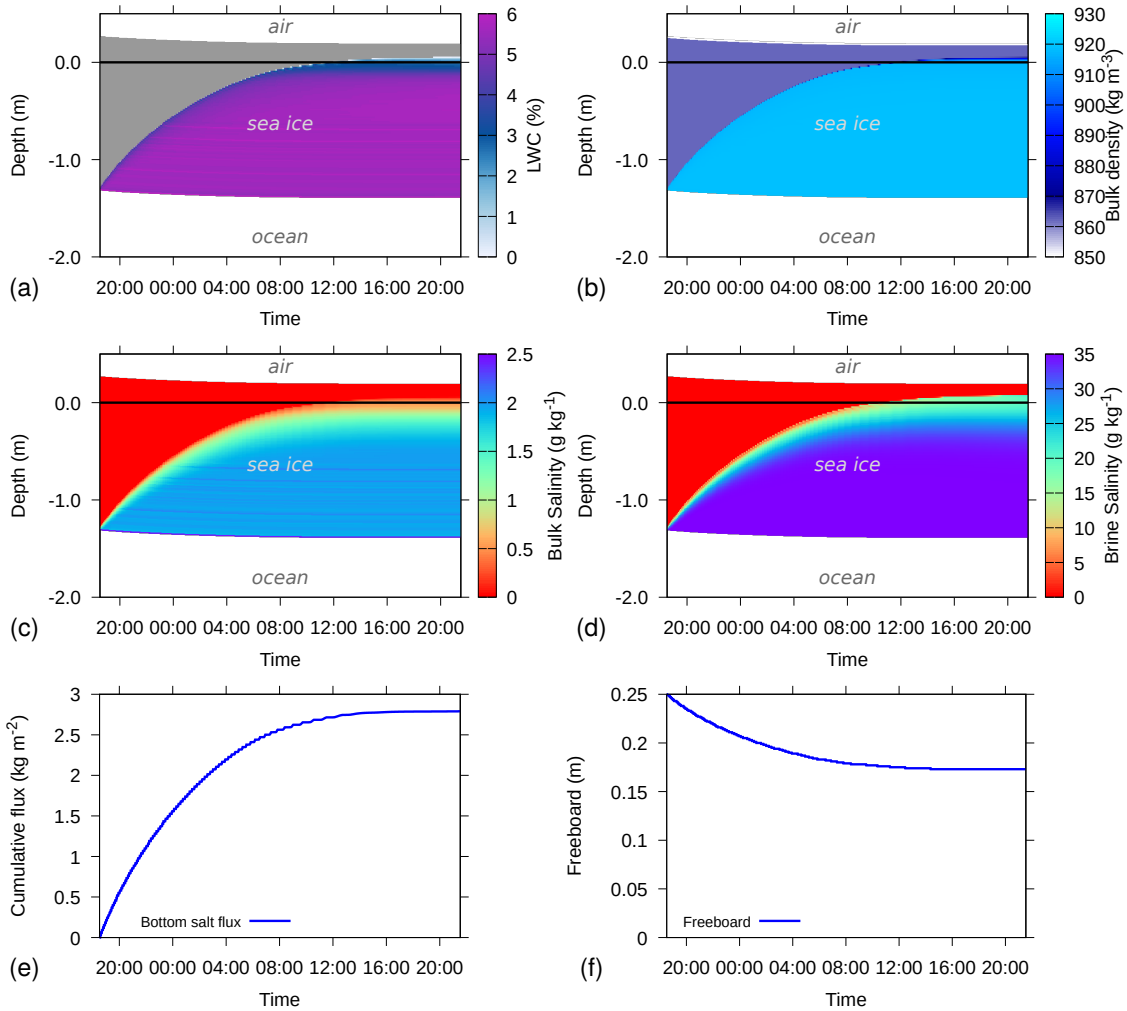


Figure 4. Example simulation where initially dry sea-porous freshwater ice with 94% volumetric ice content is placed into ocean water with a salinity of 35 g kg^{-1} . Shown are (a) liquid water content (LWC), (b) bulk density, (c) bulk salinity, (d) brine salinity, (e) cumulative salt flux at the bottom of the sea ice and (f) freeboard. In (a), dry snow is parts of the ice are colored grey. In (a), (b), (c), and (d), the depth on the y-axis is relative to sea level, i.e., sea level is 0 and indicated by the solid black line.

mined upon installation of the Snow Buoy. The sea level as calculated from hydrostatic balance is indicated by the solid line. The For the snow depth driven simulations, the sea level stays below the snow-sea ice interface, i.e., indicating that freeboard is positive in the simulations during the whole simulation period. However, for the precipitation driven simulations, there is more snowfall, which causes negative freeboard from October onward.

Fig. 5c shows the measured sea ice temperatures from the corresponding IMB. Note that for this IMB, the thermistor string chain does not extend above the initial 2 cm snow layer on top of the sea ice, such that the time evolution of the snow cover

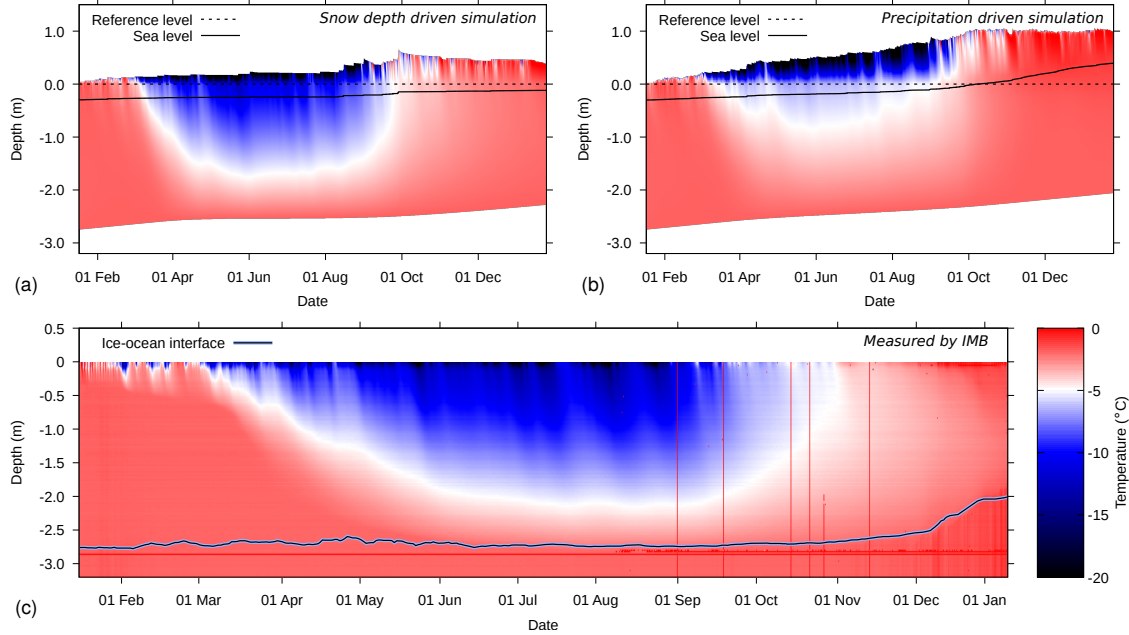


Figure 5. Snow and ice temperatures for Snow Buoy 2016S31 / IMB 2016T41, in for (a) simulations driven by in-situ measured snow depth, (b) simulations driven by ERA5 precipitation, and (c) measured temperatures by the IMB and (d) the difference between simulated (driven by snow depth) and measured temperatures. The depth on the y-axis is defined relative to the sea ice-snow interface, as determined upon installation (dashed line). The In (a) and (b), the solid line denotes the simulated-sea level as determined by the simulations. In (c), the blue/black line denotes the ocean/sea ice interface, as determined for the IMB.

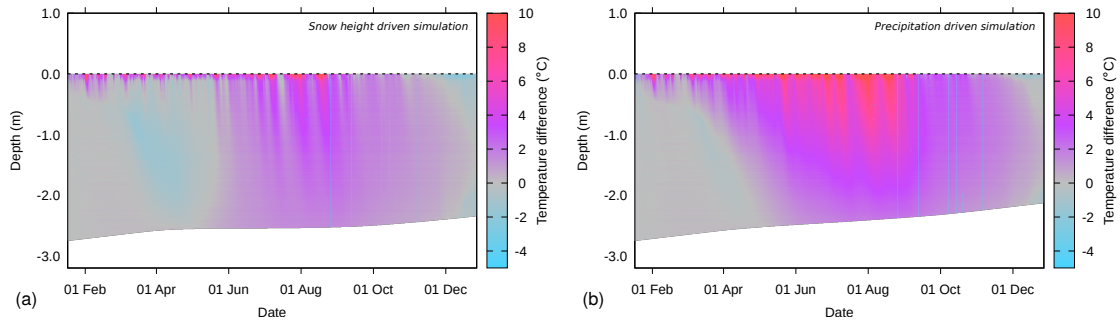


Figure 6. Difference between simulated and measured snow and ice temperatures for Snow Buoy 2016S31 / IMB 2016T41, for (a) simulations driven by in-situ measured snow depth, (b) simulations driven by ERA5 precipitation. The depth on the y-axis is defined relative to the sea ice-snow interface, as determined upon installation.

is not recorded by the IMB. We find that the IMB confirms the strong cooling of the sea ice during the austral winter months,

as found in the simulations, as well as the near-surface warming to the melting point of fresh water shortly before the last transmission by the buoy.

Fig 5d shows the difference between measured temperatures and the simulated temperatures in the ice by 6 shows difference plots of measured ice temperatures and simulated ice temperatures. Fig 6a compares the snow depth driven simulations (i.e., Fig 5e-a minus Fig. 5a), with positive values denoting c) and Fig 6b compares the precipitation driven simulations (i.e., Fig 5b minus Fig. 5c). Positive values denote an overestimated temperature by the model and vice versa. Note that the bottom of the sea ice in the simulations is typically above the ice–ocean interface in the IMB data.

The comparison shows that in spring, the the period March to May, the snow depth driven simulation slightly underestimates the sea ice temperatures, which suggests an overestimation of the initial cooling of the sea ice during the austral wintermonths. 10 The model underestimates towards austral winter. Both simulations underestimate the lowest temperatures reached in winter by up to 6–10 $^{\circ}$ C near the snow–sea ice interface, which is located at the top of the thermistor string chain. Similarly, incidental cooling in near surface sea ice layers in February and March are also underestimated. This could on the one hand indicate an overestimation of the surface energy balance incoming energy or an underestimation of outgoing energy in the forcing data or by the model, but also by an underestimated new snow density, and thus. On the other hand, an underestimated (new) 15 snow density would result in an underestimated thermal conductivity, by the model and overestimated thermal insulation in the model, as thermal conductivity typically increases with increasing snow density. Heat from the sea ice part would then not be able to be effectively transported through the snowpack and exchanged with the atmosphere.

The simulations driven by ERA5 precipitation show about twice as much snow accumulating on the sea ice (Fig. 5b) compared to accumulations determined from the snow height measurements (Fig. 5a). Also the reanalysis provides precipitation 20 (and thus snow accumulating) in the austral winter time, which is not found in the snow depth time series. This is not necessary a bias in ERA5, because snow erosion by wind can keep the snow depth constant over extended periods of time. Due to this discrepancy, the total snow depth may be overestimated by the ERA5 input at the end of the simulation. Furthermore, the thick snow cover in the precipitation driven simulation better insulates the underlying ice, resulting in a stronger overestimation of ice temperatures compared to the snow height driven simulation.

25 The thermistor string chain is also used to determine the heat capacity by heating the string chain for 1 or 2 minutes and looking at analyzing the temperature response. By combining the absolute temperatures and the heating rates, the ice–ocean interface has been determined as manually determined and is shown in Fig. 5c. The IMB data confirm the modelling result that the strong negative energy balance at the top of the snow–sea ice system during austral winter has not resulted in an ice thickness increase. The warmer sea ice in the precipitation driven simulations resulted in a thinning of the ice by the ocean 30 heat flux, which is not confirmed by the IMB data. The decrease in ice thickness in December 2016 is not reproduced by the model either one of the simulation setups. The trajectory of the buoy shows a marked change in drift direction (Fig. 1), changing from a northward to a southward drifting course during this period. This change of direction may have been accompanied by an intrusion of warm ocean water below the sea ice and an increased ocean heat flux.

Fig. 5a and 5b show the simulation driven by in-situ snow depth measurements, and by precipitation time series from ERA5, 35 respectively. The in-situ measured snow depth on the Snow Buoys qualitatively shows a good agreement in terms of timing

of precipitation events and the general evolution of the snow cover on the sea ice. However, the ERA5 precipitation leads to accumulations in the austral winter time, that are not present in the snow depth time series. This is not necessary a bias in ERA5, because snow erosion by wind can keep the snow depth constant over extended periods of time. Due to this discrepancy, the total snow depth is slightly overestimated by the ERA5 input at the end of the simulation.

5 LWC, bulk and brine salinity, as well as the bottom salt flux for the simulations driven by measured snow depth are shown in Fig. 7. LWC (Fig. 7a) shows a strong reduction in austral winter due to the freezing brine. In December, occasional surface meltwater from the snow percolates down in the sea ice. Combined with rising temperatures, a high LWC layer forms around and just below, causing brine salinity to increase (Fig. 7c). The snow is dry most of the time, except towards the end of the simulation when meltwater percolates downward. Furthermore, we find a thin layer with low values of LWC just above sea

10 level. This is caused by capillary forces causing upward motion of sea water above sea level.

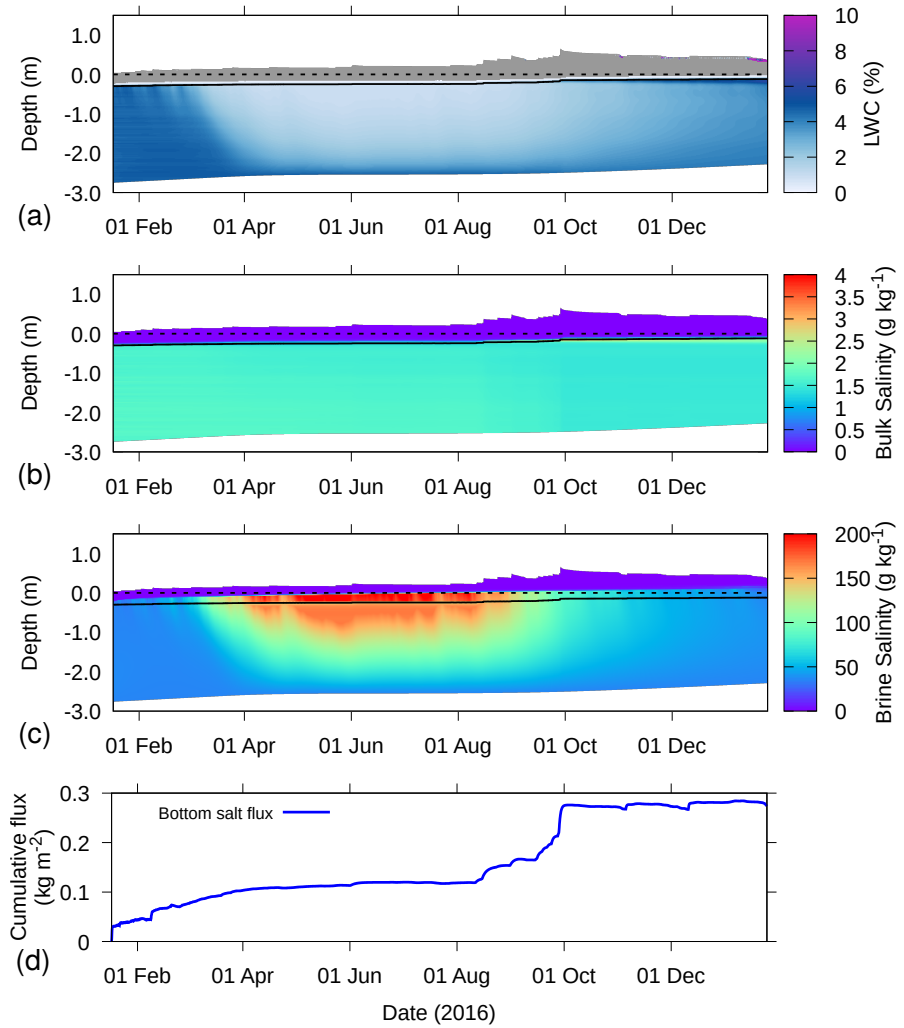
Fig. 7b shows that the bulk salinity of the sea ice hardly changes over the course of the simulation, whereas the brine salinity (Fig. 7c) clearly shows a relationship with the temperature. This reflects the prescribed thermal equilibrium between brine and the ice, assuming that the brine is at melting temperature. Fig. 7d shows that the added weight of snow accumulation the accumulating snow pushes the sea ice deeper into the ocean, increasing the pressure head at the bottom of the sea ice. 15 This leads to an influx of saline water, even though the sea level remains below the snow–ice interface. Combined with rising temperatures, a layer with increased bulk salinity and increased LWC forms around and just below sea level around the 1st of October.

4.3 Fixed Salinity Profiles

Example simulation for buoy 2016S31, where measured snow depth was used to derive the precipitation events, and the bulk 20 salinity profile was prescribed, for temperature (a), LWC (b) and bulk salinity (c). In (b), dry snow is colored grey. The depth on the y-axis is defined relative to the sea ice–snow interface, as determined upon installation (dashed line). The solid line denotes the sea level as determined by the simulations.

In Fig. ??, we show an example of a simulation with a prescribed, time-invariant salinity profile. The bulk salinity profile is fixed between the bottom and top of the sea ice, with a value of 12 g kg^{-1} . The vertical distribution of bulk salinity is then 25 prescribed by a sine function with an amplitude of 8 g kg^{-1} . The snow is assigned a constant salinity of 1 g kg^{-1} . The water transport is described by the bucket scheme, which is the only scheme that works with prescribed salinity profiles.

The salinity in snow causes the presence of some amount of liquid water in the snowpack, such that the brine salinity satisfies the melting point temperature. We also find that the high bulk salinity prescribed near the snow–ice interface requires high values of LWC to arrive at the brine salinity that would correspond to the ice temperatures. The latent heat required for melting 30 of ice to achieve this, results in lower temperatures of the sea ice. Overall, the simulations compare well to simulations with explicit salinity transport, in terms of ice thickness and temperature distributions.



Example simulation for Snow Buoy

2016S31, where measured snow depth was used to derive the precipitation events, for temperature (a), LWC (b), bulk salinity (c), brine salinity (d) and cumulative salt flux at the bottom of the sea ice (e). In (b), dry snow is colored grey. In (a), (b), and (c), the depth is defined relative to the sea ice-snow interface, as determined upon installation (dashed line). The solid line denotes the sea level as determined by the simulations. An increasing cumulative flux denotes inflow and vice versa.

Figure 7. Example simulation for Snow Buoy 2016S31, where measured snow depth was used to derive the precipitation events, for (a) LWC, (b) bulk salinity, (c) brine salinity and (d) cumulative salt flux at the bottom of the sea ice. In (a), dry parts of the snow – sea ice system are colored grey. In (a), (b), and (c), the depth is defined relative to the sea ice-snow interface, as determined upon installation (dashed line). The solid line denotes the sea level as determined by the simulation. In (d), an increasing cumulative flux denotes inflow and vice versa.

4.3 Flooding and Superimposed Ice Formation

Figs. 8 and 9 show an example simulation for Snow Buoy 2014S12. The simulations were driven by the snow depth measurements from the buoy. Upon installation of the buoy, the snow depth was referenced to the sea ice surface. This reference level is shown by the dashed line. Due to basal ice melt and growth, as well as additional snowfall, the simulated sea level became 5 higher w.r.t. to the snow depth sensor, as indicated by the solid line. This is congruent with a negative freeboard. It indicates that significant flooding occurred, as also evidenced by the LWC in Fig. 8b and associated high bulk salinity (Fig. 8c). Fig. 9a shows that the bulk density of the flooded part is similar to the underlying ice density, illustrating the depletion of pore space. Fig. 9b shows that much of the sea water that flooded flooding the snow refroze, adding substantial ice mass.

The simulated temperature (Fig. 8a) shows the two austral winters with low temperatures, and the two austral summers 10 with temperatures close to 0°C . Interestingly, the low temperatures in the first austral winter impacted the part below sea level stronger than the second austral winter, as demonstrated by the lower temperatures in that part of the domain. During the second austral winter, the flooding in the simulation increased the liquid water content of the snow and consequently, much of the energy loss by the sea ice in this period was balanced by the energy release from refreezing liquid water, rather than decreasing temperatures.

15 Fig. 8e shows that flooding also leads to a strong influx of salt to the snow-sea ice system. The flooding saturates the snow, which has significant pore space compared to the sea ice. Therefore, snowfall events of similar magnitude have different effects on the salt influx, depending on whether or not flooding occurs at the time.

Note that the flooding, as depicted in simulations with the Richards equation coupled to the transport equation, is governed by the hydraulic conductivity of ice. In cold ice, hydraulic conductivity can be so low that negative freeboard remains for extended 20 period of times, even without flooding. On the other hand, flooding may also be triggered by deformation and cracking of the sea ice, combined with lateral flow effects. However, Maksym and Jeffries (2000) have shown that the simpler assumption (i.e., negative freeboard will trigger flooding) can already yield satisfying results. In the model, the maximum ice contents is fixed to $0.99 \text{ m}^3 \text{ m}^{-3}$ and is typically lower, such that hydraulic conductivity is typically generally large enough for instantaneous flooding.

25 The brine salinity in Fig. 8d shows spurious oscillations. These originate from the lower boundary and could be caused by the strong transition of brine salinity to ocean salinity. Also, the oscillations are partly attributed to the maximum allowed ice contents of 99% in the simulations, as they occur in the same area. The exact numerical mechanism and a possible solution is unknown at the stage.

Figs. 9c and 9d show the snow microstructure as simulated by the model. Even though validation for this specific floe 30 is not possible, we find several features consistent with other field observations. For example, a wet slush layer (coloured red) at the interface between snow and ice is visible, triggered by capillary suction and flooding. This is also reported in Nicolaus et al. (2009) and Arndt and Paul (2018) for the same geographical region. Even though those field observations report the presence of depth hoar layers in snowpacks, particularly in deeper snowpacks (exceeding 30 cm), the simulations seem to

show more deep depth hoar layers (coloured blue). The field observations often report wind slabs or other hard layers in between depth hoar layers. Simulating those kind of layers is a well-known problem for snowpack models (Domine et al., 2019).

The grain size shown in 9d ranges from 2-2.5 cm in the depth hoar layers at the base of the snowpack to 0.5-1 cm near the top of the snowpack. These simulated grain sizes corresponds to the range of values reported by the field studies listed earlier 5 (1-5 mm), yet exact validation remains difficult.

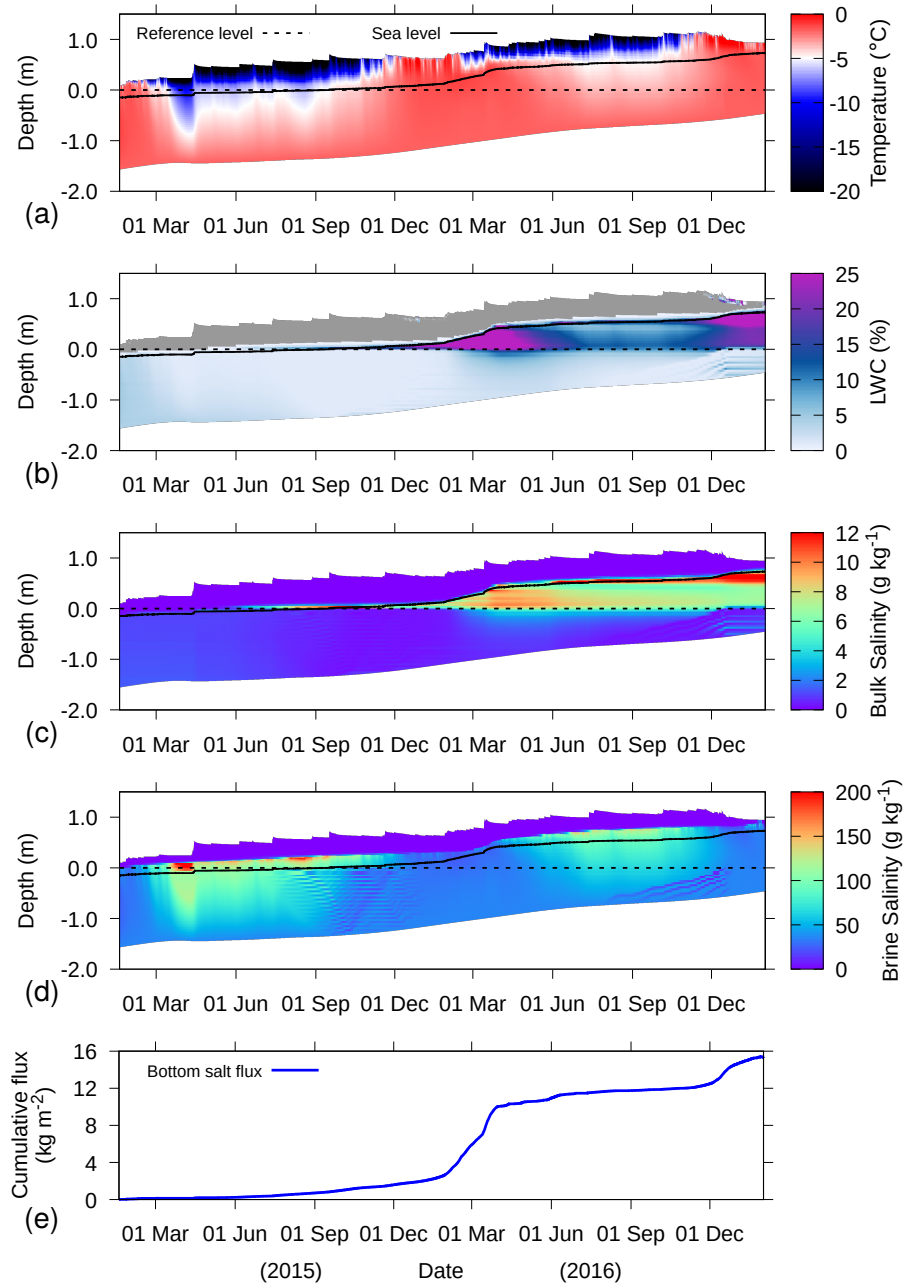


Figure 8. Example simulation for buoy 2014S12, where measured snow depth was used to derive the precipitation events, for temperature (a) temperature, LWC (b) LWC, bulk salinity (c), brine bulk salinity, (d) brine salinity and (e) cumulative salt flux at the bottom of the sea ice (e). In (b), dry parts of the snow is sea ice system are colored grey. In (a), (b), (c), and (d), the depth is defined relative to the sea ice-snow interface, as determined upon installation (dashed line). The solid line denotes the sea level as determined by the simulations simulation. An increasing cumulative flux denotes inflow and vice versa.

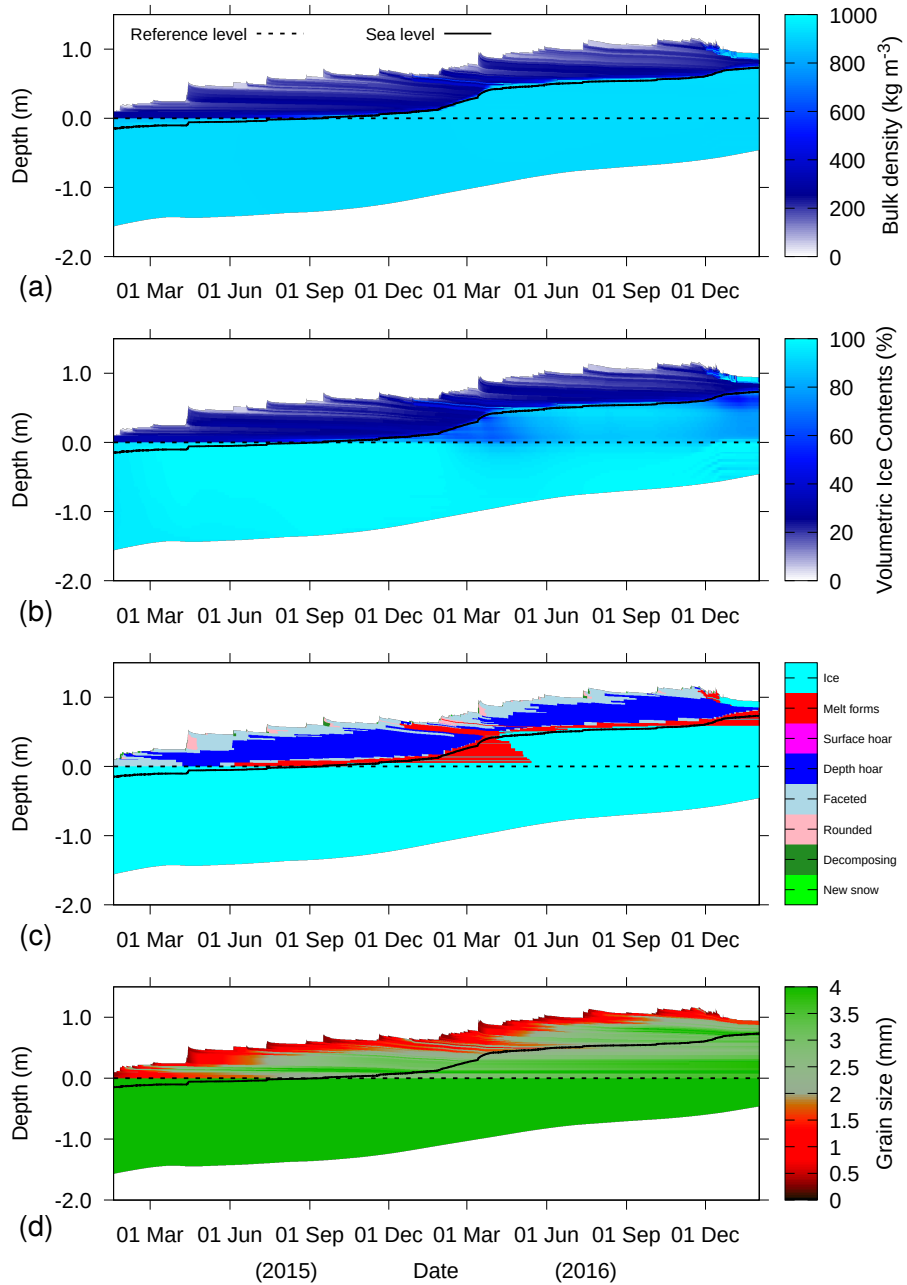


Figure 9. Example simulation for buoy 2014S12, where measured snow depth was used to derive the precipitation events, for (a) total bulk density, (b) volumetric ice content, (c) grain type and (d) grain size. The depth on the y-axis is defined relative to the sea ice-snow interface, as determined upon installation (dashed line). The solid line denotes the sea level as determined by the simulation.

4.4 Forced Warming and Cooling

Warming conditions increase the brine volume and the hydraulic conductivity of the sea ice, but also can cause freshwater percolation from snow melt. Similarly, cooling conditions decrease brine volume and increase brine salinity and density. When brine channels allow, the dense brine may drain from the sea ice.

5 We To test how our model simulations would react to continuous warming or cooling conditions, we used Snow Buoy 2016S31 for two experiments where we forced constant warming and constant cooling conditions by modifying the meteorological driving data starting April 1, 2016. For warming To force warming conditions, we prescribed a constant air temperature of +5 °C, a relative humidity of 80%, a wind speed of 3 m s⁻¹ and an incoming shortwave radiation of 300 W m⁻².

Fig. 10 and 11 show the warming example of simulation result for the warming experiment with buoy 2016S31. Fig. 10 shows that as soon as melting conditions were enforced (starting April 1st), the snowpack very quickly reached melting temperature. The fresh water percolating as a result from snow melt first starts started accumulating on below-freezing sea ice with low porosity (see Fig. 10b). This process is visible between April 14 and April 27 in April and leads to superimposed ice formation a thin layer of superimposed ice (Fig. 11b and 11c). Upon continued warming, fresh water starts Starting April 15, the bulk density of the snow – sea ice system was homogeneously around ice density, showing that the pore space has been depleted (11a).

The fresh water started flushing the ice around April 10, leading to a rapid reduction of bulk and brine salinity (Fig. 10c,d), due to the outflow of saline water at the bottom of the sea ice (Fig. 10e). When the brine decreases, water freezes and the permeability of the sea ice is low compared to the surface melt. We find that the meltwater accumulates on the top of the sea ice (Fig. 10b), which can be interpreted as the formation of a melt pond.

20 The sea ice thins continuously upon continued warming (Fig. 11b), until the ice has melted and the melt pond disappears. At this point, the simulations showed strong instabilities in the bottom salt flux, such that that the cumulative flux in Fig. 10e is only shown for the time period with ice below the liquid water. Note that the melt pond in the model consists of a little bit of ice (Fig. 11b), which results from the SNOWPACK numerics.

Fig. 12 shows an example where cooling conditions were enforced. Similar to the warming example, the meteorological 25 forcing conditions were replaced from April 1 onward by setting a constant air temperature of -30 °C, a wind speed of 1 m s⁻¹ and no incoming shortwave radiation. The ocean heat flux was set at 8 W m⁻². We find a consistent cooling and increase in brine salinity As soon as cooling conditions were present, a freezing front progressed through the sea ice. The interface between the sea ice and the ocean remained at the freezing point of ocean water, while the sea ice freezed and increased thickness.

With the decrease in temperature, brine salinity increased (Fig. 12d). This is achieved by freezing the liquid water, as shown 30 by the decrease in LWC (Fig. 12b). The bulk salinity remains approximately constant (Fig. 12e).

An increase in brine salinity also increases the density of the brine. This may lead to flushing of the sea ice, when the heavy brine moves downward and is replaced by lighter ocean water. However, in our simulations, there is only a very small outflow of salinity at the bottom ((Fig. 12e) and the bulk salinity remains approximately constant (Fig. 12c)). This result shows that

without a description of the convective processes in sea ice resulting from cooling (Griewank and Notz, 2013), the salinity depletion found due to cooling is strongly underestimated by this model approach.

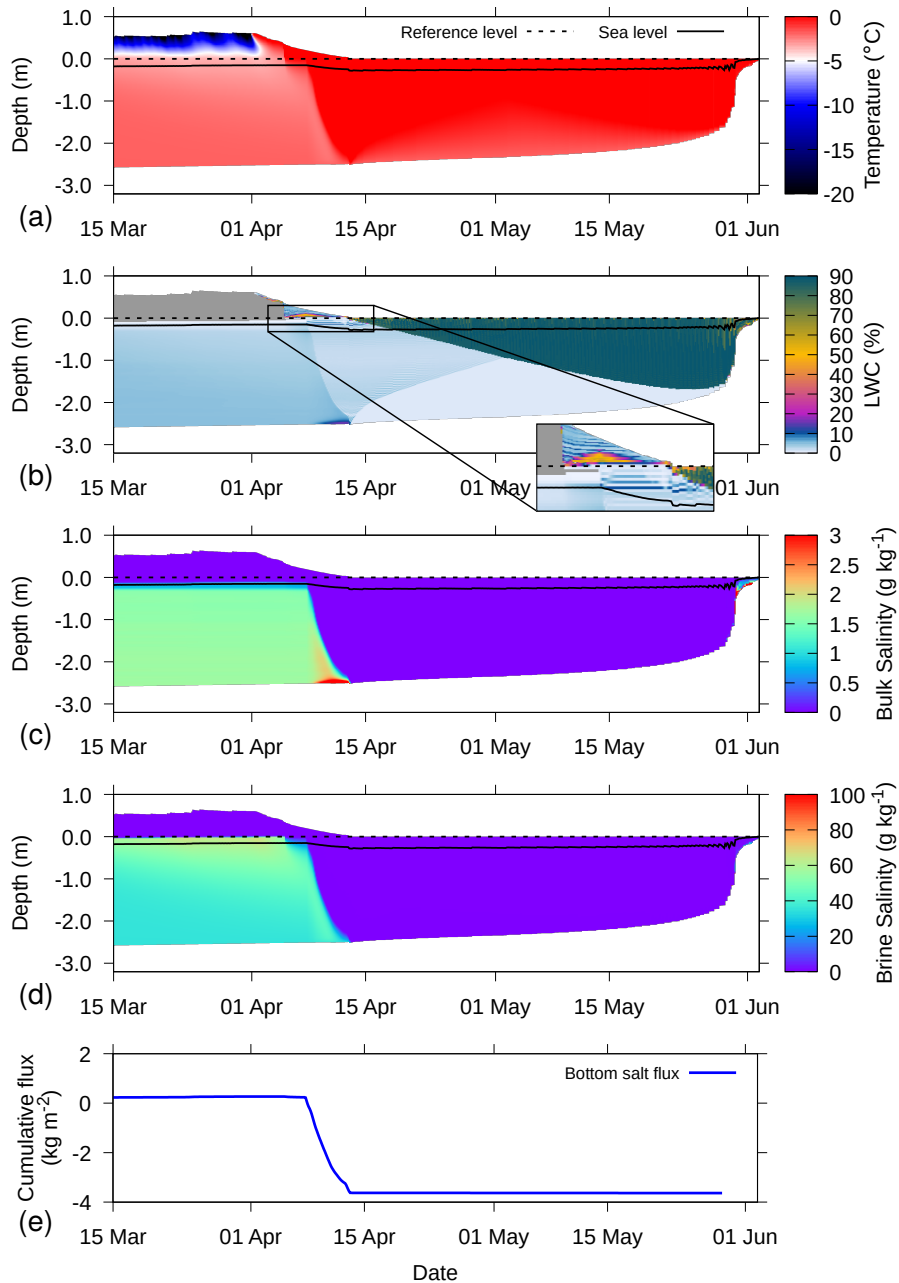


Figure 10. Simulation for 2016S31, where from April 1 onward, melting conditions are were enforced, for temperature (a) temperature, LWC (b) LWC, bulk salinity (c), brine bulk salinity, (d) brine salinity and (e) cumulative salt flux at the bottom of the sea ice (e). In (b), dry parts of the snow is sea ice system are colored grey. In (a), (b), (c), and (d), the depth on the y-axis is defined relative to the sea ice-snow interface, as determined upon installation (dashed line). The solid line denotes the sea level as determined by the simulations. An increasing cumulative flux denotes inflow and vice versa.

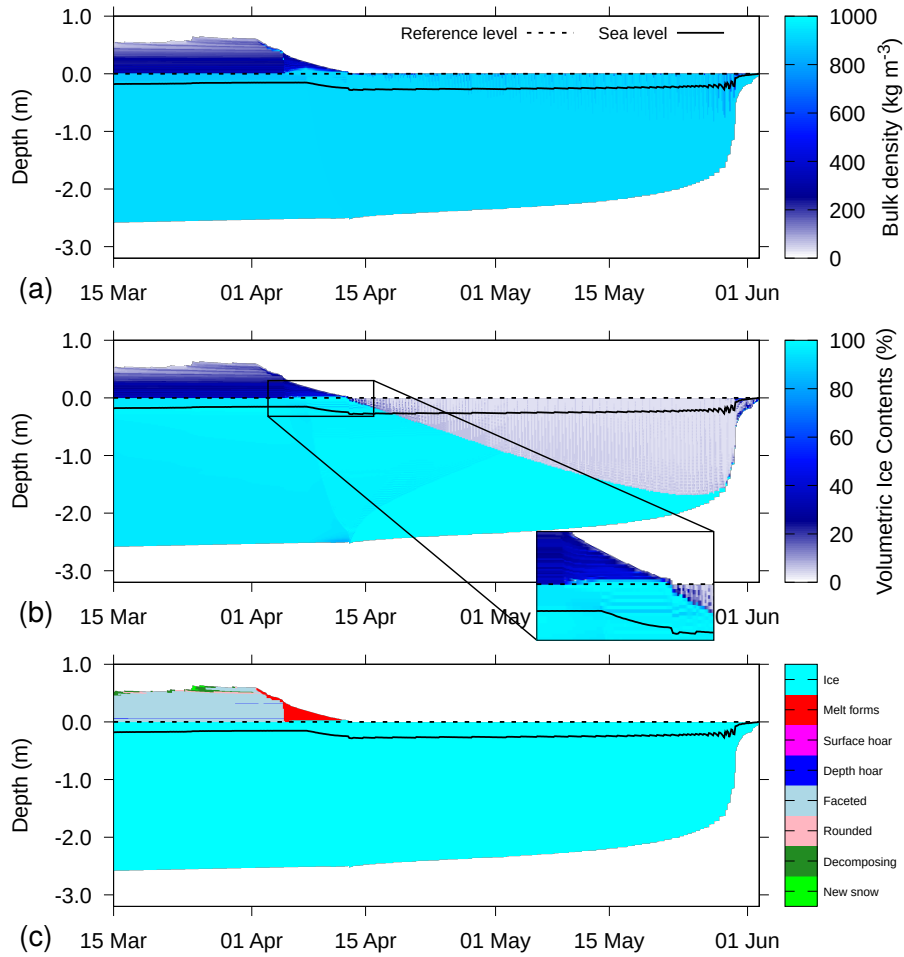


Figure 11. Simulation for 2016S31, where from April 1 onward, melting conditions ~~are~~ ~~were~~ enforced, for (a) total bulk density, (ab) volumetric ice content, (c) and grain type. The depth on the y-axis is defined relative to the sea ice-snow interface, as determined upon installation (dashed line). The solid line denotes the sea level as determined by the simulations.

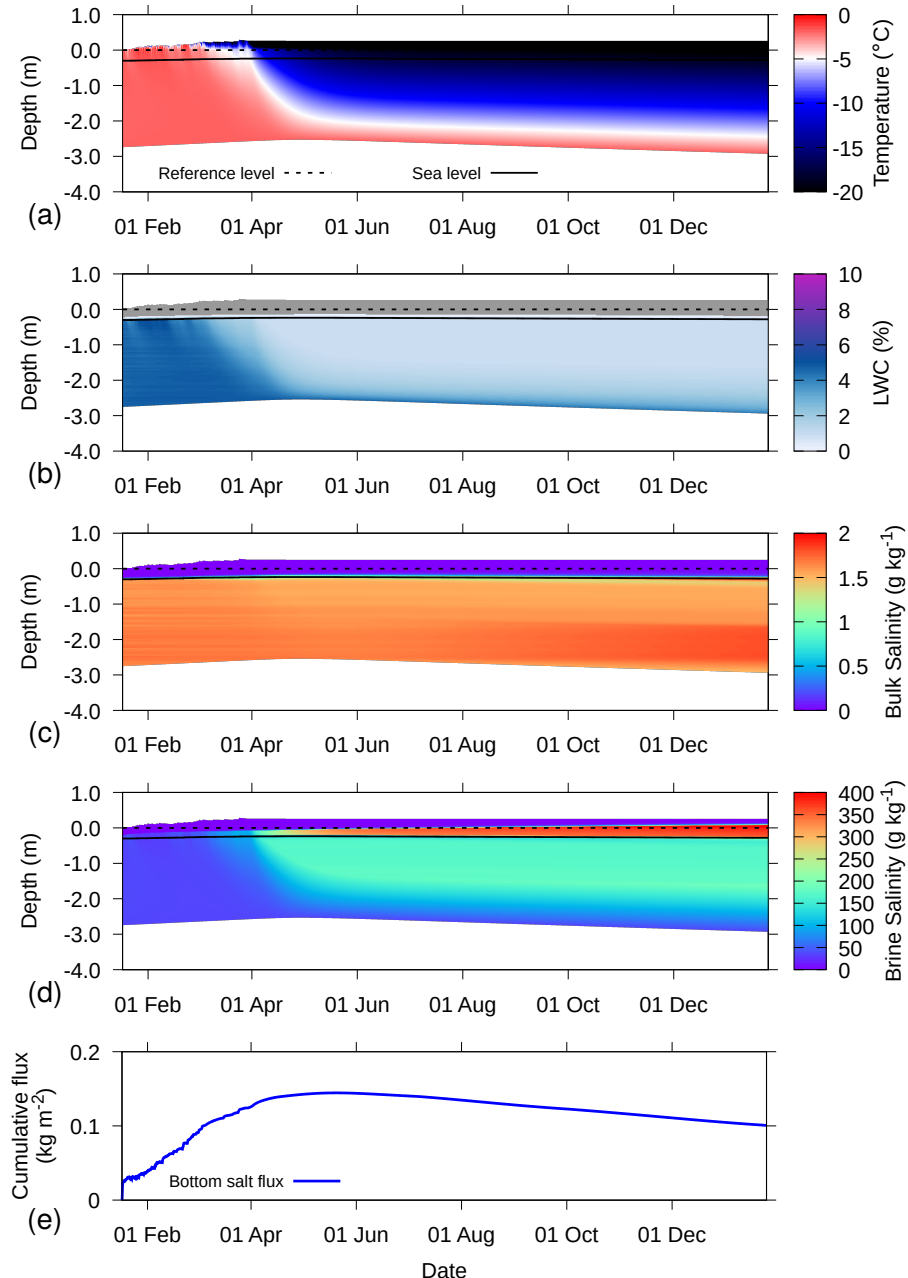


Figure 12. Simulation for 2016S31, where from April 1 onward, cooling conditions are enforced, for [temperature](#) (a) [temperature](#), [LWC](#) (b) [LWC](#), [bulk salinity](#) (c), [brine salinity](#) (d) [brine salinity](#) and (e) cumulative salt flux at the bottom of the sea ice (e). In (b), dry [parts of the snow](#) [is](#) [sea ice system](#) [are](#) colored grey. In (a), (b), (c), and (d), the depth on the y-axis is defined relative to the sea ice-snow interface, as determined upon installation (dashed line). The solid line denotes the sea level as determined by the simulations. An increasing cumulative flux denotes inflow and vice versa.

4.5 Thin Ice

A final test is run by starting with only 2 cm of ice, with constant atmospheric conditions to simulate thin ice evolution. The atmospheric conditions were set as -10°C air temperature, 100% relative humidity, no wind speed, no incoming solar radiation and a constant incoming longwave radiation of 230 W m^{-2} . The ocean heat flux was set to 0 W m^{-2} .

5 The simulations were run for 1 month, which resulted in approximately 50 cm ice growth (Fig. 13). The temperature distribution (Fig. 13a) shows a very strong gradient, as the bottom temperature is forced to the ocean water temperature, whereas the surface cools from radiation loss and sensible and latent heat exchange. The relatively warm sea ice compared to the air temperature results in a latent heat flux directed to the atmosphere, even though relative humidity is 100%. The evaporation at the top of the sea ice leads to an outflow of fresh water at the top of the snowpack, resulting in an accumulation of
10 salt near the surface (Kaleschke et al., 2004; Domine et al., 2005, e.g.).(e.g., Kaleschke et al., 2004; Domine et al., 2005). This is found in Fig. 13b and Fig. 13c in a salty slush layer at the surface with high LWC and high bulk salinity. The brine salinity (Fig. 13d) mimics the temperature distribution (Fig. 13a), because of the forced thermal equilibrium with the brine by the model. When the ice is very thin, the evaporation at the top of the ice causes an influx of salt at the bottom (Fig. 13e). The transport of salt from below decreases with increasing ice thickness, as capillary forces are not strong enough anymore to
15 bridge the freeboard.

5 Outlook

Here, we showed crucial modifications to the SNOWPACK model with the primary goal of simulating the snow covering sea ice. As we initially focus on the Southern Ocean, the modifications centered around liquid water percolation in the snow, and flooding with ocean water of the snow layer. These are crucial processes to simulate for interpreting snow height measurements.

20

Nevertheless, these first sets of simulations revealed several directions for future improvements. First of all, the used relationship between temperature and brine salinity (Eq. 2) is only valid for temperatures close to the melting temperature of water. Other relationships have been proposed (Vancoppenolle et al., 2019) and may be important to include for more accurate simulations.

25

Brine dynamics in sea ice is a very complex process. Particularly gravity drainage of brine is complex to simulate (Notz and Worster, 2009) and can have a profound influence on bulk salinity profiles. Typically, a decreasing bulk salinity is found with increasing floe thickness, due to gravity drainage (Kovacs, 1996). The current model framework is not able to reproduce this. Furthermore, cooling of thin ice during the freezing process increases the pressure in the brine pockets, which can cause upward brine migration and higher salinity near the sea ice surface. Our simulations show this as a result of an evaporative flux. However, 30 this effect may potentially be described by an additional term to the capillary pressure (Eq. 4).

The Crank-Nicolson scheme used for the transport equation causes some numerical instabilities, particularly when the volumetric ice content is at prescribed upper limit of 99%. This is a known problem with the Crank-Nicolson scheme (Østerby, 2003), and could be mitigated by using other numerical schemes.

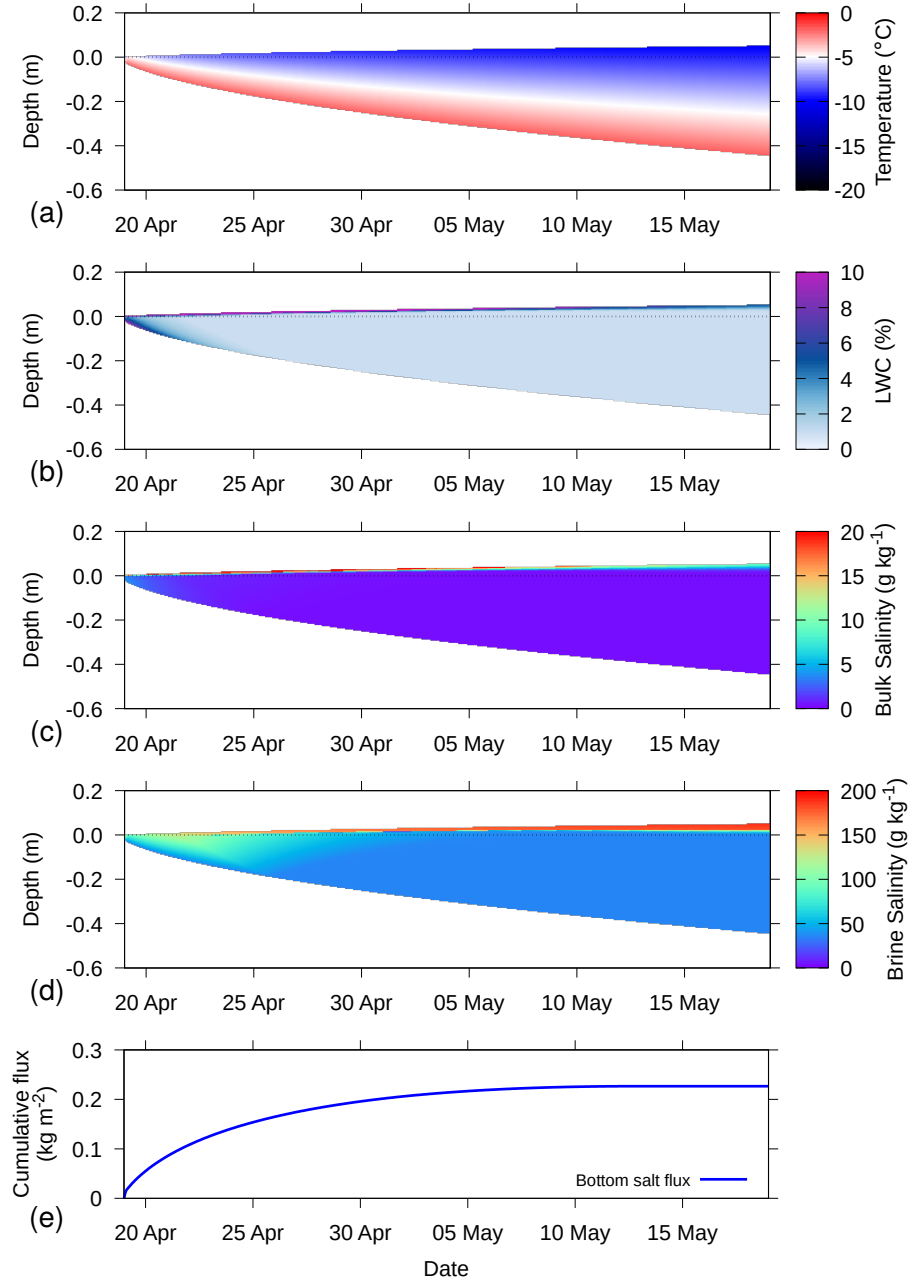


Figure 13. Simulation for 2016S31, where from April 1 onward, melting conditions are enforced, ice growth of thin ice, for temperature (a) temperature, LWC (b) LWC, bulk salinity (c), brine bulk salinity (d) brine salinity and (e) cumulative salt flux at the top and bottom of the sea ice (e). In (b), dry snow is colored grey. In (a), (b), (c), and (d), the depth on the y-axis is defined relative to sea level. An increasing cumulative flux denotes inflow and vice versa.

6 Conclusions

We introduced a series of modifications to the physics-based, multi-layer SNOWPACK model ~~to allow it to simulate sea ice. This involved modifying the model thermodynamics for simulations of the snow – sea ice system. The thermodynamic description in the model was modified~~ to account for the varying melting point of ice based on salinity and adding domain

5 restructuring to allow basal ice growth. Water transport through the snow – sea ice system can optionally be described by the Richards equation, which describes water flow in porous media for the full range from saturated conditions (Darcy law) to unsaturated conditions. This equation is coupled to a concentration equation for salinity. With the adapted model, we explicitly describe several aspects of brine dynamics, such as flooding, superimposed ice formation and the percolation of fresh water from snow melt, flushing the sea ice. The model formulations allow for a certain amount of drainage of dense brine, but the
10 process is largely underestimated compared to what is known from literature, as convective brine transport is, thus far, not described by the model.

The ~~modifications allow the~~ snow microstructure descriptions ~~previously~~ developed in the SNOWPACK model ~~to can now~~ be applied for sea ice conditions as well. The model is able to simulate the temporal evolution of snow density, grain size and shape and snow wetness over the life span of an ice floe. We find abundant depth hoar layers and melt layers, as well as
15 superimposed ice formation due to flooding and percolation. ~~The detailed snow microstructure evolution has the potential to be used to improve remote sensing retrieval algorithms to assess snow depth and ice thickness from space and driving radiative transfer models such as the Snow Microwave Radiative Transfer model SMRT (Picard et al., 2018).~~

Driving the simulations ~~, particularly using reanalysis model output seems to work well, apart from uncertainties in~~ estimating the ocean heat flux from below ~~, is difficult~~ and estimating precipitation amounts. The ability of SNOWPACK to use
20 ~~the in-situ snow depth to determine snow fall amounts was found to be useful for assessing the mass balance, but is difficult to upscale~~ due to limited ~~foreing measurement~~ data from polar regions. ~~Simulations~~ The simulations based on Snow and IMB Buoy data demonstrate ~~however~~ the importance of such remote data collection systems for modelling. ~~The detailed snow microstructure evolution can be used for remote sensing retrieval algorithms to assess snow depth and ice thickness from space. For this, a coupling to the Snow Microwave Radiative Transfer model SMRT (Picard et al., 2018) is foreseen.~~

25 *Code and data availability.* The SNOWPACK model and the MeteoIO meteorological preprocessing library (Bavay and Egger, 2014) needed to run SNOWPACK are available under a LGPLv3 license under <https://models.slf.ch>. The source code of the version used for the simulations presented in this study is available in the Online Supplement, and corresponds to revision 2508 of MeteoIO (<https://models.slf.ch/svn/meteoio/trunk>) and revision 1799 of SNOWPACK (<https://models.slf.ch/svn/snowpack/branches/dev>). The source code, input and configuration files, as well as run, postprocessing and plotting scripts for the example simulations in this study are also available in the Online Supplement. The website
30 <https://niviz.org/> can be used to visualize the SNOWPACK output files.

The data for Snow Buoys 2014S12 and 2016S31 can be acquired via doi: 10.1594/PANGAEA.875272 (Nicolaus and Schwegmann, 2017) and doi: 10.1594/PANGAEA.875287 (Arndt et al., 2017), respectively. IMB data from Buoy 2016T41 are available at <http://www.meereisportal>.

de, direct link: http://data.meereisportal.de/gallery/index_new.php?active-tab1=method&buoytype=TB®ion=s&buoystate=inactive&submit3=display&lang=en_US&active-tab2=buoy. ERA5 data can be accessed via doi: 10.5065/D6X34W69 (ERA, 2017).

Author contributions. NW developed the model code and performed the simulations, LR performed code testing, LR, NM, KL, LK, MN and ML contributed to model conceptualization and design. NW prepared the manuscript with contributions from all co-authors.

5 Acknowledgements

We thank the captain, officers and crew of R/V Polarstern for their support during the campaigns to deploy the Snow Bouys and IMBs. Louisa von Hülsen from the Alfred Wegener Institute is acknowledged for providing preliminary IMB analysis data. N.W. was supported by the Swiss National Science Foundation (SNSF), grant no. P2ELP2_172299. This work was additionally supported by the US National Science Foundation (NSF) grant no. OPP-1142075 and Swiss National Science Foundation grant no. PZ00P2_142684. We also thank the German Research Council (DFG) for funding the Snow cover impacts on Antarctic Sea Ice (SCASI) project within the framework of the priority program "Antarctic Research with comparative investigations in Arctic ice areas" (grant no: NI 1096/5-1 and KA 2694/7-1). The Helmholtz infrastructure programs FRAM and ACROSS is acknowledged for funding the Snow and Ice Mass-balance Buoys. ERA5 data constitute modified Copernicus Climate Change Service Information [2018].

References

ERA5 Reanalysis, <https://doi.org/10.5065/D6X34W69>, 2017.

Ackley, S. F., Xie, H., and Tichenor, E. A.: Ocean heat flux under Antarctic sea ice in the Bellingshausen and Amundsen Seas: two case studies, *Ann. Glaciol.*, 56, 200–210, <https://doi.org/10.3189/2015AoG69A890>, 2015.

5 Allison, I., Brandt, R. E., and Warren, S. G.: East Antarctic sea ice: Albedo, thickness distribution, and snow cover, *J. Geophys. Res.*, 98, 12 417–12 429, <https://doi.org/10.1029/93JC00648>, <http://dx.doi.org/10.1029/93JC00648>, 1993.

Anderson, E., Bai, Z., Bischof, C., Blackford, S., Demmel, J., Dongarra, J., Du Croz, J., Greenbaum, A., Hammarling, S., McKenney, A., and Sorensen, D.: LAPACK Users' Guide, Society for Industrial and Applied Mathematics, Philadelphia, PA, third edn., 1999.

Andreas, E. L.: Parameterizing Scalar Transfer over Snow and Ice: A Review, *J. Hydrometeor.*, 3, 417–432, [https://doi.org/10.1175/1525-7541\(2002\)003<0417:PSTOSA>2.0.CO;2](https://doi.org/10.1175/1525-7541(2002)003<0417:PSTOSA>2.0.CO;2), 2002.

10 Arndt, S. and Paul, S.: Variability of Winter Snow Properties on Different Spatial Scales in the Weddell Sea, *J. Geophys. Res.*, 123, 8862–8876, <https://doi.org/10.1029/2018JC014447>, <https://agupubs.onlinelibrary.wiley.com/doi/abs/10.1029/2018JC014447>, 2018.

15 Arndt, S., Rossmann, L., and Nicolaus, M.: Snow height on sea ice and sea ice drift from autonomous measurements from buoy 2016S31, deployed during POLARSTERN cruise PS96 (ANT-XXXI/2), PANGAEA, <https://doi.org/10.1594/PANGAEA.875287>, <https://doi.org/10.1594/PANGAEA.875287>, in: Nicolaus, Marcel; Hoppmann, Mario; Arndt, Stefanie; Hendricks, Stefan; Katlein, Christian; König-Langlo, Gert; Nicolaus, Anja; Rossmann, Leonard; Schiller, Martin; Schwegmann, Sandra; Langevin, Danielle; Bartsch, Annekathrin (2017): Snow height and air temperature on sea ice from Snow Buoy measurements. Alfred Wegener Institute, Helmholtz Centre for Polar and Marine Research, Bremerhaven, PANGAEA, <https://doi.org/10.1594/PANGAEA.875638>, 2017.

Assur, A.: Composition of sea ice and its tensile strength, Research report 44, U.S. Army Snow, Ice and Permafrost Research Establishment, 20 Corps of Engineers, Wilmette, Ill., 1960.

20 Bartelt, P. and Lehning, M.: A physical SNOWPACK model for the Swiss avalanche warning Part I: Numerical model, *Cold Reg. Sci. Technol.*, 35, 123–145, [https://doi.org/10.1016/S0165-232X\(02\)00074-5](https://doi.org/10.1016/S0165-232X(02)00074-5), 2002.

Baunach, T., Fierz, C., Satyawali, P. K., and Schneebeli, M.: A model for kinetic grain growth, *Ann. Glaciol.*, 32, 1–6, <https://doi.org/10.3189/172756401781819427>, 2001.

25 Bavay, M. and Egger, T.: MeteoIO 2.4.2: a preprocessing library for meteorological data, *Geosci. Model Dev.*, 7, 3135–3151, <https://doi.org/10.5194/gmd-7-3135-2014>, <http://www.geosci-model-dev.net/7/3135/2014/>, 2014.

Bitz, C. M. and Lipscomb, W. H.: An energy-conserving thermodynamic model of sea ice, *J. Geophys. Res.*, 104, 15 669–15 677, <https://doi.org/10.1029/1999JC900100>, <http://dx.doi.org/10.1029/1999JC900100>, 1999.

Brandt, R. E., Warren, S. G., Worby, A. P., and Grenfell, T. C.: Surface Albedo of the Antarctic Sea Ice Zone, *J. Climate*, 18, 3606–3622, 30 <https://doi.org/10.1175/JCLI3489.1>, <https://doi.org/10.1175/JCLI3489.1>, 2005.

Brun, E., David, P., Sudul, M., and Brunot, G.: A numerical model to simulate snow-cover stratigraphy for operational avalanche forecasting, *J. Glaciol.*, 38, 13–22, 1992.

Buckingham, E.: Studies on the movement of soil moisture, Bureau of Soils, Bulletin 38, United States Department of Agriculture, Washington, DC, 1907.

35 Calonne, N., Flin, F., Morin, S., Lesaffre, B., du Roscoat, S. R., and Geindreau, C.: Numerical and experimental investigations of the effective thermal conductivity of snow, *Geophys. Res. Lett.*, 38, L23 501, <https://doi.org/10.1029/2011GL049234>, 2011.

Calonne, N., Geindreau, C., Flin, F., Morin, S., Lesaffre, B., Rolland du Roscoat, S., and Charrier, P.: 3-D image-based numerical computations of snow permeability: links to specific surface area, density, and microstructural anisotropy, *Cryosphere*, 6, 939–951, <https://doi.org/10.5194/tc-6-939-2012>, 2012.

Celia, M. A., Bouloutas, E. T., and Zarba, R. L.: A general mass-conservative numerical solution for the unsaturated flow equation, *Water Resour. Res.*, 26, 1483–1496, <https://doi.org/10.1029/WR026i007p01483>, 1990.

5 Chung, Y.-C., Bélair, S., and Mailhot, J.: Simulation of Snow on Arctic Sea Ice Using a Coupled Snow–Ice Model, *J. Hydrometeor.*, 11, 199–210, <https://doi.org/10.1175/2009JHM1112.1>, <https://doi.org/10.1175/2009JHM1112.1>, 2010.

Courant, R., Friedrichs, K., and Lewy, H.: Über die partiellen Differenzengleichungen der mathematischen Physik, *Math. Ann.*, 100, 32–74, <https://doi.org/10.1007/BF01448839>, in German., 1928.

10 Cox, G. F. N. and Weeks, W. F.: Salinity Variations in Sea Ice, *J. Glaciol.*, 13, 109–120, <https://doi.org/10.3189/S0022143000023418>, 1974.

Crank, J. and Nicolson, P.: A practical method for numerical evaluation of solutions of partial differential equations of the heat-conduction type, *Advances in Computational Mathematics*, 6, 207–226, <https://doi.org/10.1007/BF02127704>, <https://doi.org/10.1007/BF02127704>, 1996.

Curry, J. A., Schramm, J. L., and Ebert, E. E.: Sea Ice-Albedo Climate Feedback Mechanism, *J. Climate*, 8, 240–247, [https://doi.org/10.1175/1520-0442\(1995\)008<0240:SIACFM>2.0.CO;2](https://doi.org/10.1175/1520-0442(1995)008<0240:SIACFM>2.0.CO;2), 1995.

15 Déry, S. J. and Tremblay, L.-B.: Modeling the Effects of Wind Redistribution on the Snow Mass Budget of Polar Sea Ice, *J. Phys. Oceanogr.*, 34, 258–271, [https://doi.org/10.1175/1520-0485\(2004\)034<0258:MTEOWR>2.0.CO;2](https://doi.org/10.1175/1520-0485(2004)034<0258:MTEOWR>2.0.CO;2), 2004.

Domine, F., Sparapani, R., Ianniello, A., and Beine, H. J.: The origin of sea salt in snow on Arctic sea ice and in coastal regions, *Atmos. Chem. Phys.*, 4, 2259–2271, <https://doi.org/10.5194/acp-4-2259-2004>, 2004.

20 Domine, F., Taillandier, A. S., Simpson, W. R., and Severin, K.: Specific surface area, density and microstructure of frost flowers, *Geophys. Rese. Lett.*, 32, L13 502, <https://doi.org/10.1029/2005GL023245>, <https://agupubs.onlinelibrary.wiley.com/doi/abs/10.1029/2005GL023245>, 2005.

Domine, F., Picard, G., Morin, S., Barrere, M., Madore, J.-B., and Langlois, A.: Major Issues in Simulating Some Arctic Snowpack Properties Using Current Detailed Snow Physics Models: Consequences for the Thermal Regime and Water Budget of Permafrost, *J. Adv. Model. Earth Sy.*, 11, 34–44, <https://doi.org/10.1029/2018MS001445>, <https://agupubs.onlinelibrary.wiley.com/doi/abs/10.1029/2018MS001445>, 2019.

25 Drinkwater, M. R. and Crocker, G.: Modelling Changes in Scattering Properties of the Dielectric and Young Snow-Covered Sea Ice at GHz frequencies, *J. Glaciol.*, 34, 274–282, <https://doi.org/10.3189/S0022143000007012>, 1988.

Eicken, H., Lange, M. A., and Wadhams, P.: Characteristics and distribution patterns of snow and meteoric ice in the Weddell Sea and their 30 contribution to the mass balance of sea ice, *Ann. Geophys.*, 12, 80–93, <https://doi.org/10.1007/s00585-994-0080-x>, <http://dx.doi.org/10.1007/s00585-994-0080-x>, 1994.

Eicken, H., Fischer, H., and Lemke, P.: Effects of the snow cover on Antarctic sea ice and potential modulation of its response to climate change, *Ann. Glaciol.*, 21, 369–376, <https://doi.org/10.3189/S0260305500016086>, 1995.

35 Ferrari, R., Jansen, M. F., Adkins, J. F., Burke, A., Stewart, A. L., and Thompson, A. F.: Antarctic sea ice control on ocean circulation in present and glacial climates, *PNAS*, <https://doi.org/10.1073/pnas.1323922111>, <http://www.pnas.org/content/early/2014/05/29/1323922111>, 2014.

Fuller, M. C., Geldsetzer, T., Yackel, J., and Gill, J. P. S.: Comparison of a coupled snow thermodynamic and radiative transfer model with in situ active microwave signatures of snow-covered smooth first-year sea ice, *Cryosphere*, 9, 2149–2161, <https://doi.org/10.5194/tc-9-2149-2015>, <https://www.the-cryosphere.net/9/2149/2015/>, 2015.

Gallet, J.-C., Merkouriadi, I., Liston, G. E., Polashenski, C., Hudson, S., R"osel, A., and Gerland, S.: Spring snow conditions on Arctic sea ice north of Svalbard, during the Norwegian Young Sea ICE (N-ICE2015) expedition, *J. Geophys. Res.*, 122, 10,820–10,836, <https://doi.org/10.1002/2016JD026035>, <https://agupubs.onlinelibrary.wiley.com/doi/abs/10.1002/2016JD026035>, 2017.

Golden, K. M., Eicken, H., Heaton, A. L., Miner, J., Pringle, D. J., and Zhu, J.: Thermal evolution of permeability and microstructure in sea ice, *Geophys. Res. Lett.*, 34, <https://doi.org/10.1029/2007GL030447>, <https://agupubs.onlinelibrary.wiley.com/doi/abs/10.1029/2007GL030447>, 2007.

10 Goosse, H. and Fichefet, T.: Importance of ice-ocean interactions for the global ocean circulation: A model study, *J. Geophys. Res.*, 104, 23 337–23 355, <https://doi.org/10.1029/1999JC900215>, <https://agupubs.onlinelibrary.wiley.com/doi/abs/10.1029/1999JC900215>, 1999.

Gordon, A. L.: The Southern-Ocean and Global Climate, *Oceanus*, 31, 39–46, 1988.

Grenfell, T. C. and Perovich, D. K.: Spectral albedos of sea ice and incident solar irradiance in the southern Beaufort Sea, *J. Geophys. Res.*, 89, 3573–3580, <https://doi.org/10.1029/JC089iC03p03573>, <https://agupubs.onlinelibrary.wiley.com/doi/abs/10.1029/JC089iC03p03573>, 1984.

15 Griewank, P. J. and Notz, D.: Insights into brine dynamics and sea ice desalination from a 1-D model study of gravity drainage, *J. Geophys. Res.*, 118, 3370–3386, <https://doi.org/10.1002/jgrc.20247>, 2013.

Groot Zwaftink, C. D., Cagnati, A., Crepaz, A., Fierz, C., Macelloni, G., Valt, M., and Lehning, M.: Event-driven deposition of snow on the Antarctic Plateau: analyzing field measurements with SNOWPACK, *Cryosphere*, 7, 333–347, <https://doi.org/10.5194/tc-7-333-2013>, 2013.

20 Grosfeld, K., Treffeisen, R., Asseng, J., Bartsch, A., Bräuer, B., Fritzsch, B., Gerdts, R., Hendricks, S., Hiller, W., Heygster, G., Krumpen, T., Lemke, P., Melsheimer, C., Nicolaus, M., Ricker, R., and Weigelt, M.: Online sea-ice knowledge and data platform <www.meereisportal.de>, *Polarforschung*, 85, 143–155, <https://doi.org/10.2312/polfor.2016.011>, 2015.

Haas, C., Thomas, D. N., and Bareiss, J.: Surface properties and processes of perennial Antarctic sea ice in summer, *J. Glaciol.*, 47, 613–625, <https://doi.org/10.3189/172756501781831864>, 2001.

25 Haas, C., Beckers, J., King, J., Silis, A., Stroeve, J., Wilkinson, J., Notenboom, B., Schweiger, A., and Hendricks, S.: Ice and Snow Thickness Variability and Change in the High Arctic Ocean Observed by In Situ Measurements, *Geophys. Res. Lett.*, 44, 10,462–10,469, <https://doi.org/10.1002/2017GL075434>, <https://agupubs.onlinelibrary.wiley.com/doi/abs/10.1002/2017GL075434>, 2017.

Haverkamp, R. and Vauclin, M.: A note on estimating finite difference interblock hydraulic conductivity values for transient unsaturated flow problems, *Water Resour. Res.*, 15, 181–187, <https://doi.org/10.1029/WR015i001p00181>, 1979.

30 Hunke, E. C., Notz, D., Turner, A. K., and Vancoppenolle, M.: The multiphase physics of sea ice: a review for model developers, *Cryosphere*, 5, 989–1009, <https://doi.org/10.5194/tc-5-989-2011>, <https://www.the-cryosphere.net/5/989/2011/>, 2011.

Huwald, H., Tremblay, L.-B., and Blatter, H.: A multilayer sigma-coordinate thermodynamic sea ice model: Validation against Surface Heat Budget of the Arctic Ocean (SHEBA)/Sea Ice Model Intercomparison Project Part 2 (SIMIP2) data, *J. Geophys. Res.*, 110, C05 010, <https://doi.org/10.1029/2004JC002328>, <https://agupubs.onlinelibrary.wiley.com/doi/abs/10.1029/2004JC002328>, 2005.

35 Jackson, K., Wilkinson, J., Maksym, T., Meldrum, D., Beckers, J., Haas, C., and Mackenzie, D.: A Novel and Low-Cost Sea Ice Mass Balance Buoy, *J. Atmos. Ocean Technol.*, 30, 2676–2688, <https://doi.org/10.1175/JTECH-D-13-00058.1>, <https://doi.org/10.1175/JTECH-D-13-00058.1>, 2013.

Jeffries, M. O., Morris, K., Weeks, W., and Worby, A. P.: Seasonal variations in the properties and structural composition of sea ice and snow cover in the Bellingshausen and Amundsen Seas, Antarctica, *J. Glaciol.*, 43, 138–151, <https://doi.org/10.3198/1997JoG43-143-138-151>, 1997.

Jordan, R. E., Andreas, E. L., and Makshtas, A. P.: Heat budget of snow-covered sea ice at North Pole 4, *J. Geophys. Res.*, 104, 7785–7806, 5 <https://doi.org/10.1029/1999JC900011>, <https://agupubs.onlinelibrary.wiley.com/doi/abs/10.1029/1999JC900011>, 1999.

Kaleschke, L., Richter, A., Burrows, J., Afe, O., Heygster, G., Notholt, J., Rankin, A. M., Roscoe, H. K., Hollwedel, J., Wagner, T., and Jacobi, H.-W.: Frost flowers on sea ice as a source of sea salt and their influence on tropospheric halogen chemistry, *Geophysical Research Letters*, 31, L16 114, <https://doi.org/10.1029/2004GL020655>, <https://agupubs.onlinelibrary.wiley.com/doi/abs/10.1029/2004GL020655>, 2004.

Kovacs, A.: Sea Ice. Part I. Bulk Salinity Versus Floe Thickness, CRREL report, U.S. Army Cold Regions Research and Engineering 10 Laboratory, 1996.

Lecomte, O., Fichefet, T., Vancoppenolle, M., and Nicolaus, M.: A new snow thermodynamic scheme for large-scale sea-ice models, *Ann. Glaciol.*, 52, 337–346, 2011.

Ledley, T. S.: Snow on sea ice: Competing effects in shaping climate, *J. Geophys. Res.*, 96, 17 195–17 208, 15 <https://doi.org/10.1029/91JD01439>, <https://agupubs.onlinelibrary.wiley.com/doi/abs/10.1029/91JD01439>, 1991.

Lehning, M., Bartelt, P., Brown, B., Russi, T., Stöckli, U., and Zimmerli, M.: SNOWPACK calculations for avalanche warning based upon a new network of weather and snow stations, *Cold Reg. Sci. Technol.*, 30, 145–157, [https://doi.org/10.1016/S0165-232X\(99\)00022-1](https://doi.org/10.1016/S0165-232X(99)00022-1), 1999.

Lehning, M., Bartelt, P., Brown, B., Fierz, C., and Satyawali, P.: A physical SNOWPACK model for the Swiss avalanche warning Part II: Snow microstructure, *Cold Reg. Sci. Technol.*, 35, 147–167, [https://doi.org/10.1016/S0165-232X\(02\)00073-3](https://doi.org/10.1016/S0165-232X(02)00073-3), 2002a.

Lehning, M., Bartelt, P., Brown, B., and Fierz, C.: A physical SNOWPACK model for the Swiss avalanche warning Part III: Meteorological 20 forcing, thin layer formation and evaluation, *Cold Reg. Sci. Technol.*, 35, 169–184, [https://doi.org/10.1016/S0165-232X\(02\)00072-1](https://doi.org/10.1016/S0165-232X(02)00072-1), 2002b.

Leonard, K. C. and Maksym, T.: The importance of wind-blown snow redistribution to snow accumulation on Bellingshausen Sea ice, *Ann. Glaciol.*, 52, 271–278, <https://doi.org/10.3189/172756411795931651>, 2011.

Lewis, M., Tison, J., Weissling, B., Delille, B., Ackley, S., Brabant, F., and Xie, H.: Sea ice and snow cover characteristics during 25 the winter-spring transition in the Bellingshausen Sea: An overview of SIMBA 2007, *Deep-Sea Res. Pt. II*, 58, 1019–1038, <https://doi.org/10.1016/j.dsr2.2010.10.027>, 2011.

Liston, G. E., Polashenski, C., Rösel, A., Itkin, P., King, J., Merkouriadi, I., and Haapala, J.: A Distributed Snow-Evolution Model for Sea-Ice Applications (SnowModel), *J. Geophys. Res.*, 123, 3786–3810, <https://doi.org/10.1002/2017JC013706>, <https://agupubs.onlinelibrary.wiley.com/doi/abs/10.1002/2017JC013706>, 2018.

Maksym, T. and Jeffries, M. O.: A one-dimensional percolation model of flooding and snow ice formation on Antarctic sea ice, *J. Geophys. Res.*, 105, 26 313–26 331, <https://doi.org/10.1029/2000JC900130>, 2000.

Markus, T. and Cavalieri, D. J.: Snow Depth Distribution Over Sea Ice in the Southern Ocean from Satellite Passive Microwave Data, pp. 19–39, American Geophysical Union (AGU), <https://doi.org/10.1029/AR074p0019>, <https://agupubs.onlinelibrary.wiley.com/doi/abs/10.1029/AR074p0019>, 1998.

Massel, S. R.: Internal Gravity Waves in the Shallow Seas, Springer International Publishing, Switzerland, <https://doi.org/10.1007/978-3-319-18908-6>, 2015.

Massom, R. A., Drinkwater, M. R., and Haas, C.: Winter snow cover on sea ice in the Weddell Sea, *J. Geophys. Res.*, 102, 1101–1117, 35 <https://doi.org/10.1029/96JC02992>, 1997.

Massom, R. A., Drinkwater, M. R., and Haas, C.: Winter snow cover on sea ice in the Weddell Sea, *J. Geophys. Res.*, 102, 1101–1117, <https://doi.org/10.1029/96JC02992>, <https://agupubs.onlinelibrary.wiley.com/doi/abs/10.1029/96JC02992>, 1998.

Massom, R. A., Eicken, H., Hass, C., Jeffries, M. O., Drinkwater, M. R., Sturm, M., Worby, A. P., Wu, X., Lytle, V. I., Ushio, S., Morris, K., Reid, P. A., Warren, S. G., and Allison, I.: Snow on Antarctic sea ice, *Rev. Geophys.*, 39, 413–445, <https://doi.org/10.1029/2000RG000085>, 5 2001.

Maykut, G. A. and Untersteiner, N.: Some results from a time-dependent thermodynamic model of sea ice, *J. Geophys. Res.*, 76, 1550–1575, <https://doi.org/10.1029/JC076i006p01550>, <https://agupubs.onlinelibrary.wiley.com/doi/abs/10.1029/JC076i006p01550>, 1971.

Merkouriadi, I., Gallet, J.-C., Graham, R. M., Liston, G. E., Polashenski, C., Rösel, A., and Gerland, S.: Winter snow conditions on Arctic sea ice north of Svalbard during the Norwegian young sea ICE (N-ICE2015) expedition, *J. Geophys. Res.*, 122, 10,837–10,854, 10 <https://doi.org/10.1002/2017JD026753>, <https://agupubs.onlinelibrary.wiley.com/doi/abs/10.1002/2017JD026753>, 2017.

Mualem, Y.: A new model for predicting the hydraulic conductivity of unsaturated porous media, *Water Resour. Res.*, 12, 513–522, <https://doi.org/10.1029/WR012i003p00513>, 1976.

Nicolaus, M. and Schwegmann, S.: Snow height on sea ice and sea ice drift from autonomous measurements from buoy 2014S12, deployed during POLARSTERN cruise PS82 (ANT-XXIX/9), PANGAEA, <https://doi.org/10.1594/PANGAEA.875272>, <https://doi.org/10.1594/PANGAEA.875272>, in: Nicolaus, Marcel; Hoppmann, Mario; Arndt, Stefanie; Hendricks, Stefan; Katlein, Christian; König-Langlo, Gert; Nicolaus, Anja; Rossmann, Leonard; Schiller, Martin; Schwegmann, Sandra; Langevin, Danielle; Bartsch, Annekathrin (2017): Snow height and air temperature on sea ice from Snow Buoy measurements. Alfred Wegener Institute, Helmholtz Centre for Polar and Marine Research, Bremerhaven, PANGAEA, <https://doi.org/10.1594/PANGAEA.875638>, 2017.

Nicolaus, M., Haas, C., and Bareiss, J.: Observations of superimposed ice formation at melt-onset on fast ice on Kongsfjorden, Svalbard, 20 *Phys. Chem. Earth*, 28, 1241–1248, <https://doi.org/10.1016/j.pce.2003.08.048>, 2003.

Nicolaus, M., Haas, C., Bareiss, J., and Willmes, S.: A model study of differences of snow thinning on Arctic and Antarctic first-year sea ice during spring and summer, *Ann. Glaciol.*, 44, 147–153, <https://doi.org/10.3189/172756406781811312>, 2006.

Nicolaus, M., Haas, C., and Willmes, S.: Evolution of first-year and second-year snow properties on sea ice in the Weddell Sea during spring-summer transition, *J. Geophys. Res.*, 114, <https://doi.org/10.1029/2008JD011227>, <https://agupubs.onlinelibrary.wiley.com/doi/abs/10.1029/2008JD011227>, 2009.

Nicolaus, M., Hoppmann, M., Arndt, S., Hendricks, S., Katlein, C., König-Langlo, G., Nicolaus, A., Rossmann, L., Schiller, M., Schwegmann, S., Langevin, D., and Bartsch, A.: Snow height and air temperature on sea ice from Snow Buoy measurements, <https://doi.org/10.1594/PANGAEA.875638>, <https://doi.org/10.1594/PANGAEA.875638>, 2017.

Notz, D.: Challenges in simulating sea ice in Earth System Models, *WIREs Clim. Change*, 3, 509–526, <https://doi.org/10.1002/wcc.189>, 30 <https://onlinelibrary.wiley.com/doi/abs/10.1002/wcc.189>, 2012.

Notz, D. and Worster, M. G.: Desalination processes of sea ice revisited, *J. Geophys. Res.*, 114, <https://doi.org/10.1029/2008JC004885>, <https://agupubs.onlinelibrary.wiley.com/doi/abs/10.1029/2008JC004885>, 2009.

Obleitner, F. and Lehning, M.: Measurement and simulation of snow and superimposed ice at the Kongsvegen glacier, Svalbard (Spitzbergen), *J. Geophys. Res.*, 109, <https://doi.org/10.1029/2003JD003945>, <https://agupubs.onlinelibrary.wiley.com/doi/abs/10.1029/2003JD003945>, 35 2004.

Østerby, O.: Five Ways of Reducing the Crank–Nicolson Oscillations, *BIT Numerical Mathematics*, 43, 811–822, <https://doi.org/10.1023/B:BITN.0000009942.00540.94>, <https://doi.org/10.1023/B:BITN.0000009942.00540.94>, 2003.

Perovich, D., Jones, K., Light, B., Eicken, H., Markus, T., Stroeve, J., and Lindsay, R.: Solar partitioning in a changing Arctic sea-ice cover, *Ann. Glaciol.*, 52, 192–196, <https://doi.org/10.3189/172756411795931543>, 2011.

Petty, A. A., Webster, M., Boisvert, L., and Markus, T.: The NASA Eulerian Snow on Sea Ice Model (NESOSIM) v1.0: initial model development and analysis, *Geosci. Model Dev.*, 11, 4577–4602, <https://doi.org/10.5194/gmd-11-4577-2018>, <https://www.geosci-model-dev.net/11/4577/2018/>, 2018.

Picard, G., Sandells, M., and Löwe, H.: SMRT: an active–passive microwave radiative transfer model for snow with multiple microstructure and scattering formulations (v1.0), *Geosci. Model Dev.*, 11, 2763–2788, <https://doi.org/10.5194/gmd-11-2763-2018>, <https://www.geosci-model-dev.net/11/2763/2018/>, 2018.

Poisson, A. and Papa, A.: Diffusion coefficients of major ions in seawater, *Mar. Chem.*, 13, 265–280, [https://doi.org/10.1016/0304-4203\(83\)90002-6](https://doi.org/10.1016/0304-4203(83)90002-6), 1983.

Powell, D. C., Markus, T., Cavalieri, D. J., Gasiewski, A. J., Klein, M., Maslanik, J. A., Stroeve, J. C., and Sturm, M.: Microwave Signatures of Snow on Sea Ice: Modeling, *IEEE T. Geosci. Remote*, 44, 3091–3102, <https://doi.org/10.1109/TGRS.2006.882139>, 2006.

Rankin, A. M., Wolff, E. W., and Martin, S.: Frost flowers: Implications for tropospheric chemistry and ice core interpretation, *J. Geophys. Res.*, 107, <https://doi.org/10.1029/2002JD002492>, <https://agupubs.onlinelibrary.wiley.com/doi/abs/10.1029/2002JD002492>, 2002.

Ricker, R., Hendricks, S., Helm, V., Skourup, H., and Davidson, M.: Sensitivity of CryoSat-2 Arctic sea-ice freeboard and thickness on radar-waveform interpretation, *Cryosphere*, 8, 1607–1622, <https://doi.org/10.5194/tc-8-1607-2014>, <https://www.the-cryosphere.net/8/1607/2014/>, 2014.

Steger, C. R., Reijmer, C. H., van den Broeke, M. R., Wever, N., Forster, R. R., Koenig, L. S., Kuipers Munneke, P., Lehning, M., Lhermitte, S., Ligtenberg, S. R. M., Miège, C., and Noël, B. P. Y.: Firn Meltwater Retention on the Greenland Ice Sheet: A Model Comparison, *Front. Earth Sci.*, 5, 3, <https://doi.org/10.3389/feart.2017.00003>, <https://www.frontiersin.org/article/10.3389/feart.2017.00003>, 2017.

Sturm, M., Holmgren, J., and Perovich, D. K.: Winter snow cover on the sea ice of the Arctic Ocean at the Surface Heat Budget of the Arctic Ocean (SHEBA): Temporal evolution and spatial variability, *J. Geophys. Res.*, 107, SHE 23–1–SHE 23–17, <https://doi.org/10.1029/2000JC000400>, 8047, 2002a.

Sturm, M., Perovich, D. K., and Holmgren, J.: Thermal conductivity and heat transfer through the snow on the ice of the Beaufort Sea, *J. Geophys. Res.*, 107, SHE 19–1–SHE 19–17, <https://doi.org/10.1029/2000JC000409>, <https://agupubs.onlinelibrary.wiley.com/doi/abs/10.1029/2000JC000409>, 2002b.

Toyota, T., Takatsuji, S., Tateyama, K., Naoki, K., and Ohshima, K. I.: Properties of sea ice and overlying snow in the Southern Sea of Okhotsk, *J. Oceanogr.*, 63, 393–411, <https://doi.org/10.1007/s10872-007-0037-2>, <https://doi.org/10.1007/s10872-007-0037-2>, 2007.

Tremblay, L.-B. and Mysak, L. A.: Modeling Sea Ice as a Granular Material, Including the Dilatancy Effect, *J. Phys. Oceanogr.*, 27, 2342–2360, [https://doi.org/10.1175/1520-0485\(1997\)027<2342:MSIAAG>2.0.CO;2](https://doi.org/10.1175/1520-0485(1997)027<2342:MSIAAG>2.0.CO;2), 1997.

Trujillo, E., Leonard, K., Maksym, T., and Lehning, M.: Changes in snow distribution and surface topography following a snowstorm on Antarctic sea ice, *J. Geophys. Res.*, 121, 2172–2191, <https://doi.org/10.1002/2016JF003893>, <https://agupubs.onlinelibrary.wiley.com/doi/abs/10.1002/2016JF003893>, 2016.

Turner, A. K. and Hunke, E. C.: Impacts of a mushy-layer thermodynamic approach in global sea-ice simulations using the CICE sea-ice model, *J. Geophys. Res.*, 120, 1253–1275, <https://doi.org/10.1002/2014JC010358>, <https://agupubs.onlinelibrary.wiley.com/doi/abs/10.1002/2014JC010358>, 2014.

Ukita, J. and Martinson, D. G.: An efficient adjustable-layering thermodynamic sea-ice model formulation for high-frequency forcing, *Ann. Glaciol.*, 33, 253–260, <https://doi.org/10.3189/172756401781818194>, 2001.

van Genuchten, M. T.: A Closed-form Equation for Predicting the Hydraulic Conductivity of Unsaturated Soils, *Soil Sci. Soc. Am. J.*, 44, 892–898, <https://doi.org/10.2136/sssaj1980.03615995004400050002x>, 1980.

Vancoppenolle, M., Goosse, H., de Montety, A., Fichefet, T., Tremblay, B., and Tison, J.-L.: Modeling brine and nutrient dynamics in Antarctic sea ice: The case of dissolved silica, *J. Geophys. Res.*, 115, <https://doi.org/10.1029/2009JC005369>, <https://agupubs.onlinelibrary.wiley.com/doi/abs/10.1029/2009JC005369>, 2010.

Vancoppenolle, M., Madec, G., Thomas, M., and McDougall, T. J.: Thermodynamics of Sea Ice Phase Composition Revisited, *J. Geophys. Res.*, 124, 615–634, <https://doi.org/10.1029/2018JC014611>, <https://agupubs.onlinelibrary.wiley.com/doi/abs/10.1029/2018JC014611>, 2019.

Veldman, A. E. P. and Rinzema, K.: Playing with nonuniform grids, *Journal of Engineering Mathematics*, 26, 119–130, <https://doi.org/10.1007/BF00043231>, <https://doi.org/10.1007/BF00043231>, 1992.

Weiss, A. I., King, J., Lachlan-Cope, T., and Ladkin, R.: On the effective aerodynamic and scalar roughness length of Weddell Sea ice, *J. Geophys/ Res.*, 116, D19 119, <https://doi.org/10.1029/2011JD015949>, <https://agupubs.onlinelibrary.wiley.com/doi/abs/10.1029/2011JD015949>, 2011.

Wever, N., Lehning, M., Clifton, A., Rüedi, J.-D., Nishimura, K., Nemoto, M., Yamaguchi, S., and Sato, A.: Verification of moisture budgets during drifting snow conditions in a cold wind tunnel, *Water Resour. Res.*, 45, <https://doi.org/10.1029/2008WR007522>, <http://dx.doi.org/10.1029/2008WR007522>, w07423, 2009.

Wever, N., Fierz, C., Mitterer, C., Hirashima, H., and Lehning, M.: Solving Richards Equation for snow improves snowpack meltwater runoff estimations in detailed multi-layer snowpack model, *Cryosphere*, 8, 257–274, <https://doi.org/10.5194/tc-8-257-2014>, 2014.

Wever, N., Schmid, L., Heilig, A., Eisen, O., Fierz, C., and Lehning, M.: Verification of the multi-layer SNOWPACK model with different water transport schemes, *Cryosphere*, 9, 2271–2293, <https://doi.org/10.5194/tc-9-2271-2015>, <http://www.the-cryosphere.net/9/2271/2015/>, 2015.

Wever, N., Würzer, S., Fierz, C., and Lehning, M.: Simulating ice layer formation under the presence of preferential flow in layered snowpacks, *Cryosphere*, 10, 2731–2744, <https://doi.org/10.5194/tc-10-2731-2016>, <http://www.the-cryosphere.net/10/2731/2016/>, 2016.

Willatt, R. C., Giles, K. A., Laxon, S. W., Stone-Drake, L., and Worby, A. P.: Field Investigations of Ku-Band Radar Penetration Into Snow Cover on Antarctic Sea Ice, *IEEE T. Geosci. Remote*, 48, 365–372, <https://doi.org/10.1109/TGRS.2009.2028237>, 2010.

Yamaguchi, S., Watanabe, K., Katsushima, T., Sato, A., and Kumakura, T.: Dependence of the water retention curve of snow on snow characteristics, *Ann. Glaciol.*, 53, 6–12, <https://doi.org/10.3189/2012AoG61A001>, 2012.